eXPRESS Polymer Letters Vol.9, No.2 (2015) 84
Available online at www.expresspolymlett.com
DOI: 10.3144/expresspolymlett.2015.9

Editorial corner – a personal view
Polymer self-heals in seconds

M. Q. Zhang[*]

Materials Science Institute, Sun Yat-sen (Zhongshan) University, 510275 Guangzhou, P. R. China

Recently, self-healing polymers capable of autonomously restoring themselves have attracted more and more research interests. Many approaches that impart remendability to polymeric materials by either incorporation of healing agent into the matrices or making use of reversible inter/intra-macromolecular bonding have been proposed. Comparatively, however, most of the research concerns are focused on the extent of properties recovery rather than the speed.

In fact, rapid healing of cracks is highly desired for practical applications. On the one hand, crack propagates very fast; on the other hand, the damaged materials should be healed immediately to prevent occurrence of catastrophic failure.

By reviewing the available literature, we find that the reported time taken for reaching steady state or maximum healing used to be on the level of hour or dozens of minutes. Evidently, it needs to be greatly shortened.

To tackle the problem, SbF_5 (ACS Appl. Mater. Interfaces, DOI: 10.1021/am405989b), a strong Lewis acid, and trifluoromethanesulfonic acid (Compos Sci. Technol., DOI: 10.1016/j.compscitech.2014.08.028), a strong Bronsted acid, were employed for formulating fast healing systems, respectively. In actual operation, the acids were encapsulated by silica, and then embedded in epoxy matrix together with encapsulated epoxy monomer. Upon cracking of the composite, the fluidic chemicals released from the broken microcapsules flowed to the damage sites due to capillary effect and curing of the epoxy monomer occurred, re-connecting the cracked faces. Both impact and fatigue tests demonstrated that mechanical strength of the epoxy filled with the healing agent can be recovered within seconds at room temperature without manual intervention. Moreover, the healing system consisting of trifluoromethanesulfonic acid-epoxy pair turned out to possess significant thermal stability. It can survive the rigorous processing of high T_g epoxy (>240°C) during composite fabrication and provide the composite that was pre-treated at 180°C for 5 h with the same healing efficiency as the untreated one.

The above investigations also indicate that the healing speed of fast self-healing materials is difficult to be precisely evaluated by the existing destructive tests because of the time consuming recombination of the broken specimens. Fast in-situ measurement protocol like ultrasonic immersion technique that allows for determining elastic constants (Angew. Makromol. Chem., DOI: 10.1002/apmc.1992.051980104) within short time should be introduced.

Although the healing systems based on the encapsulated strong Lewis or Bronsted acids and epoxy monomer have shown their ultrafast healability, much milder substitute with comparable healing speed is still worth being developed in view of easy handling. Besides, the balance between the rate of curing and speed of healing agent delivery should be considered when large damage sites are dealt.

Prof. Dr. Ming Qiu Zhang
Member of International Advisory Board

[*]Corresponding author, e-mail: ceszmq@mail.sysu.edu.cn

eXPRESS Polymer Letters Vol.9, No.2 (2015) 85–94
Available online at www.expresspolymlett.com
DOI: 10.3144/expresspolymlett.2015.10

Novel high glass temperature sugar-based epoxy resins: Characterization and comparison to mineral oil-based aliphatic and aromatic resins

P. Niedermann[*], *G. Szebényi, A. Toldy*

Department of Polymer Engineering, Faculty of Mechanical Engineering, Budapest University of Technology and Economics, Műegyetem rkp. 3., H-1111 Budapest, Hungary

Received 19 June 2014; accepted in revised form 17 August 2014

Abstract. Curing and rheological behaviour, glass transition temperature, mechanical and thermal properties of two newly synthesized glucopyranoside- (GPTE) and glucofuranoside- (GFTE) based renewable epoxy resin (EP) components were investigated and compared to aromatic and aliphatic EPs. The glucose-based EPs can be successfully cured with amine and anhydride type curing agents, their gel times are suitable for processing and can be well-adopted to the needs of the common composite preparation methods. GPTE showed the highest glass transition temperature (T_g) among all investigated resins, followed by GFTE and DGEBA. Below the T_g there was no significant difference between the storage modulus values of the EP systems. The glucose-based EPs had lower tensile and bending strength, but their tensile modulus values are not significantly different from the mineral oil based EPs. The thermal stability of the synthesized GPTE and GFTE is between DGEBA and the aliphatic resins. In applications where bending stresses are dominant over the tensile ones, and outstanding T_g is required, these glucose-based resins offer a feasible renewable option.

Keywords: *biopolymers, high glass temperature, thermal properties, mechanical properties, aircraft applications*

1. Introduction

In the recent years intensive research work has been focused on the partial or full replacement of the mineral oil based epoxy resin (EP) components by renewable ones in several industrial segments in order to reduce their dependence on petrochemicals. The synthesis of bio-based EPs is feasible from different natural materials such as wood biomass [1], industrial lignin [2] and starch [3]. One of the most common methods to prepare bio-based EPs is the epoxidation of different vegetable oils, which are basically fatty acid esters of glycerol [4–8]. For the functionalization of plant oils (epoxidation of the unsaturated fatty acid chains double bonds) many chemical solutions were worked out [9, 10]. Basically there are four methods: epoxidation with percarboxylic acids; with inorganic or organic peroxides; with halohydrines or with molecular oxygen [11]. Many investigations deal with the mechanical properties of the neat epoxidized plant oils (EPOs) and mixed EPO/petrol oil based EP (mostly DGEBA – diglycidyl ether of bisphenol A) systems [12–26]. According to the literature in these hybrid EP systems usually phase separation was observed [12, 20, 21]. In all cases the glass transition temperature (T_g), thermal, tensile and bending properties decreased by increasing EPO-content, so the EPOs behaved basically as plasticizers. On the other hand, the impact strength of petrol oil based EPs increased at 20 mass% EPO-content [13], and the epoxidized triglycerides were tougher than DGEBA [14]. Besides the mechanical properties, the curing process also was investigated

[*]Corresponding author, e-mail: niedermann@pt.bme.hu

with many types of curing agents [19, 22]. With synthetic aliphatic EP components, the T_g values increased with increasing ESO-content, followed by a slight decrease in mechanical properties [26]. Based on the literature, the EPOs can be applied as renewable sourced polymer matrices in fiber reinforced polymer composites, however high-tech applications as aeronautical require much higher T_g and better mechanical properties.

Sugar is a renewable resource that has the potential to replace mineral oil in the synthesis of EPs, furthermore due to its large oversupply in the recent decades its application as base material in polymer synthesis does not compete with the food industry. Sugar based EP components can be synthesized by replacing the hydroxyl groups of sugar structured molecules as cardanol [27–29], sucrose [30, 31], maltitol, sorbitol [32] and isosorbide [33–36] with oxirane functions. With the mixture of a novel synthesized cardanol based novolac-type phenolic resins and polybutadiene liquid rubber (CTPB) tensile strength improvement and higher thermal stability could be achieved with increasing CTPB-content. [27]. With poly(butadiene-co-acrylonitrile) (CTBN) the tensile strength decreased, but with 15 mass% CTBN-content, the impact strength increased [28, 29]. Cured epoxy allyl sucrose (EAS) and epoxy crotyl sucrose (ECS) were compared to DGEBA by Pan *et al*. [30]. The EAS had lower and the ECS had higher tensile strength and modulus than the DGEBA. From sucrose based starting materials cured epoxidized sucrose ester of fatty acids can be formed, which has higher tensile strength and modulus than the commercially available epoxidized soybean oil (ESO) [31]. Shibata *et al*. [32] achieved tensile strength improvement with 10 mass% microfibrillated cellulose fiber reinforcement in glycerol polyglycidyl ether (GPE) and sorbitol polyglycidyl ether (SPE) matrix materials. Isosorbide is also an alternative source to synthesize renewable sourced epoxy components [33–35]. Chrisanthos *et al*. [36] synthesized two hygroscopic isosorbide based EP components. The mechanical properties of renewable sourced cured EP components were compared to DGEBA. They reached higher rubbery modulus above T_g, but the T_g values were lower than in the case of DGEBA.

In this work curing and rheological behaviour, glass transition temperature, mechanical and thermal properties of two novel glucose-based EP components were investigated. These results were not only compared to the conventional, widely investigated aromatic diglycidyl ether of bisphenol A (DGEBA) resin, but also to a glycerol- (GER) and a pentaerythritol-based (PER) aliphatic resin, which are currently synthesized on mineral oil base, however they can be potentially synthesized from renewable sources: glycerol is available in large quantities from natural fatty acids, while pentaerythritol can be produced from bio-based methanol as well. The expected outcome of this study was to determine the potential application areas, where these newly developed glucose-based EP components are capable of replacing the mineral oil based commodity resins.

2. Experimental

2.1. Materials

As renewable epoxy resin components two glucose-based components, synthesized previously by the research group of the authors [37], were used: a solid glucopyranoside based trifunctional epoxy resin component (GPTE) and a liquid glucofuranoside based trifunctional epoxy resin component (GFTE).

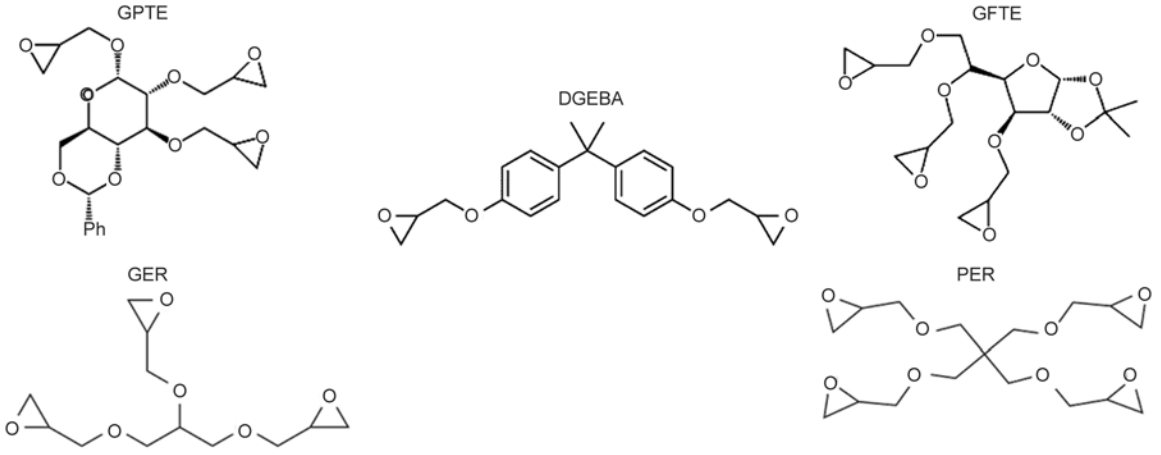

Figure 1. Chemical structure of the applied EP components

Table 1. Characteristics of the applied EP components

Abbreviation	Main component	Supplier	Trade name	Phase / Structure / Viscosity [Pa·s] (at 25°C) [–]	Molecular weight [g/mol]	Epoxy equivalent weight (EEW) [g/eq]
GPTE	(2′,3′-epoxypropyl)-2,3-di-O-(2′,3′-epoxypropyl)-4,6-O-benzylidene-α-D-glucopyranoside	synthesized at Budapest University of Technology and Economics [37]	–	Solid / Cycloaliphatic	436	160
GFTE	3,5,6-tri-O-(2,3-epoxypropyl)-1,2-O-isopropylidene-α-D-glucofuranose	synthesized at Budapest University of Technology and Economics [37]	–	Liquid / Cycloaliphatic / 3.76	388	160
DGEBA	Diglycidyl ether of bisphenol A	IPOX Chemicals Ltd. (Budapest, Hungary)	ER1010	Liquid / Aromatic / 10–14	340	188
GER	Triglycidyl ether of glycerol	IPOX Chemicals Ltd. (Budapest, Hungary)	MR3012	Liquid / Aliphatic / 0.9	274	144
PER	Tetraglycidyl ether of pentaerythritol	IPOX Chemicals Ltd. (Budapest, Hungary)	MR3016	Liquid / Aliphatic / 0.24	360	168

As conventional mineral oil based resins the bifunctional aromatic bisphenol-A based DGEBA and two aliphatic components, the trifunctional glycerol-based GER and the tetrafunctional pentaerythritol-based PER were used. The chemical structure of these components can be seen in Figure 1, while their characteristics are listed in Table 1.

As hardener two types of curing agents were applied: an amine and an anhydride with accelerator. The amine curing agent was diethylene-toluene-tetramine with 45 g/eq hydrogen equivalent (DETDA80 – DETDA) by Lonza (Basel, Switzerland). The anhydride was methyl-tetrahydrophtalic-anhydride with minimal tetrahydrophtalic anhydride content (Aradur 917 – AR917) with 1-methylimidazole (DY070) accelerator by Huntsman Advanced Materials (Basel, Switzerland). The equivalent mass of the anhydride type curing agent, calculated form its molecular mass, was 160 g/eq. The accelerator was applied in 2 mass% related to the mass of the epoxy resin component. During the composite preparation in all cases stoichiometric ratio of EP component and hardener was used. The macro scaled specimens for the mechanical investigations were made by resin moulding with a vertical moulding tool. The curing procedure, determined on the basis of DSC and gel time tests, consisted of the following isothermal heat steps: 1 h at 100°C, 1 h at 150°C and 2 h at 175°C in the case of DETDA, and 2 h at 100°C and 2 h and 140°C with AR917.

2.2. Methods

2.2.1. Differential scanning calorimetry (DSC)

The DSC tests were carried out with Q2000 device of TA Instruments (New Castle, DE, USA) in 50 mL/min nitrogen flow. Tzero type aluminium pans were used, the sample mass was 5–10 mg. For the investigation of the curing process of the samples the applied three-step temperature program consisted of heat/cool/heat cycles: after a linear ramp from 25–250°C with 5°C/min heat rate (first cycle), the sample was cooled down to 0°C with 50°C/min cooling rate, followed by a second linear heating ramp from 0–250°C with 5°C/min heating rate (second cycle) to ensure the proper conversion. The glass transition temperature (T_g) values were determined from the second heating scan and were defined as the inflection point of the transition curve. After the heat/cool/heat cycle isothermal measurements were carried out as well to determine proper curing circumstances for macro-scaled specimen preparation. After carrying out the specific curing cycles on macro-scaled samples, determined on the basis of DSC results and gel time, the conversion of the specimens was checked by applying a linear heating ramp from 0–250°C with 5°C/min heating rate. If no postcuring was detected, the conversion was considered as complete.

2.2.2. Parallel plate rheometry

Gel time was determined by parallel plate rheometry using AR2000 device from TA Instruments (New Castle, DE, USA) with 25 mm diameter plate and 200 μm gap between the plates in oscillation mode. The test frequency was 10 Hz, the applied temperature was 100°C. The gel time was determined from the intersection of the recorded shear storage (G') and shear loss (G'') modulus values.

2.2.3. Dynamic mechanical analysis (DMA)

For the investigations of the dynamic mechanical properties and for the determination of the T_g values

DMA tests were carried out in three point bending setup with TA Q800 device of TA Instruments (New Castle, DE, USA). The temperature range was 25–225°C with 3°C/min heat rate. The frequency was 1 Hz. The size of the specimens was 50×10×2 mm (length × width × thickness), and the support span was 50 mm. The amplitude was strain controlled with 0.1% relative strain.

2.2.4. Tensile test

To determine the epoxy systems tensile strength and Young's modulus a Zwick Z005 (Ulm, Germany) type computer controlled universal tester was used with a 5 kN load cell. The specimen dimensions were 100×10×2 mm (length × width × thickness) according to EN ISO 527-3. The initial test length was 100 mm. The test speed was 2 mm/min. The temperature was 22°C and the relative humidity was 58.3%.

2.2.5. Bending test

To determine the bending strength and bending modulus values of the epoxy systems three point bending tests were carried out according to EN ISO 178 with a Zwick Z005 (Ulm, Germany) type computer controlled universal tester with 5 kN load cell. The specimen size was 40×25×2 mm (length × width × thickness), and the support span was 32 mm. The test speed was 2 mm/min. The temperature was 22°C and the relative humidity was 58.3%.

2.2.6. Hardness

To investigate the hardness of the various epoxy systems with anhydride and amine type curing agents Shore-D type hardness was determined with Zwick (Ulm, Germany) H04.3150 hardness tester.

2.2.7. Thermogravimetrical analysis (TGA)

The TGA measurements were carried out with a Setaram Labsys (Caluire, France) type TGA device. The heating range was 30–700°C with 10°C/min heating rate in nitrogen atmosphere. Setaram type 400 µL aluminium oxide pan was used. The sample size was 15–20 mg. From the recorded TG data dTG values were calculated by Setaram Setsys software.

3. Results and discussion

3.1. Curing behaviour

To study the curing behaviour of the novel glucose-based epoxy resin components and compare them to the mineral oil based ones, DSC measurements were carried out. Figure 2 shows the first DSC heating cycle of the EP systems with amine (DETDA) and anhydride (AR917) type curing agents and Table 2 summarizes the DSC results.

According to Figure 2 and Table 2, both novel glucose-based resins could be successfully cured both with amine and anhydride type curing agents. In case of AR917 no significant difference could be noticed between the heat flow profile of the different EPs, the curing occurred in rather narrow temperature zone, with a peak temperature around 130°C. The curing process was significantly slower in the case of DETDA and the EP systems needed higher curing temperature than with AR917. The aliphatic

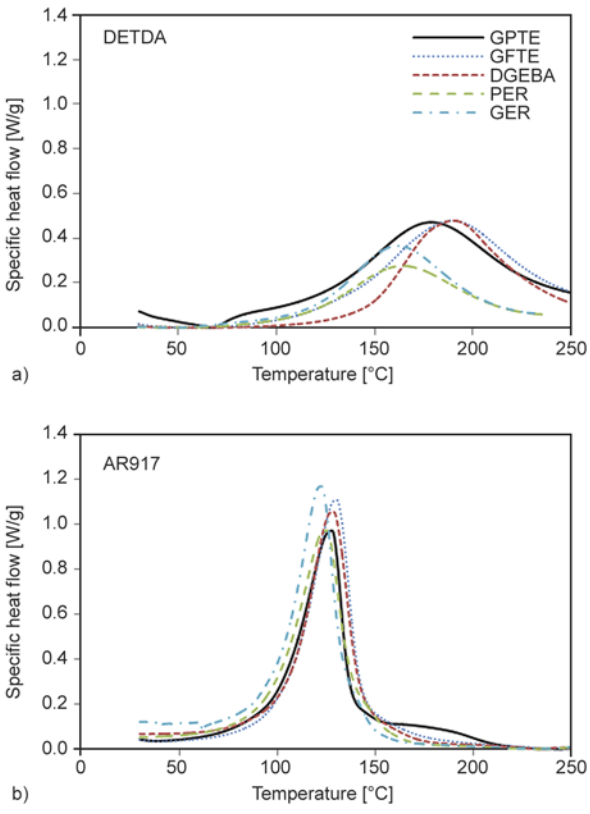

Figure 2. Curing process of the EP systems with DETDA (a) and AR917 (b) curing agents (first DSC cycle)

Table 2. DSC results of the EP systems with DETDA and AR917 curing agents

Base resin	GPTE		GFTE		DGEBA		PER		GER	
Curing agent	DETDA	AR917	DETDA	AR917	DETDA	AR917	DETDA	AR917	DETDA	AR917
Total specific reaction enthalpy [J/g]	365.9	396.3	332.6	414.5	295.6	380.6	327.9	388.1	418.7	371.7
Peak [°C]	179	133	190	130	190	129	164	125	162	123
T_g [°C]	210	178	173	157	179	155	98	116	76	99

resins cured at lower temperature, while the heat flow curve of the aromatic DGEBA and cycloaliphatic glucose-based resins was shifted to higher temperatures.

As for the T_g values, according to Table 2, the aromatic and glucose-based systems had higher T_g with the aromatic amine type DETDA than with anhydride type AR917 curing agent, while the aliphatic ones had lower T_g with DETDA. GPTE type glucose-based EP systems showed the highest T_g values among all investigated resins, followed by glucose-based cycloaliphatic GFTE and aromatic DGEBA, while the aliphatic ones had the lowest values, as expected.

3.2. Gelling

Prior to specimen moulding the gel time of the EP systems was determined as well. The applied temperature during the measurement was determined on the basis of DSC results: with DETDA a constant temperature of 175°C, while with AR917 100°C was applied. Table 3 shows the gel times of the EP systems with DETDA (at 175°C) and AR917 (at 100°C). Table 3 shows that curing with amine type DETDA leads to shorter gel times than curing with the anhydride type AR917 in all EP systems. In case of AR917 the glucose-based EP systems had similar gel times than DGEBA, while with DETDA the glucose-based EP components have significantly lower gel times than the DGEBA. With both curing agents the aliphatic resins showed the highest reactivity. According to these results, the gel times of the novel glucose-based resins are appropriate for processing and can be well-adopted to the requirements of the common composite preparation method by choosing the type of the curing agent.

Table 3. Gel times of the EP systems with DETDA and AR917 curing agents

		Base resin				
	Curing agent	**GPTE**	**GFTE**	**DGEBA**	**PER**	**GER**
t_{gel} [s]	DETDA	586	552	862	448	420
	AR917	955	908	935	532	769

3.3. Dynamic mechanical properties

In order to compare the dynamic mechanical properties of the glucose-based EP systems compared to the mineral oil based ones, DMA measurements were carried out. The storage modulus and loss factor (tan δ) values in the function of temperature can be seen in Figure 3.

The storage moduli of the different EP systems were compared at 0, 25, 50 and 75°C. From the peak position of tan δ curves in the function of temperature, T_g values of the EP systems were determined. Table 4 shows the storage modulus at 0, 25, 50 and 75°C and compares the T_g values determined by DSC and DMA.

According to Table 4 there was no significant difference between the storage modulus values of the EP systems below the T_g. The storage modulus of the novel glucose-based resins at lower temperatures is higher than the values of DGEBA, and above 50°C it still in the same region of the storage modulus of DGEBA. In the case of PER and GER 75°C is close to the T_g of these aliphatic systems, which explains the low storage modulus values at this temperature. The T_g values determined by DMA showed similar tendency than the ones determined by DSC: the glucose-based aliphatic GPTE had much higher T_g than DGEBA both with amine type DETDA and anhydride type AR917, while the T_g values of GFTE were in the same range as DGEBA.

3.4. Mechanical properties

In order to compare mechanical properties and hardness of the glucose-based EP resins to the mineral oil based ones, tensile, bending and Shore-D type

Table 4. Storage modulus measured by DMA and T_g values determined by DSC and DMA in EP systems cured with DETDA and AR917 curing agents

		Storage modulus [MPa]									
Base resin		**GPTE**		**GFTE**		**DGEBA**		**PER**		**GER**	
Curing agent		**DETDA**	**AR917**	**DETDA**	**AR917**	**DETDA**	**AR917**	**DETDA**	**AR917**	**DETDA**	**AR917**
Temperature [°C]	0	2895	3032	3058	2999	2648	2817	3078	3239	2965	2970
	25	2558	2877	2727	2804	2409	2716	2376	3049	2386	2767
	50	2274	2716	2341	2611	2155	2627	1512	2832	1076	2567
	75	2072	2528	2034	2440	2005	2559	555	2532	45	2343
T_g [°C]											
Method	DMA	213	188	178	161	177	154	86	115	65	98
	DSC	210	178	173	157	179	155	98	116	76	99

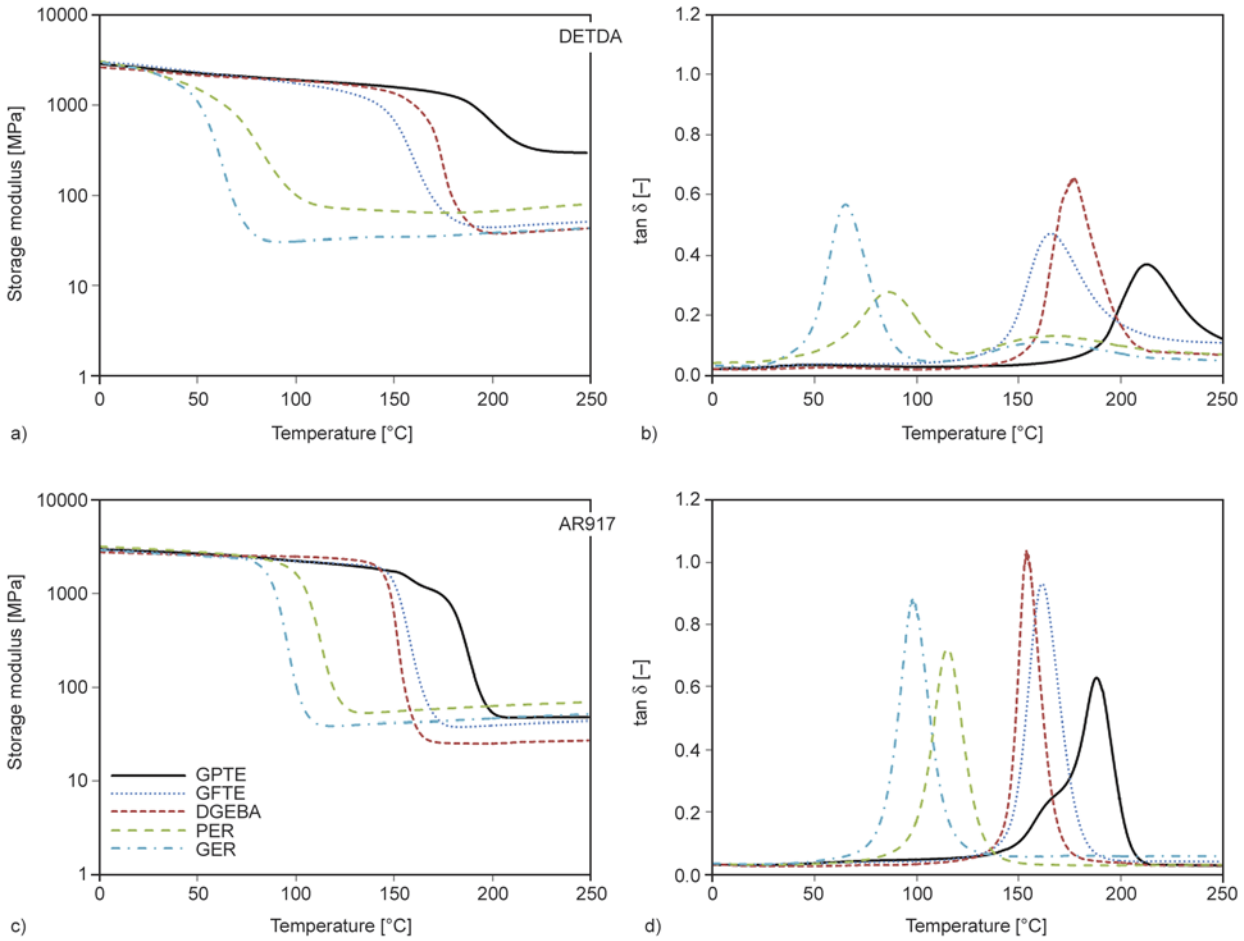

Figure 3. Storage modulus and tan δ curves of EP systems with DETDA (a, b) and AR917 (c, d) curing agents

hardness tests were carried out. From the measured force and crosshead travel values, tensile strength and Young's modulus, bending strength and bending modulus were determined (Table 5).

Based on the results showed in Table 5, DGEBA has the highest tensile strength both with DETDA and AR917 curing agent. Noteworthy worsening in the tensile strength was detected in the case of the glucose-based EP components (GPTE, GFTE) compared to the mineral oil based ones. All EP systems have lower tensile strength with amine type DETDA than with anhydride type AR917, which may be explained with the high temperature heat treatment (2 h at 175°C) necessary for proper conversion, probably causing already degradation in the crosslinked resin. Despite the tendency in tensile strength values, the GPTE and GFTE with AR917 have almost the highest Young's modulus value. Similar trend

Table 5. Comparison of the mechanical properties and hardness of glucose-based EP resins to mineral oil based ones with DETDA and AR917 curing agents

Base resin		**GPTE**		**GFTE**		**DGEBA**		**PER**		**GER**	
Curing agent		**DETDA**	**AR917**	**DETDA**	**AR917**	**DETDA**	**AR917**	**DETDA**	**AR917**	**DETDA**	**AR917**
Tensile strength [MPa]	Average value	14.67	24.90	29.02	37.58	44.80	77.61	34.88	64.69	46.81	66.92
	Standard deviation	4.01	4.08	8.75	9.13	14.18	0.79	9.97	0.78	0.32	0.34
Young's modulus [GPa]	Average value	2.23	2.50	2.48	2.66	2.26	2.54	2.27	2.66	2.33	2.66
	Standard deviation	0.06	0.07	0.05	0.11	0.07	0.04	0.02	0.05	0.04	0.07
Bending strength [MPa]	Average value	49.11	86.86	62.84	68.86	86.84	94.87	85.85	91.67	85.81	94.41
	Standard deviation	10.07	25.82	8.02	5.71	1.39	0.77	0.59	0.52	1.79	0.21
Bending modulus [GPa]	Average value	2.29	2.61	2.31	2.51	2.12	2.88	2.50	3.12	2.30	3.01
	Standard deviation	0.12	0.12	0.47	0.16	0.10	0.03	0.01	0.02	0.28	0.02
Hardness [Shore-D]	Average value	105.72	107.82	107.28	109.06	103.98	106.20	99.64	107.12	99.32	105.84
	Standard deviation	2.52	1.94	1.59	1.05	1.93	0.57	2.18	0.53	2.05	0.65

can be seen in the case of the bending properties. The bending strength of the glucose-based EP systems is lower than the synthetic resins except the GPTE with AR917. The bending modulus values are the lowest in the case of the glucose-based epoxy components with DETDA. Basically the glucose-based and the mineral oil based epoxy components' modulus values are comparable with each other using the same curing agent.

According to the hardness tests, the glucose-based epoxy components have the highest hardness among all the five examined EP components with both curing.

3.5. Thermal behaviour

Thermal stability of the synthesized bio-based epoxy resins, GPTE and GFTE was compared to the stability of the applied aliphatic and aromatic synthetic resins (DGEBA, PER, GER) both in case of anhydride (AR917) and aromatic amine type hardener (DETDA). Figure 4 shows the TG and dTG curves of all epoxy resin systems with DETDA and AR917 curing agents.

Table 6 shows the temperature at 5 and 50 mass% loss ($T_{5mass\%}$; $T_{50mass\%}$), the maximum mass loss rate (dTG_{max}), the temperature belonging to this value (T_{dTGmax}) and the char yield at the end of the TGA test (at 700°C).

Based on these results, the aromatic DGEBA had the highest thermal stability, the stability of the synthesized GPTE and GFTE is between the aliphatic resins and DGEBA. In the case of the glucose-based resins, the char yield values are significantly

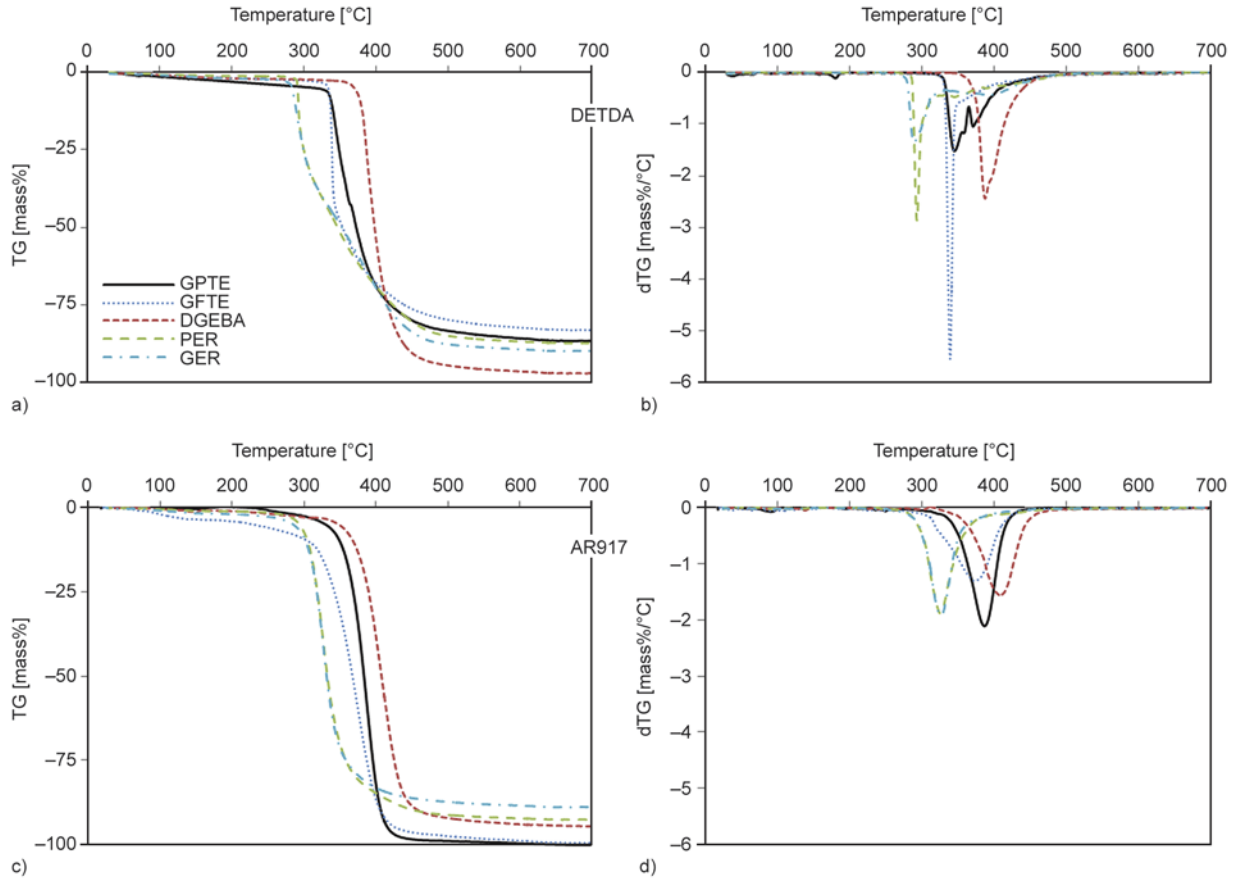

Figure 4. TG and dTG curves in function of temperature of the EP components with DETDA (a, b) and AR917 (c, d) curing agents

Table 6. $T_{5mass\%}$; $T_{50mass\%}$; dTG_{max}; T_{dTGmax} and char yield values of the EP systems with DETDA and AR917 curing agents

Base resin	GPTE		GFTE		DGEBA		PER		GER	
Curing agent	DETDA	AR917	DETDA	AR917	DETDA	AR917	DETDA	AR917	DETDA	AR917
$T_{5mass\%}$ [°C]	314	330	334	229	370	348	291	294	284	285
$T_{50mass\%}$ [°C]	373	384	354	367	398	408	347	333	353	331
dTG_{max} [mass%/°C]	–1.52	–2.11	–5.55	–1.31	–2.44	–1.56	–2.87	–1.88	–1.36	–1.92
T_{dTGmax} [°C]	345	387	339	374	387	409	293	325	289	327
Char yield [mass%]	13.35	0.21	16.83	0.54	2.89	10.29	12.64	15.94	10.11	15.76

higher with DETDA than with AR917, which may be explained by the high amount of ether type linkages derived from hydroxyl groups, which leads to the formation of an intumescent system when amine type hardeners are used [38].

4. Conclusions

Curing and rheological behaviour, glass transition temperature, mechanical and thermal properties of two novel glucose-based (GPTE, GFTE) EP components were investigated. The results were compared to the conventional, widely investigated aromatic DGEBA EP resin and as well as to GER and PER aliphatic EP resins, which are currently synthesized on mineral oil basis, but can be potentially produced from renewable sources.

According to the DSC results, the novel glucose-based resins could be successfully cured both with amine and anhydride type curing agents. In all investigated EPs the curing process was significantly slower and therefore higher curing temperatures were necessary with amine type hardener. As for the T_g values, GPTE type glucose-based EP systems showed the highest T_g values among all investigated resins, followed by glucose-based cycloaliphatic GFTE and aromatic DGEBA, while the aliphatic ones had the lowest values, as expected.

As for the gelling properties, the glucose-based EPs had similar gel times with anhydride curing agent as DGEBA, while with amine hardener their gel time was significantly lower than in case of DGEBA.

According to the DMA test results there was no significant difference between the storage modulus values of the EP systems below the T_g. The storage modulus of the novel glucose-based resins is higher or above 50°C it is in the same region as the storage modulus of DGEBA. The T_g values determined by DMA showed similar tendency than the values determined by DSC.

According to the mechanical test results, the glucose based EP systems have lower tensile and bending strength, but the tensile modulus values are not significantly different from the synthetic EPs.

Based on the TGA measurements, the stability of the synthesized GPTE and GFTE is between the aliphatic resins and DGEBA. In the case of the glucose-based resins, the char yield values are significantly higher with DETDA than with AR917, which may be explained by the high amount of ether type linkages derived from hydroxyl groups, which leads to the formation of an intumescent system when amine type hardeners are used.

Based on the results, the newly synthesized glucopyranoside- and glucofuranoside-based renewable EP components are promising candidates to replace the commodity mineral oil based ones. Their major advantages are the high T_g (in some cases above 200°C), adjustable gel time by choosing appropriate curing agent, high storage modulus values and hardness. In applications where bending stresses are dominant over the tensile ones, and outstanding T_g is required, these sugar-based resins offer a feasible renewable choice.

Acknowledgements

The research leading to these results has received funding from the European Union's Seventh Framework Programme (FP7/2007-2013) for the Clean Sky Joint Technology Initiative under grant agreement no 298090 (Topic manager: Dassault Aviation).

This work is connected to the scientific program of the 'Development of quality-oriented and harmonized R+D+I strategy and functional model at BME' and 'Talent care and cultivation in the scientific workshops of BME' project. This project is supported by New Széchenyi Plan (Project ID: TÁMOP-4.2.1/B-09/1/KMR-2010-0002), by NFÜ EU_BONUS_12-1-2012-0026, by TÁMOP – 4.2.2.B-10/1;2010-0009. Andrea Toldy acknowledges the financial support received through János Bolyai Scholarship of the Hungarian Academy of Science.

References

[1] Koike T.: Progress in development of epoxy resin systems based on wood biomass in Japan. Polymer Engineering and Science, **52**, 701–717 (2012). DOI: 10.1002/pen.23119

[2] Huijbrechts A. A. M. L., Huang J., Schols H. A., van Langen B., Visser G. M., Boeriu C. G., Sudhölter E. J. R.: 1-Allyloxy-2-hydroxy-propyl-starch: Synthesis and characterization. Journal of Polymer Science Part A: Polymer Chemistry, **45**, 2734–2744 (2007). DOI: 10.1002/pola.22029

[3] Huijbrechts A. M. L., ter Haar R., Schols H. A., Franssen M. C. R., Boeriu C. G., Sudhölter E. J. R.: Synthesis and application of epoxy starch derivatives. Carbohydrate Polymers, **79**, 858–866 (2010). DOI: 10.1016/j.carbpol.2009.10.012

[4] Liu X. Q., Huang W., Jiang Y. H., Zhu J., Zhang C. Z.: Preparation of a bio-based epoxy with comparable properties to those of petroleum-based counterparts. Express Polymer Letters, **6**, 293–298 (2012). DOI: 10.3144/expresspolymlett.2012.32

[5] Sarwono A., Man Z., Bustam M. A.: Blending of epoxidised palm oil with epoxy resin: The effect on morphology, thermal and mechanical properties. Journal of Polymers and the Environment, **20**, 540–549 (2012). DOI: 10.1007/s10924-012-0418-5

[6] Güner F. S., Yağc i Y., Erciyes A. T.: Polymers from triglyceride oils. Progress in Polymer Science, **31**, 633–670 (2006). DOI: 10.1016/j.progpolymsci.2006.07.001

[7] Tan S. G., Chow W. S.: Biobased epoxidized vegetable oils and its greener epoxy blends: A review. Polymer-Plastics Technology and Engineering, **49**, 1581–1590 (2010). DOI: 10.1080/03602559.2010.512338

[8] Wang R., Schuman T. P.: Vegetable oil-derived epoxy monomers and polymer blends: A comparative study with review. Express Polymer Letters, **7**, 272–292 (2013). DOI: 10.3144/expresspolymlett.2013.25

[9] Khot S. N., Lascala J. J., Can E., Morye S. S., Williams G. I., Palmese G. R., Kusefoglu S. H., Wool R. P.: Development and application of triglyceride-based polymers and composites. Journal of Applied Polymer Science, **82**, 703–723 (2001). DOI: 10.1002/app.1897

[10] Can E., Küsefoğlu S., Wool R. P.: Rigid thermosetting liquid molding resins from renewable resources. II. Copolymers of soybean oil monoglyceride maleates with neopentyl glycol and bisphenol A maleates. Journal of Applied Polymer Science, **83**, 972–980 (2002). DOI: 10.1002/app.2277

[11] Guenter S., Rieth R., Rowbotton K. T.: Ullmann's encyclopedia of industrial chemistry, 6th edition. Wiley, New York (2003).

[12] Ratna D.: Mechanical properties and morphology of epoxidized soyabean-oil-modified epoxy resin. Polymer International, **50**, 179–184 (2001). DOI: 10.1002/1097-0126(200102)50:2<179::AID-PI603>3.0.CO;2-E

[13] Zhu J., Chandrashekhara K., Flanigan V., Kapila S.: Curing and mechanical characterization of a soy-based epoxy resin system. Journal of Applied Polymer Science, **91**, 3513–3518 (2004). DOI: 10.1002/app.13571

[14] Earls J. D., White J. E., López L. C., Lysenko Z., Dettloff M. L., Null M. J.: Amine-cured ω-epoxy fatty acid triglycerides: Fundamental structure–property relationships. Polymer, **48**, 712–719 (2007). DOI: 10.1016/j.polymer.2006.11.060

[15] Li J., Du Z., Li H., Zhang C.: Porous epoxy monolith prepared via chemically induced phase separation. Polymer, **50**, 1526–1532 (2009). DOI: 10.1016/j.polymer.2009.01.049

[16] Mustata F., Tudorachi N., Rosu D.: Curing and thermal behavior of resin matrix for composites based on epoxidized soybean oil/diglycidyl ether of bisphenol A. Composites Part B: Engineering, **42**, 1803–1812 (2011). DOI: 10.1016/j.compositesb.2011.07.003

[17] Park S-J., Jin F-L., Lee J-R.: Thermal and mechanical properties of tetrafunctional epoxy resin toughened with epoxidized soybean oil. Materials Science and Engineering A, **374**, 109–114 (2004). DOI: 10.1016/j.msea.2004.01.002

[18] Park S-J., Jin F-L., Lee J-R.: Effect of biodegradable epoxidized castor oil on physicochemical and mechanical properties of epoxy resins. Macromolecular Chemistry and Physics, **205**, 2048–2054 (2004). DOI: 10.1002/macp.200400214

[19] Gerbase A. E., Petzhold C. L., Costa A. P. O.: Dynamic mechanical and thermal behavior of epoxy resins based on soybean oil. Journal of the American Oil Chemists' Society, **79**, 797–802 (2002). DOI: 10.1007/s11746-002-0561-z

[20] Miyagawa H., Misra M., Drzal L. T., Mohanty A. K.: Fracture toughness and impact strength of anhydride-cured biobased epoxy. Polymer Engineering and Science, **45**, 487–495 (2005). DOI: 10.1002/pen.20290

[21] Altuna F. I., Espósito L. H., Ruseckaite R. A., Stefani P. M.: Thermal and mechanical properties of anhydride-cured epoxy resins with different contents of biobased epoxidized soybean oil. Journal of Applied Polymer Science, **120**, 789–798 (2011). DOI: 10.1002/app.33097

[22] Gupta A. P., Ahmad S., Dev A.: Modification of novel bio-based resin-epoxidized soybean oil by conventional epoxy resin. Polymer Engineering and Science, **51**, 1087–1091 (2011). DOI: 10.1002/pen.21791

[23] Karger-Kocsis J., Grishchuk S., Sorochynska L., Rong M. Z.: Curing, gelling, thermomechanical, and thermal decomposition behaviors of anhydride-cured epoxy (DGEBA)/epoxidized soybean oil compositions. Polymer Engineering and Science, **54**, 747–755 (2013). DOI: 10.1002/pen.23605

[24] Kim J. R., Sharma S.: The development and comparison of bio-thermoset plastics from epoxidized plant oils. Industrial Crops and Products, **36**, 485–499 (2012). DOI: 10.1016/j.indcrop.2011.10.036

[25] Jin F-L., Park S-J.: Thermal and rheological properties of vegetable oil-based epoxy resins cured with thermally latent initiator. Journal of Industrial and Engineering Chemistry, **13**, 808-814 (2007).

[26] Niedermann P., Szebényi G., Toldy A.: Effect of epoxidized soybean oil on curing, rheological, mechanical and thermal properties of aromatic and aliphatic epoxy resins. Journal of Polymers and the Environment, in press (2014). DOI: 10.1007/s10924-014-0673-8

[27] Devi A., Srivastava D.: Studies on the blends of cardanol-based epoxidized novolac resin and CTPB. European Polymer Journal, **43**, 2422–2432 (2007). DOI: 10.1016/j.eurpolymj.2007.03.006

[28] Yadav R., Awasthi P., Srivastava D.: Studies on synthesis of modified epoxidized novolac resin from renewable resource material for application in surface coating. Journal of Applied Polymer Science, **114**, 1471–1484 (2009).
DOI: 10.1002/app.30581

[29] Yadav R., Srivastava D.: Studies of cardanol-based epoxidized novolac resin and its blends. Chemistry and Chemical Technology, **2**, 173–184 (2008).

[30] Pan X., Sengupta P., Webster D. C.: High biobased content epoxy–anhydride thermosets from epoxidized sucrose esters of fatty acids. Biomacromolecules, **12**, 2416–2428 (2011).
DOI: 10.1021/bm200549c

[31] Sachinvala N. D., Winsor D. L., Menescal R. K., Ganjian I., Niemczura W. P., Litt M. H.: Sucrose-based epoxy monomers and their reactions with diethylenetriamine. Journal of Polymer Science Part A: Polymer Chemistry, **36**, 2397–2413 (1998).
DOI: 10.1002/(SICI)1099-0518(19980930)36:13<2397::AID-POLA27>3.0.CO;2-4

[32] Shibata M., Nakai K.: Preparation and properties of biocomposites composed of bio-based epoxy resin, tannic acid, and microfibrillated cellulose. Journal of Polymer Science Part B: Polymer Physics, **48**, 425–433 (2010).
DOI: 10.1002/polb.21903

[33] Feng X., East A. J., Hammond W. B., Zhang Y., Jaffe M.: Overview of advances in sugar-based polymers. Polymers for Advanced Technologies, **22**, 139–150 (2011).
DOI: 10.1002/pat.1859

[34] Fenoulliot F., Rousseau A., Colomines G., Saint-Loup R., Pascault J-P.: Polymers from renewable 1,4:3,6-dianhydrohexitols (isosorbide, isomannide and isoidide): A review. Progress in Polymer Science, **35**, 578–622 (2010).
DOI: 10.1016/j.progpolymsci.2009.10.001

[35] Lukaszczyk J., Janicki B., Kaczmarek M.: Synthesis and properties of isosorbide based epoxy resin. European Polymer Journal, **47**, 1601–1606 (2011).
DOI: 10.1016/j.eurpolymj.2011.05.009

[36] Chrysanthos M., Galy J., Pascault J-P.: Preparation and properties of bio-based epoxy networks derived from isosorbide diglycidyl ether. Polymer, **52**, 3611–3620 (2011).
DOI: 10.1016/j.polymer.2011.06.001

[37] Rapi Zs., Bakó P., Keglevich Gy., Bodzay B., Szolnoki B., Niedermann P., Toldy A., Marosi Gy.: Synthesis and characterization of bio-based epoxy resin components derived from D-glucose. European Polymer Journal, in press (2014).
DOI: 10.1016/j.eurpolymj.2014.09.025

[38] Le Bras M., Camino G., Bourbigot S., Delobel R.: Fire retardancy of polymers: The use of intumescence. The Royal Chemical Society, Cambridge (1998).

eXPRESS Polymer Letters Vol.9, No.2 (2015) 95–104
Available online at www.expresspolymlett.com
DOI: 10.3144/expresspolymlett.2015.11

Low-cost replication of self-organized sub-micron structures into polymer films

H. Stenberg[1], *P. Stenberg*[2], *L. Takkunen*[1], *M. Kuittinen*[2], *M. Suvanto*[1], *T. T. Pakkanen*[1*]

[1]University of Eastern Finland, Department of Chemistry, P.O.Box 111, FIN-80101 Joensuu, Finland
[2]University of Eastern Finland, Institute of Photonics, P.O.Box 111, FIN-80101 Joensuu, Finland

Received 9 May 2014; accepted in revised form 20 August 2014

Abstract. In this paper, the results of exploiting self-organized sub-micron polystyrene (PS) wrinkle patterns possessing random orientation, in preparation of a nickel stamp for hot embossing purposes, are presented. Self-organized patterns were prepared employing a method in which a stiff cross-linked capping layer on the topmost part of the soft polystyrene layer was created by using reactive ion etching (RIE) device with mild conditions and argon as a process gas, and the wrinkle formation was initiated thermally. Different surface patternings were obtained using silicon and stainless steel (SST) wafers as substrates. Prepared Ni-stamps were employed in hot embossing of polycarbonate (PC) and cyclo-olefin polymer (COP) films, using a nano-imprinting process. The replication quality of the self-organized wrinkle structures in PC and COP films was monitored by comparing the shape and dimensions of the original and final surface structures. The hot embossed sub-micron scale features, originally formed on stainless steel substrate, were found to have influence on the optical properties of the PC and COP films by lowering their reflectances.

Keywords: *coatings, self-organization, hot-embossing, polystyrene, silicon*

1. Introduction

Pattern formation by self-organization, employing different kinds of layered systems, for example trilayered substrate/soft layer/superstrate or bilayered hard substrate/soft layer structures, has been studied quite actively during past decades [1–5]. Both theoretical [6–9] and experimental [10, 11] approaches have been used to explain the phenomenon. Utilization of the self-organized patterns in various applications is of high interest [12] and it has been applied for example in the case of curved photonic crystals by Kolaric *et al*. [13].

It has been found out that very different kinds of materials and methods can be employed for self-organizing coatings [14–18], or the whole process set-up can be designed from end-to-start, to obtain structures with desired shapes or sizes, as a result [19, 20]. The self-organizing pattern formation to be occurred, the structure of the layered system and materials employed must be appropriate for the process and fulfill certain requirements. For example in case of thermally induced self-organization sufficient difference in thermal expansion coefficients of individual layers is required. Also, the thickness of each material layer of the system must be optimum, for the stress driving self-organization to be developed. By tailoring the forming structures, the properties of the structured surface, like wetting or optical properties, can be influenced [21–23].

Hot embossing is a simple method to transfer desired structures into different thermoplastic polymer films [24]. The process parameters are set for each material according to the materials properties. Hot embossing enables production of different kinds of elements for e.g. optoelectronics or biomedical application purposes [25, 26]. Furthermore, the replication, car-

*Corresponding author, e-mail: tuula.pakkanen@uef.fi

ried out by hot embossing, is easily transferred to a time saving and cost effective, high-volume roll-to-roll manufacturing [27–29].

By combining the advantages of the self-organized pattern formation and the thermal imprint processing, large volumes of patterned polymer products with a specific sub-micron structuring can be prepared. For example Chou *et al*. [30], have previously introduced the utilization of the hot embossing with 25 nanometer resolution, but the original structures were obtained using electron beam lithography. Schweikart *et al*. [31], demonstrated the replication of periodic sub-micron sized wrinkles employing both micro thermoforming and molding process using epoxy resin.

In the present research, we demonstrate a controlled preparation of self-organized PS wrinkle patterns on top of silicon and stainless steel wafers and replication of these structures into polymer films by hot embossing via electro-plating the wrinkles into Ni stamps. This stepwise fabrication method enables development of characteristic and random sub-micron sized surface patterning over large surface areas without using any expensive equipments and processes. We show that the shape and size of the obtained surface structures can be influenced by varying the substrate material. Moreover, effects of this unique sub-micron sized structuring on the optical properties of the PC and COP polymer films are studied.

2. Materials and methods

Single-side polished silicon wafers (ø100 mm, <100>, Compart Technology Ltd.) and stainless steel (SST) wafers (ø100 mm, thickness 0.5 mm, Ruukki Metals) were cleaned 5 minutes in trichloroethylene and 5 minutes in methanol, using an ultrasonic treatment. The wafers were dried under nitrogen flow and kept in a desiccator in a nitrogen atmosphere. The native oxide layer was left intact.

The solution of PS and toluene, having the concentration of 10% (weight/volume), was prepared dissolving polystyrene with molar mass of 192 000 g/mol (Sigma-Aldrich Co.) in toluene (Merck KGaA, 99.9 %) under mixing and heating. Cleaned wafers were coated by the PS/toluene solution (PS layer thickness on Si 1.5 μm, and on SST 0.5 μm) employing a spin-coating technique (Laurell technologies Co., WS-400A–6NPP/LITE/10K spin-coater). Coated wafers were kept at 60°C for 12 hours to remove the remaining solvent and stress generated in spin-coating.

2.1. Preparation of the self-organized PS coating

Coated wafers were plasma treated (Oxford Instruments, Plasmalab80Plus) using reactive ion etching (RIE) equipment with mild conditions (plasma power = 30 W, pressure = 120 mTorr, flow rate = 19.8 sccm) and argon as a process gas, to create a cross-linked PS layer to the upper part of the PS coating. After argon plasma treatment the wafers were heated in oven at 130°C, which is above the glass transition temperature (T_g = 103°C) of the PS, for 12 hours, for wrinkles to be formed [16].

2.2. Preparation of the hot embossing nickel stamp

A thin Ni layer, having thickness of 35 nm, was sputtered onto of the self-organized PS layers on top of the Si and SST wafers. The sputtered nickel was used as an initiation layer, in order to grow the Ni shims with a thickness of 300 μm in electro-plating equipment (HEGA EFNI 01, Ni-sulfamate). Ni-shim was separated from the Si/PS or SST/PS wafers, cut to a round stamp with a diameter of 60 mm, and cleaned using trichloroethylene and methanol.

2.3. Hot embossing of polycarbonate (PC) and cyclo olefin polymer (COP)

For hot embossing purposes the Ni-stamp was silanized for 10–15 minutes in a glove box in a nitrogen atmosphere using a mixture of HFE-7100 (3M) and trimethylhydroxysilane (ABCR GmbH & Co., 0.2% in HFE-7100), after which the stamp was rinsed for 15 minutes with HFE-7100.

Hot embossing process was conducted using nanoimprinting equipment (Obducat Nanoimprinter Eitre 3) with 3" seating, and the prepared Ni-plates as stamps. Two polymer materials, PC (thickness 0.10 mm) (T_g = 150°C) [31] and COP (thickness 0.15 mm) (T_g = 140°C) [33], were patterned using parameters suitable for each material (Table 1). Hot embossing

Table 1. Hot embossing parameters

	PC	COP
T_1 [°C]	165	150
Pressure [bar]	50	50
Time [s]	120	180
T_2 [°C]	135	135

T_1 is a hot embossing temperature, T_2 is a release temperature

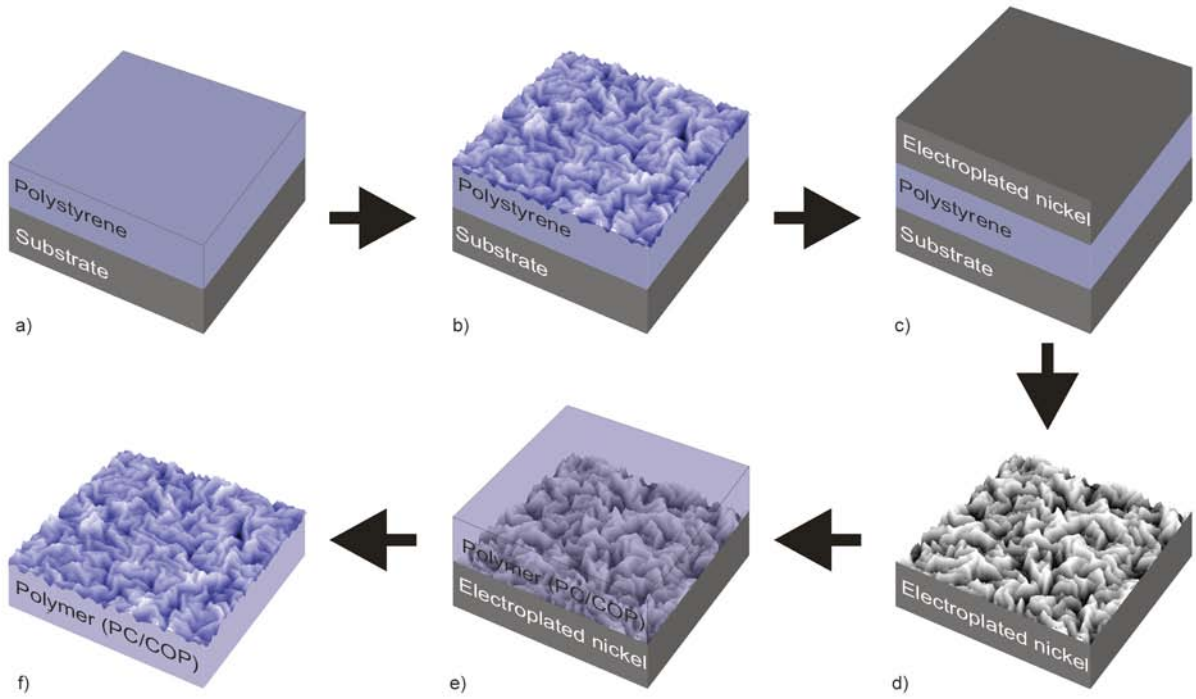

Figure 1. Schematic illustration of the hot embossing process, a) coating the substrate, b) pattern development to the PS, c) electro-plating nickel layer on top of the self-organized PS, d) nickel stamp removal, e) employing the Ni stamp in hot embossing, f) hot embossed PC/COP film

temperature was set above the softening temperature of the used material, whereas the release temperature was below that. The hot embossing process is represented in Figure 1.

2.4. Characterization of the samples

The wrinkled PS layers were observed using non-contact mode of atomic force microscope (AFM, Thermo Microscopes Explorer) with SPMlab 5.01 software. The shapes and the dimensions of the self-organized structures were analyzed using the line analysis, area analysis and peak/valley measurement tools of the software and the minimum height of an individual structure was set to 5 nm.

For filtered power spectral density (FPSD) analysis the numerical data obtained from AFM observation of the surfaces was analyzed by Vision 4.20 program, to create the PSD curves. The PSD curves were further Fourier filtered to obtain the filtered roughness values with selected spatial frequency ranges.

Static contact angles (CA) of the hot embossed and smooth un-patterned reference samples were determined (CAM 200 Optical contact angle meter) for both water and oleic acid, at the ambient temperature. For water, a drop volume of 5 μL was used, whereas in case of oleic acid the volume was set to 1 μL. The duration of each determination was 30 s and the CA was measured from at least five different points. To obtain an average CA of each sample, five last values of each measurement were used in calculation.

Optical properties of the patterned and unpatterned PC and COP films were determined using UV/VIS/NIR spectrometer (Perkin Elmer Lambda 900 UV/

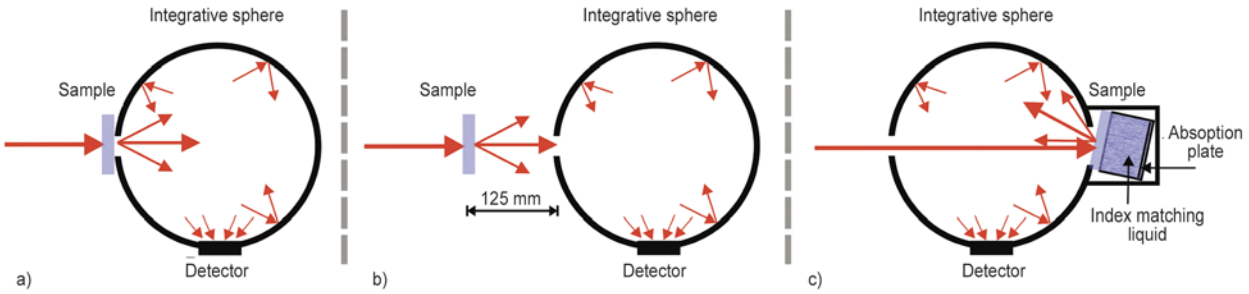

Figure 2. Schematic illustration of the experimental configurations for a) transmittance, b) scattering and c) reflectance determination

VIS/NIR) with 150 mm integrative sphere accessory unit. The wavelength range from 300 to 1000 nm was scanned with 1 nm step resolution. In reflectance measurements index matching liquid (Cargille Series: A, n =1.48000) and an absorption plate were used behind the sample film to prevent the backside reflection. In order to examine the scattering property of the samples, the transmittance determinations were carried out first by setting the sample in a holder at the opening of the integrative sphere and secondly by using a movable sample holder, which was placed 12.5 cm from the integrative sphere opening. The measurements were carried out at ambient temperature (25°C), in air. The schematic illustration of the all experimental setups is presented in Figure 2.

3. Results and discussion

3.1. Fabrication of the structured surfaces

In order to develop a patterned PS layer on top of the polystyrene coated Si and SST wafers, a stiff superstrate was created by cross-linking the uppermost layer of the PS coating by employing a plasma treatment with a mild conditions [16] and argon as a process gas, after which the pattern formation was obtained by annealing. Use of the SST wafer enabled a study of the influence of the substrate with a characteristic surface structure, on the self-organized pattern formation and the shape and dimensions of the patterns of polystyrene.

Patterns of the PS layer obtained employing Si substrate, possessed a shape of wrinkles (Figure 3a). The highest wrinkles were about 200 nm, whereas the average height value, determined for the whole scanned area (10×10 μm), was about 100 nm (Figure 3a). The average period (peak-to-peak) was determined to be about 240 nm. The surface of the Ni-stamp, prepared on top of the wrinkled PS layer is a negative of the original surface pattern (Figure 3c). The surface of an uncoated SST wafer composed of characteristic island-like structures having height from 300 to 500 nm, determined by AFM [15]. The self-organized patterns of PS film formed on the SST substrate also possessed a shape of wrinkles (Figure 3b). The average wrinkle height was 210 nm and the highest wrinkles were 390 nm. The average period (peak-to-peak) was determined to 400 nm.

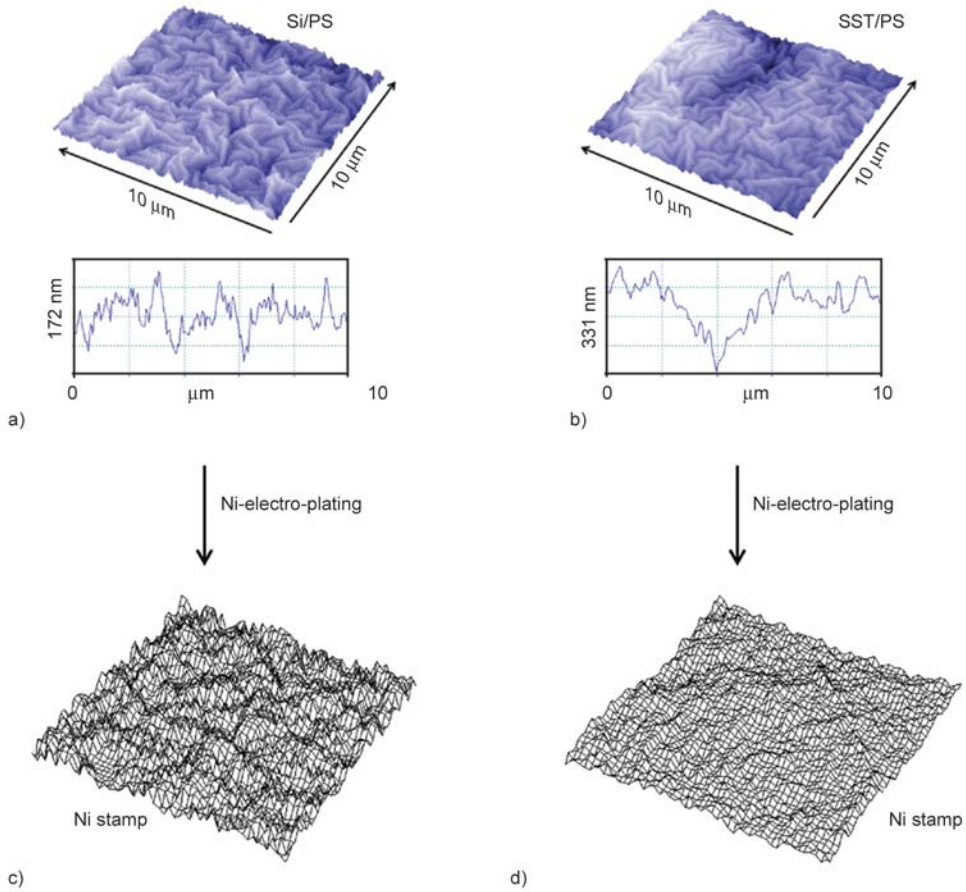

Figure 3. AFM images (10 μm×10 μm) and topography graphs (10 μm) of self-organized PS patterns formed on (a) Si and (b) SST wafer and transferred to Ni-stamp as negation (c) and (d)

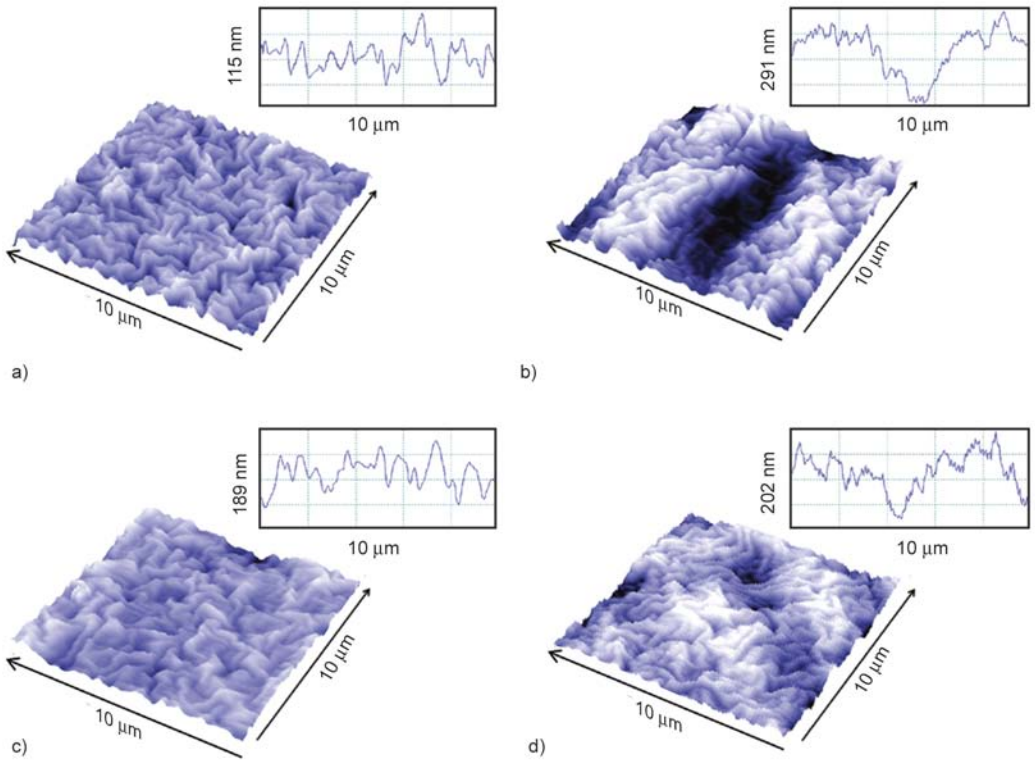

Figure 4. AFM images (10 µm×10 µm) and topography graphs (10 µm) of the hot embossed PC and COP films; (a) PC/Si, (c) COP/Si, (b) PC/SST, (d) COP/SST

Dimensions of the surface patterns were determined employing area analysis tool of the AFM software from the whole scanned area (10×10 µm). Figure 3d shows the wrinkles, transferred from the SST/PS wafer to the Ni plate.

Self-organized structures formed on PS coated Si and SST wafers, were successfully replicated onto PC and COP films with thicknesses of 0.10 and 0.15 mm, respectively (Figure 4). Dimensions of the wrinkles on the hot embossed polymers were determined by AFM. The average height value of the replicated wrinkles employing the Si substrate was about 100 nm (Table 2) and the largest heights 200 nm. Copied structures on the patterned polymers (PC, COP) show some characteristic shapes of the SST wafer (Figure 4 b and 4d) island-like features.

Table 2. Average dimensions of the self-organized patterns on original and hot embossed surfaces

Sample	Average height [nm]	Average period [µm]
Si/PS	100	0.24
$PC_{hot\ embossed,\ Si}$	90	0.77
$COP_{hot\ embossed,\ Si}$	90	0.65
SST/PS	210	0.40
$PC_{hot\ embossed,\ SST}$	130	0.28
$COP_{hot\ embossed,\ SST}$	120	0.23

3.2. Replication quality

The replication fidelity of the self-organized wrinkles on the PC and COP films was evaluated employing power spectral density analysis with filtered roughness values (FPSD) [34, 35]. This analysis gives detailed information mainly of the structure periodicities and is based on the numerical data obtained from the AFM determinations of the original wrinkled surfaces and the replicated PC and COP films.

In the case of self-organized structures formed on Si substrate (Figure 5a, Si/PS), the spectral density curve and the filtering results of the corresponding roughness show a large amount of the surface roughness to be centered in the filtering ranges 100–500 nm and 1–10 µm, whereas area 500–1000 nm contains less spectral density. The AFM observation of the wrinkled Si/PS surface patterns (Figure 3a) showed the structure consisting of both smaller and larger wrinkles with an average period value of 240 nm. Therefore, the results obtained by FPSD are in line with the findings of AFM analysis.

Comparison between the filtered roughness values of hot embossed polymer films (PC and COP) and the original surface (Si/PS) shows a quite similar trend for all samples; the filtering ranges 100–500 nm

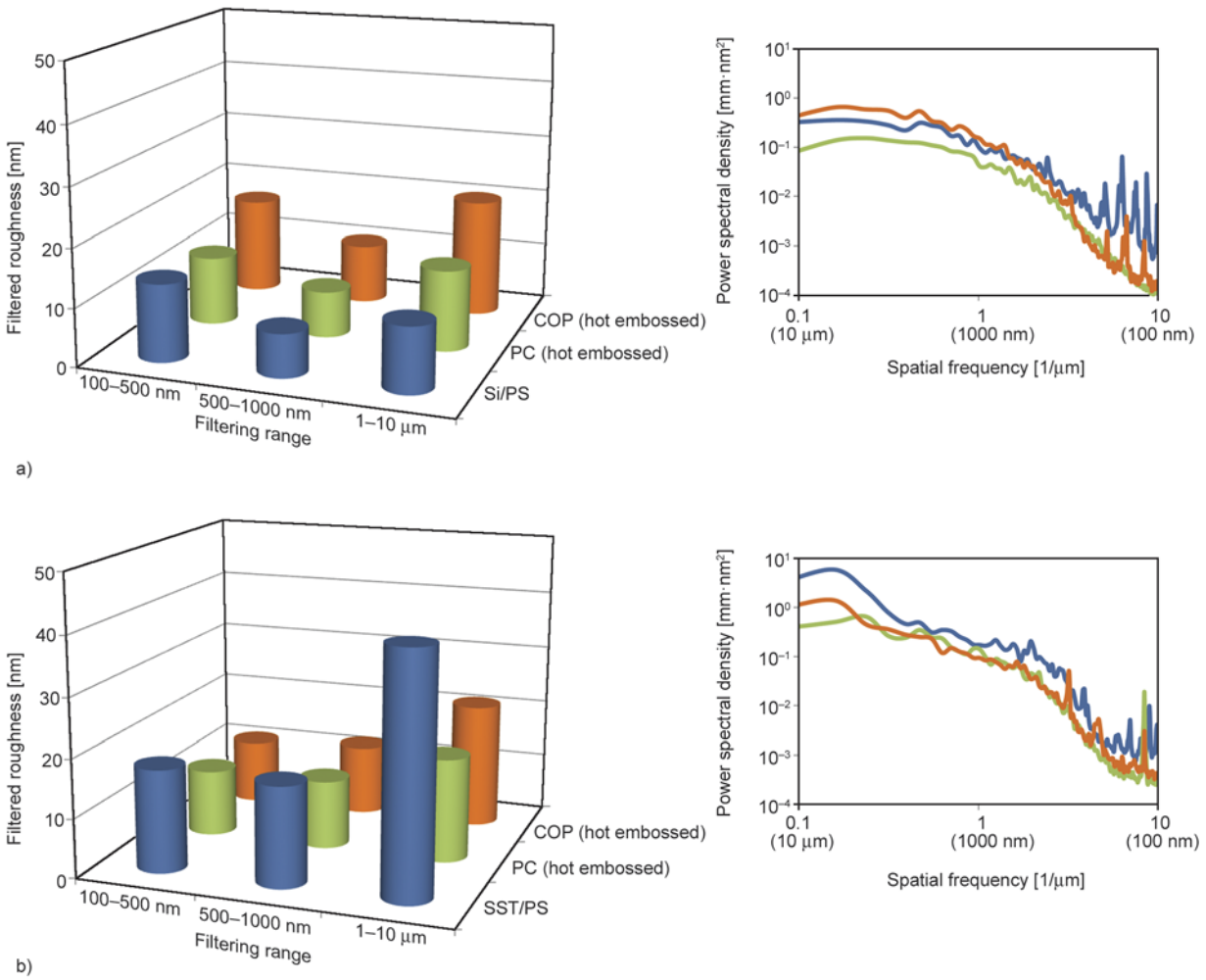

Figure 5. PSD analysis results of wrinkled surfaces formed on (a) Si substrate and (b) SST substrate, and replicated to PC and COP films by hot embossing

and 1–10 µm contain more roughness than the range 500–1000 nm (Figure 5a). The original wrinkled surface contains a lot of small peaks, which seem to have vanished due to replication process. This influences the values of average wrinkle periods. Even though, lacking the smallest wrinkles, the patterning of $PC_{hot\ embossed,\ Si}$ and $COP_{hot\ embossed,\ Si}$, still include quite a large amount of roughness with the periodicity located in the filtering range 100–500 nm.

According to the FPSD analysis of the original SST substrate with the self-organized PS coating on top of it, the highest proportion of surface roughness is concentrated in the filtering range 1–10 µm, but also located in the filtering ranges 100–500 nm and 500–1000 nm are present (Figure 5b, SST/PS). By AFM observation the average period of these structures was determined to about 400 nm. A large proportion of the roughness in the range 1–10 µm in the FPSD analysis is probably due to characteristic island-like surface structure of the uncoated SST wafer. The roughness distributions of the hot embossed PC and COP films (Figure 5b) resemble the FPSD result of the original SST/PS. AFM analysis of the $PC_{hot\ embossed,\ SST}$ and $COP_{hot\ embossed,\ SST}$ gave the average period values of 0.28 and 0.23 µm (Table 2), respectively.

3.3. Surface and optical properties

Static contact angles (CA) of water and oleic acid were determined for both the unpatterned reference and hot embossed polymer samples. In case of PC the water CAs of patterned and unpatterned samples were almost the same, the values being 83–87°. In case of oleic acid the contact angles of the PC samples increased from 6 to 14° ($PC_{hot\ embossed,\ Si}$) and to 12° ($PC_{hot\ embossed,\ SST}$) due to the surface patterning. The CA values of COP samples showed the patterning having no significant influence on water or oleic acid CAs of the material; the CA of water was

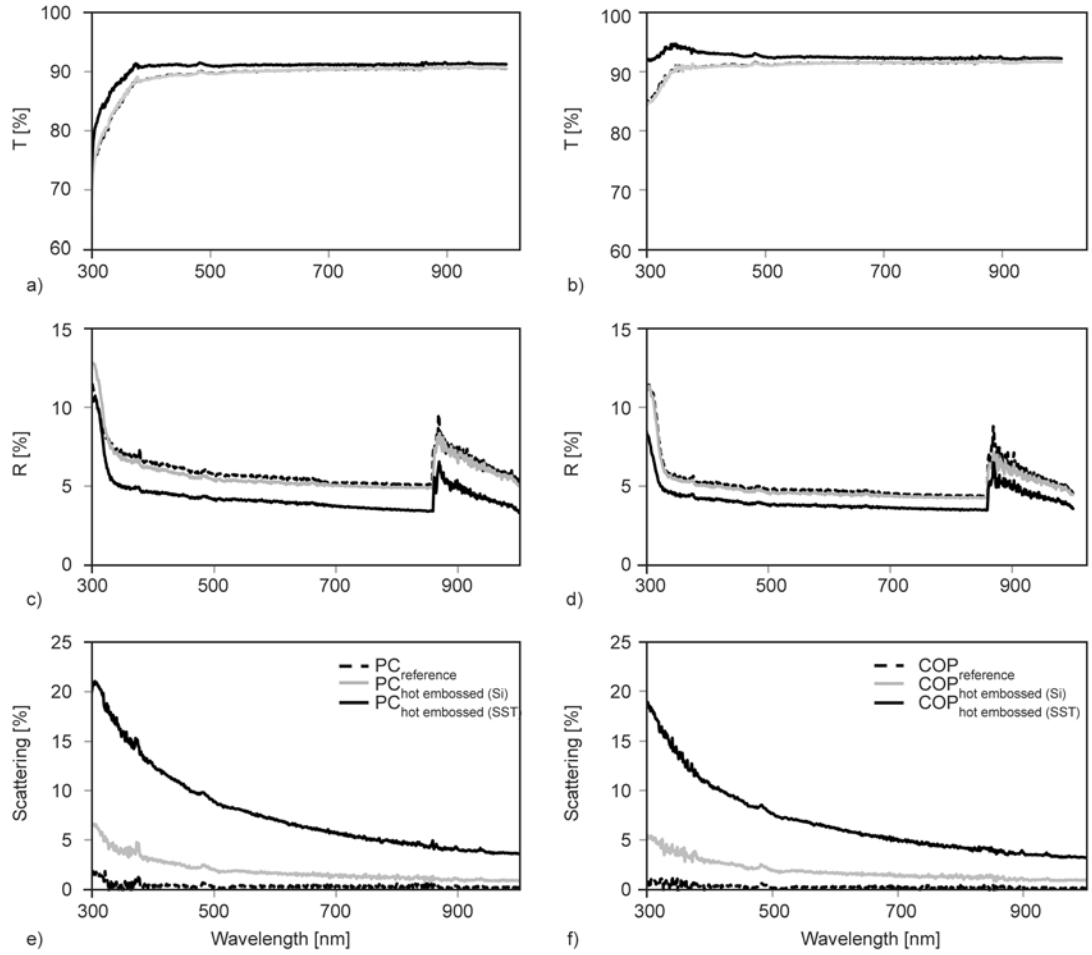

Figure 6. Transmittances, reflectances and scatterings of the reference and hot embossed PC (a, c, e) and COP (b, d, f) films

lowered 2–3° from the value of the smooth reference (101°) and the CA of oleic acid remained the same being 4–5°.

Influence of the hot embossed patterning on the transparency, reflectivity and scattering properties of the PC and COP films, was observed by determining transmittance and reflectance values of the reference and patterned samples using the UV/VIS/NIR spectrometer in the wavelength range of 300–1000 nm. In the case of reflectance determinations, scattering was ignored. Values of the determined properties at the wavelengths 450, 530 and 610 nm, corresponding the prime colors of blue, green and red [36], respectively, are collected in Table 3.

Comparison between the transmittance values of the smooth PC and COP reference samples and corresponding hot embossed samples reveals that the wrinkle structures originally formed on SST substrate slightly increase the transmittance of the polymer films (Figure 6), whereas the wrinkles developed on silicon wafer have no effect on this property. Reflectances of the patterned and the reference samples were determined employing index matching liquid and absorption plate behind the sample to

Table 3. UV/VIS results of the unpatterned reference and hot embossed PC and COP samples at the wavelengths 450, 530 and 610 nm

Sample	Transmittance [%]			Reflectance [%]			Scattering [%]		
	450 nm	530 nm	610 nm	450 nm	530 nm	610 nm	450 nm	530 nm	610 nm
$PC_{reference}$	89.5	89.9	90.1	6.1	5.7	5.6	0.3	0.3	0.3
$PC_{hot\ embossed,\ Si}$	89.4	89.9	90.1	5.8	5.4	5.3	2.7	1.9	1.6
$PC_{hot\ embossed,\ SST}$	91.1	91.0	91.1	4.4	4.2	4.0	11.2	8.3	6.9
$COP_{reference}$	91.1	91.3	91.5	5.0	4.8	4.8	0.3	0.2	0.2
$COP_{hot\ embossed,\ Si}$	91.0	91.2	91.4	4.8	4.6	4.5	2.4	1.9	1.6
$COP_{hot\ embossed,\ SST}$	92.8	92.5	92.4	4.0	3.8	3.8	8.9	7.2	6.0

prevent the backside reflection. For PC and COP materials the reflectance values of the unpatterned reference and the corresponding hot embossed samples patterned with the structures formed on Si substrate, were almost the same (Table 3). In case of $PC_{hot\ embossed\ (SST)}$ patterned with structures formed on SST substrate, the reflectance value (610 nm) was 28% lower compared with the smooth PC reference sample, being 4.0%. By structuring the COP film with patterns formed on SST wafer ($COP_{hot\ embossed\ (SST)}$) the reflectivity of the material was lowered 20% and the reflectance value of 3.8% (610 nm) was obtained (Table 3). The irregularity at the wavelength of 860 nm (Figure 6c and 6d) is due to the detector change.

Analyzing the PC samples revealed the scattering property been increased due to structuring the polymer film by hot embossing (Figure 6). For $PC_{reference}$ the scattering was 0.3% (610 nm) and the value of $PC_{hot\ embossed\ (Si)}$ 1.6% (610 nm). Applying the patterns formed on SST substrate onto the PC films ($PC_{hot\ embossed\ (SST)}$) resulted in material possessing 6.9% scattering (Table 3). For COP films the corresponding values were $COP_{reference}$ 0.2%, $COP_{hot\ embossed\ (Si)}$ 1.6% and $COP_{hot\ embossed\ (SST)}$ 6.0 % (Table 3). The influence of the structures, formed on Si and SST wafers and replicated by hot embossing into PC and COP films, on the scattering property of these materials is notable.

For patterned PC/COP films with a wrinkled surface structure, certain material and structural requirements must be fulfilled in order to obtain structured polymer films possessing anti-reflective (AR) properties. In the case of transparent PC and COP materials with refractive indices close to 1.5 [37, 38], Fresnel reflection occurs at the air/polymer interface [39], due to the large difference in index values of air and polymer [40]. By patterning the surface of the polymer film with sub-wavelength relief structures with an optimized period, depth and filling factor, the refractive index of air is gradually increased to the value of the employed polymer material, leading to the reduced reflection from the film surface [25, 41]. Therefore, in the case of the hot embossed and wrinkle structured PC and COP films, significantly lowered reflectance values over the observed wavelength area can be achieved, when the shape and dimensions of the replicated patterns meet the requirements for AR coating. In contrast to the patterned surfaces with precise structuring and tailored AR properties, the spontaneous self-organization yields patterns with random orientation and topology, and resembling the stochastic surface structure presented by Gombert *et al*. [42]. In order to obtain enhanced optical properties, like anti-reflectivity, the composition of the system undergoing self-organization, as well as the initiation method, could be tailored to produce the desired surface reliefs.

4. Conclusions

Self-organized structure formation on polymer thin films is a phenomenon, which is quite vastly studied, but rather seldom utilized in applications. In this research the replication of a characteristic and unique surface structure firstly into a nickel stamp and further into selected polymer films, is demonstrated. The results show that the obtained wrinkle structures have a slight influence on the wetting of the PC and COP films. The transmittance and reflectance determinations of the PC and COP samples reveal the scattering been somewhat increased and the reflectivity of the materials been lowered, due to hot embossed patterning. Optimization of the shapes and dimensions of the self-organized structures gives a tool for a further improvement of, e.g., wettability and optical properties of different materials. The self-organized pattern formation enables fabrication of patterns with a variety of configurations and possessing a size-scale from nano- to micrometer. The present method, carried out using hot embossing process, is cost-effective and easily transferred also into a mass production.

Acknowledgements

Great acknowledgements to PhD Hemmo Tuovinen for help with the UV/VIS determinations. Laboratory engineer Tommi Itkonen is thanked for preparing the Ni-plates. Financial support from the European Union/European Regional Development Fund (ERDF, PRI project) is gratefully acknowledged.

References

[1] Li B., Cao Y-P., Feng X-Q., Gao H.: Mechanics of morphological instabilities and surface wrinkling in soft materials: A reviw. Soft Matter, **8**, 5728–5745 (2012). DOI: 10.1039/C2SM00011C

[2] Niu K., Talreja R.: Modeling of wrinkling in sandwich panels under compression. Journal of Engineering Mechanics, **125**, 875–883 (1999). DOI: 10.1061/(ASCE)0733-9399(1999)125:8(875)

[3] Chung J. Y., Nolte A. J., Stafford C. M.: Surface wrinkling: A versatile platform for measuring thin-film properties. Advanced Materials, **23**, 349–368 (2011). DOI: 10.1002/adma.201001759
[4] Chan E. P., Page K. A., Im S. H., Patton D. L., Huang R., Stafford C. M.: Viscoelastic properties of confined polymer films measured via thermal wrinkling. Soft Matter, **5**, 4638–4641 (2009). DOI: 10.1039/B916207K
[5] Genzer J., Groenewold J.: Soft matter with hard skin: From skin wrinkles to templating and material characterization. Soft Matter, **2**, 310–323 (2006). DOI: 10.1039/B516741H
[6] Léotoing L., Drapier S., Vautrin A.: First applications of a novel unified model for global and local buckling of sandwich columns. European Journal of Mechanics – A/Solids, **21**, 683–701 (2002). DOI: 10.1016/S0997-7538(02)01229-9
[7] Koissin V., Shipsha A., Skvortsov C.: Wrinkling in sandwich panels – An analytical approach. Journal of Sandwich Structures and Materials, **13**, 705–730 (2011). DOI: 10.1177/1099636211419129
[8] Steigmann D. J.: Tension-field theory. Proceedings of the Royal Society A, **429**, 141–173 (1990). DOI: 10.1098/rspa.1990.0055
[9] Cao Y., Hutchinson J. W.: From wrinkles to creases in elastomers: The instability and imperfection-sensitivity of wrinkling. Proceedings of the Royal Society A, **468**, 94–115 (2012). DOI: 10.1098/rspa.2011.0384
[10] Sun J-Y., Xia S., Moon M-W., Oh K-H., Kim K-S.: Folding wrinkles of a thin stiff layer on a soft substrate. Proceedings of the Royal Society A, **468**, 932–953 (2012). DOI: 10.1098/rspa.2011.0567
[11] Lei H., Payne J. A., McCormick A. V., Francis L. F., Gerberich W. W., Scriven L. E.: Stress development in drying coatings. Journal of Applied Polymer Science, **81**, 1000–1013 (2001). DOI: 10.1002/app.1522
[12] Chen C-M., Yang S.: Wrinkling instabilities in polymer films and their applications. Polymer International, **61**, 1041–1047 (2012). DOI: 10.1002/pi.4223
[13] Kolaric B., Desprez S., Brau F., Damman P.: Design of curved photonic crystal using swelling induced instabilities. Journal of Materials Chemistry, **22**, 16205–16208 (2012). DOI: 10.1039/c2jm32997b
[14] Chen Y-C., Crosby A. J.: Wrinkling of inhomogeneously strained thin polymer films. Soft Matter, **9**, 43–47 (2013). DOI: 10.1039/C2SM26822A
[15] Stenberg H., Stenberg P., Suvanto M., Pakkanen T. T.: Self-organized pattern formation on silicon, stainless steel and zinc coated steel substrates. Progress in Organic Coatings, **77**, 131–135 (2014). DOI: 10.1016/j.porgcoat.2013.08.013
[16] Stenberg H., Maaranen J., Suvanto M., Pakkanen T. T.: Solvent-assisted and thermal wrinklings of argon plasma treated polystyrene coatings on silicon substrate. Surface and Coatings Technology, **238**, 133–138 (2014). DOI: 10.1016/j.surfcoat.2013.10.060
[17] Katzenstein J. M., Janes D. W., Cushen J. D., Hira N. B., McGuffin D. L., Prisco N. A., Ellison C. J.: Patterning by photochemically directing the marangoni effect. ACS Macro Letters, **1**, 1150–1154 (2012). DOI: 10.1021/mz300400p
[18] Bonaccurso E., Graf K.: Nanostructuring effect of plasma and solvent treatment on polystyrene. Langmuir, **20**, 11183–11190 (2004). DOI: 10.1021/la036441o
[19] Schweikart A., Fery A.: Controlled wrinkling as a novel method for the fabrication of patterned surfaces. Microchimica Acta, **165**, 249–263 (2009). DOI: 10.1007/s00604-009-0153-3
[20] Torres J. M., Stafford C. M., Uhrig D., Vogt B. D.: Impact of chain architecture (branching) on the thermal and mechanical behavior of polystyrene thin films. Journal of Polymer Science Part B: Polymer Physics, **50**, 370–377 (2012). DOI: 10.1002/polb.23014
[21] Chung J. Y., Youngblood J. P., Stafford C. M.: Anisotropic wetting on tunable micro-wrinkled surfaces. Soft Matter, **3**, 1163–1169 (2007). DOI: 10.1039/B705112C
[22] Lin P-C., Yang S.: Mechanically switchable wetting on wrinkled elastomers with dual-scale roughness. Soft Matter, **5**, 1011–1018 (2009). DOI: 10.1039/B814145B
[23] Celia E., Darmanin T., de Givenchy E. T., Amigoni S., Guittard F.: Recent advances in designing superhydrophobic surfaces. Journal of Colloid and Interface Science, **402**, 1–18 (2013). DOI: 10.1016/j.jcis.2013.03.041
[24] Becker H., Heim U.: Hot embossing as a method for the fabrication of polymer high aspect ratio structures. Sensors and Actuators A: Physical, **83**, 130–135 (2000). DOI: 10.1016/S0924-4247(00)00296-X
[25] David C., Häberling P., Schnieper M., Söchtig J., Zschokke C.: Nano-structured anti-reflective surfaces replicated by hot embossing. Microelectronic Engineering, **61–62**, 435–440 (2002). DOI: 10.1016/S0167-9317(02)00425-2
[26] Lee G-B., Chen S-H., Huang G-R., Sung W-C., Lin Y-H.: Microfabricated plastic chips by hot embossing methods and their applications for DNA separation and detection. Sensors and Actuators B: Chemical, **75**, 142–148 (2001). DOI: 10.1016/S0925-4005(00)00745-0
[27] Gale M. T.: Replication techniques for diffractive optical elements. Microelectronic Engineering, **34**, 321–339 (1997). DOI: 10.1016/S0167-9317(97)00189-5

[28] Stuart C., Chen Y.: Roll in and roll out: A path to high-throughput nanoimprint lithography. ACS Nano, **3**, 2062–2064 (2009).
DOI: 10.1021/nn9008356

[29] Gale M. T., Gimkiewicz C., Obi S., Schnieper M., Söchtig J., Thiele H., Westenhöfer S.: Replication technology for optical microsystems. Optics and Lasers in Engineering, **43**, 373–386 (2005).
DOI: 10.1016/j.optlaseng.2004.02.007

[30] Chou S. Y., Krauss P. R., Renstrom P. J.: Imprint lithography with 25-nanometer resolution. Science, **272**, 85–87 (1996).
DOI: 10.1126/science.272.5258.85

[31] Schweikart A., Zimin D., Handge U. A., Bennemann M. Altstädt V., Fery A., Koch K.: Fabrication of artificial petal sculptures by replication of sub-micron surface wrinkles. Macromolecular Chemistry and Physics, **211**, 259–264 (2010).
DOI: 10.1002/macp.200900543

[32] Callister W. D., Rethcwisch D. G.: Materials science and engineering. Wiley, Hoboken (2011).

[33] Kohara T.: Development of new cyclic olefin polymers for optical uses. Macromolecular Symposia, **101**, 571–579 (1996).
DOI: 10.1002/masy.19961010163

[34] Vepsäläinen L., Pääkkönen P., Suvanto M., Pakkanen T. A.: Frequency analysis of micropillar structured surfaces: A characterization and design tool for surface texturing. Applied Surface Science, **263**, 523–531 (2012).
DOI: 10.1016/j.apsusc.2012.09.098

[35] Vepsäläinen L., Stenberg P., Pääkkönen P., Kuittinen M., Suvanto M., Pakkanen T. A.: Roughness analysis for textured surfaces over several orders of magnitudes. Applied Surface Science, **284**, 222–228 (2013).
DOI: 10.1016/j.apsusc.2013.07.085

[36] Brill M. H.: A theorem on prime-color wavelengths. Color Research and Applications, **21**, 239–240 (1996).
DOI: 10.1002/(SICI)1520-6378(199606)21:3<239::AID-COL6>3.0.CO;2-T

[37] Kasarova S. N., Sultanova N. G., Ivanov C. D., Nikolov I. D.: Analysis of the dispersion of optical plastic materials. Optical Materials, **29**, 1481–1490 (2007).
DOI: 10.1016/j.optmat.2006.07.010

[38] Khanarian G., Celanese H.: Optical properties of cyclic olefin copolymers. Optical Engineering, **40**, 1024–1029 (2001).
DOI: 10.1117/1.1369411

[39] Kikuta H., Toyota H., Yu W.: Optical elements with subwavelength structured surfaces. Optical Review, **10**, 63–73 (2003).
DOI: 10.1007/s10043-003-0063-2

[40] Chattopadhyay S., Huang Y. F., Jen Y. J., Ganguly A., Chen K. H., Chen L. C.: Anti-reflecting and photonic nanostructurfes. Materials Science and Engineering R: Reports, **69**, 1–35 (2010).
DOI: 10.1016/j.mser.2010.04.001

[41] Päivänranta B., Saastamoinen T., Kuittinen M.: A wide-angle antireflection surface for the visible spectrum. Nanotechnology, **20**, 375301/1–375301/7 (2009).
DOI: 10.1088/0957-4484/20/37/375301

[42] Gombert A., Glaubitt W., Rose K., Dreibholz J., Bläsi B., Heinzel A., Sporn D., Döll W., Wittwer V.: Subwavelength-structured antireflective surfaces on glass. Thin Solid Films, **351**, 73–78 (1999).
DOI: 10.1016/S0040-6090(98)01780-5

eXPRESS Polymer Letters Vol.9, No.2 (2015) 105–118
Available online at www.expresspolymlett.com
DOI: 10.3144/expresspolymlett.2015.12

A facile route for controlled alignment of carbon nanotube-reinforced, electrospun nanofibers using slotted collector plates

*G. R. Rakesh, G. S. Ranjit, K. K. Karthikeyan, P. Radhakrishnan, P. Biji**

Nanosensor Laboratory, PSG Institute of Advanced Studies, Coimbatore-641004, India

Received 12 April 2014; accepted in revised form 10 September 2014

Abstract. A facile route for controlled alignment of electrospun multiwalled carbon nanotube (MWCNT)-reinforced Polyvinyl Alcohol (PVA) nanofibers using slotted collector geometries has been realized. The process is based on analytical predictions using electrostatic field analysis for envisaging the extent of alignment of the electrospun fibers on varied collector geometries. Both the experimental and theoretical studies clearly indicate that the introduction of an insulating region into a conductive collector significantly influences the electrostatic forces acting on a charged fiber. Among various collector geometries, rectangular slotted collectors with circular ends showed good fiber alignment over a large collecting area. The electrospun fibers produced by this process were characterized by Atomic Force Microscopy (AFM), High Resolution Transmission Electron Microscopy (HRTEM), Scanning Electron Microscopy (SEM) and Optical Microscopy. Effects of electrospinning time and slot widths on the fiber alignment have been analyzed. PVA-MWCNT nanofibers were found to be conducting in nature owing to the presence of reinforced MWCNTs in PVA matrix. The method can enable the direct integration of aligned nanofibers with controllable configurations, and significantly simplify the production of nanofibers-based devices.

Keywords: *nanocomposites, electrospinning, electrostatic field analysis, carbon nanotubes, aligned nanofibers*

1. Introduction

Nanowires with tailored physical properties have been used as key components in flexible electronics, electronic logic gates, renewable energy technologies, and chemical/biological sensor applications [1]. Direct integration of nanowires in devices remains as a major challenge, as it is difficult to reproducibly locate them in specific positions and orientations [2]. Development of cost-effective and reliable techniques for controlled integration of nanowires onto devices is very much essential for the commercialization of nanotechnology related products [3, 4]. Among various nanofabrication techniques, electrospinning is a highly versatile and cost-effective process in which, solid micro and nanofibers are produced from a polymeric fluid stream (solution or melt) delivered through a nozzle [5, 6]. Several innovative approaches have been introduced in this field for developing nanofibers with varied constitution and structure for diverse applications. There have been much research and progress in the development of various designs and modification to the electrospinning process over the last century. Special multi-spinneret designs, such as, coaxial, bicomponent, gas-jacketed electrospinning have made a breakthrough in the electrospinning process by creating hybrid electrospun nanofibers [7–11].

One of the major problems that influence the commercial viability of nanofibers membranes is the

*Corresponding author, e-mail: bijuja123@yahoo.co.in

lack of structural integrity of ultrathin electrospun membranes. The full potential of electrospun nanofibers can be utilized for commercial applications, only when they are assembled as well-ordered structures with the desired mechanical stability and structural integrity. Hierarchically organized nanofibers have great potential to solve this problem, as they allow interfacing nanofibers with various structural surfaces [12, 13]. So far, the challenge of controlling the spatial orientation of electrospun fibers has been met with partial success [7, 14]. Both mechanical and electrostatic means have been explored to improve the alignment of electrospun nanofibers [15–17]. Many reports show that the as-spun fibers could be aligned more or less parallel to each other when a rotating drum at high speed is used as the collector [18]. A wheel-like bobbin was used as the collector to position and align individual polymer nanofibers and was demonstrated by Zussman and co-workers. But, since the edge of such a bobbin had to be relatively sharp, this technique was not feasible for the formation of well-aligned nanofibers over large areas [19]. This problem has been resolved partially by parallel plate collectors which consist of two pieces of electrically conductive substrates separated by a gap to produce uniaxially aligned arrays of fibers [20]. This method was further extended by a simple method by Katta *et al*. [21] for spinning sheets with 1 cm wide strips of aligned nanofibers using copper wires spaced evenly in the form of a circular drum as a collector of the electrospun nanofibers. Another approach was developed by Chvojka *et al*. [22] who produced PVA nanoyarns using a special saw-like collector, by twisting electrospun PVA nanofibers and introduced a simple analysis of the field strength that causes the prevailing unidirectional fiber deposition between neighbouring lamellae of a special saw-like collector. Few groups have also worked on producing aligned fibers by using collector plates of special designs [23–25]. But, it is difficult to understand how the electric field behaves in each of these types of collector designs. Although numerous reports exist about the preparation and application of electrospun polymer nanofibers and composites, very small attention have been paid to how to manipulate the electric field for producing high quality or aligned nanofibers.

Carbon nanotubes (CNTs) have high Young's modulus, low density, and excellent electrical and thermal properties, which make them ideal fillers for polymer nanocomposites [26, 27]. Production of carbon nanotube-polymer nanocomposite materials is one of the key factors controlling the mechanical properties in composite and hybrid systems. Carbon nanotube-polymer nanocomposites in the form of nano/microfibers have immense applications, such as, nanofilters of scalable pore size and structural components for microdevices. Electrospun CNT/polymer nanofibers have been demonstrated to be attractive for a large variety of potential applications, such as, in optoelectronic and sensor devices. Other potential applications of electrospun CNTs/polymer nanofibers include tissue engineering scaffolds, composite reinforcement, drug carriers for controlled release and energy storage [28, 29]. To realize their commercial applications, considerable work is still required. This includes a thorough understanding of the structure–property relationship for various electrospun polymer nanofibers, the effective incorporation of carbon nanotubes into polymer fibers with a high loading content, and large scale production of composite nanofibers of consistent and high quality, but at a low cost. Few reports prove that electrospinning a polymer solution containing well-dispersed carbon nanotubes lead to nanocomposite fibers. During fast fiber-drawing process, these fibers embed carbon nanotubes, oriented parallel to the nanofiber axis due to large shear forces [30, 31]. A modified rotating disk collector including two separate parallel aluminium plates with sharp edges was used by Huang *et al*. [32] to fabricate SWNTs/polyvinylidene difluoride (PVDF) composite nanofibers. They observed that the interfacial interaction between SWNTs and PVDF and the application of extensional forces have a strong synergistic effect on crystalline structures of PVDF inducing oriented crystallites at only 0.01 wt% of nanotubes. Ge and coworkers developed oriented composite nanofiber sheets made from surface-oxidized multiwalled carbon nanotubes (MWCNTs) and polyacrylonitrile (PAN) using electrospinning [29]. Recently, Chen *et al*. [33] demonstrated that surface-functionalized MWNTs were homogeneously dispersed and highly aligned along the polyimide nanofiber axis, whereas most of the pristine MWNTs form aggregates or bundles and even protruded out of the electrospun nanofibers. Zhang *et al*. [34] produced uniaxially aligned electrospun nanofibers of PAN and Triton X-100 grafted MWNTs using a collector consisting

of two pieces of electrodes as well as a slowly rotating drum with multi-electrodes. Yee *et al*. [35] modified the design of a disk by using two separate parallel aluminium electrodes attached to a rotating disk to collect the well-aligned MWCNT/PVDF nanofibers, where both the electric field and mechanical force contributed to nanofiber alignment.

Though there are various special dynamic collectors reported, such as, rotating drums, wire drums, discs, rings etc., most of them require an external power to rotate at high rpm and it is difficult to deposit the aligned fibers onto devices directly [7]. Static collectors includes parallel strips, micromachined patterns etc., where aligned fiber formation is possible, but, mechanical stability for the aligned fibers is very poor, especially while integrating these fibers onto devices [36, 37]. Hence, there is a need for developing low cost, efficient techniques to fabricate aligned nanofibers. In this investigation, we report a simple and novel route to predict the fiber alignment to produce uniaxially aligned MWCNT-reinforced PVA nanofibers on various collector geometries. The fundamental concept adopted for this investigation is based on engineering the electrostatic field using slotted collectors during electrospinning. Our main emphasis here is to alter the nature of electrostatic field on collector plate by creating a repulsive field of various magnitude and directions by using collector plates having varied geometrical slots to produce aligned electrospun nanofibers. The collector geometries used in this investigation are having in-built insulating air gaps which induce fiber alignment by varying the electrostatic field lines. This method can provide proper mechanical stability to the fibers formed compared to the parallel plate collectors. It is also possible to use multiple slots made on single collector to produce aligned nanofibers. This method can be further used for direct integration of electrospun nanofibers having any composition to microdevices, especially for sensor applications. Current process can also be further extended in combination with near field electrospinning techniques for patterning various designs of nanofibers which is having immense applications in micro/nanoelectronics.

2. Experimental details

2.1. Materials and methods

Polyvinyl alcohol, (PVA, 99%, M_W = 140 000, HiMedia) was used without further purification to prepare feed solution for the electrospinning. Commercially available multiwalled carbon nanotubes (MWCNT, >90 %, diameter: 20–30 nm, length: 0.5–2 μm, Quantum Materials Corp., India) produced by Chemical Vapour Deposition were used for the composite nanofiber formation. Ultrapure water (Millipore Academic, Resistivity, 18.2 MΩ·cm) was used for the preparation of feed solution. Optical Microscopic images were obtained using Polarized Optical Microscope (Leica, UK). Atomic Force Microscopic (AFM) images were acquired using Multimode Scanning Probe Microscope (NTMDT-NTEGRA, Russia) for the electrospun fibers transferred onto *p*-type Si(100) substrates. Transmission Electron Microscopic (TEM, JEOL 2010, Japan) analysis was carried out for the electrospun fibers transferred onto carbon coated copper films. Field Emission Scanning Electron Microscope (ZEISS SUPRA 55, Germany) was used to study the alignment and morphology of the nanofibers. Conductivity studies were carried out using a high-current source meter (Model: 2420, Keithley, USA).

Electrostatic field analysis was performed using COMSOL Multiphysics software. The CAD model for the collector plates were created in SOLIDWORKS software and imported to COMSOL Multiphysics. Aluminium plates (thickness: 3 mm) were used to fabricate collector geometries by introducing slots of required geometry and dimensions. Different geometric configurations were created using wire electric discharge machining (EDM). EDM drilling was done prior to wire EDM process to provide starting holes for the wires. After machining, the plates were cut into required dimensions using shear cutter and cleaned ultrasonically using ethanol and ultrapure water. The cleaned, slotted collector plates were used for the electrospinning process without further surface treatments.

2.2. PVA-MWCNT feed solution preparation

The carbon nanotubes were functionalized using acid treatment as per previous reports to enhance the dispersion of carbon nanotubes in the polymer fibers [38]. Carboxylic and hydroxyl groups were produced at the peripheral walls of carbon nanotubes by this process and thereby achieved a good dispersion producing unbundled CNTs. Concentration of PVA in ultrapure water was kept constant as 10 wt% throughout the experiments after optimizing parameters, such as, voltage, needle-to-collector

distance, flow rate and concentration. PVA-MWCNT feed solution was prepared by mixing 1 wt% MWCNT with 10 wt% PVA solution for electrospinning. Before electrospinning, the mixture was stirred and ultrasonicated (power: 500 watts, frequency: 20 kHz) for 30 minutes to avoid granules present in the solution and to obtain uniform dispersion of CNTs.

2.3. Nanofiber production using electrospinning process

The electrospinning of PVA-MWCNT was carried out using an in-house electrospinning unit fabricated in our laboratory. The experimental set-up was enclosed in Pyrex glass chamber to ensure operator safety while the process is in progress and to control air turbulence. A screw rod operated beam made of an insulating material was inserted inside the chamber so that height of the beam could be adjusted. The other column of the beam was firmly grounded on the table. A nozzle (20 gauge diameter) was inserted inside the chamber over the end of the beam in the provision provided using the screw type arrangement. The nozzle was made of stainless steel for electrical conductivity and mechanical strength. A Syringe pump (Larsen & Toubro Ltd., Model No: SP102 with flow rate: 0.1–999 mL/hr) was used to feed the solution to the nozzle. A syringe (20 mL) was used as a piston and cylinder and is connected to the feed pump. A flexible tube (3 mm diameter) was connected between the syringe and the nozzle. A regulated High Voltage DC power supply (Glassman High Voltage Inc., New Jersey, USA, Model No: EH30P3) with output voltage range 1–30 kV was used for electrospinning. The positive terminal of the transformer was connected to the nozzle so that when the material is flowing it gets positively charged. The negative terminal of the transformer was connected to the collector plate. The electrospinning takes place in the gap between the nozzle and collector plate. The method was optimized by analyzing various combinations of electrospinning parameters, such as, polymer concentration, applied voltage, nozzle-collector distance, needle gauge and flow rate in order to obtain uniform nanofibers. All experiments were carried out under ambient conditions (temperature: 29°C, *RH* = 60%). Optimized voltage used for this study was 25 kV for 10 wt% PVA concentration mixed with 1 wt% MWCNTs with needle-to-collector distance of 20 cm. Flow rate used was 0.8 mL/hr using a 20 gauge needle.

3. Results and discussion

3.1. Electrostatic field analysis for the prediction of fiber alignment

According to the literature, the electric field distribution plays a major role in controlling fiber alignment. In this scenario, a detailed study of electric field distribution for collector configuration is essential for understanding the phenomenon of fiber alignment. To probe this phenomenon the electrostatic field distributions of various collector geometries were plotted using electrostatic module of COMSOL Multiphysics software. A potential of 25 kV was applied at the needle tip and the collector plate was grounded. The collector material and the medium surrounding the collector were modelled as aluminium and as air respectively. After subsequent meshing, the computation results were acquired. From the electrostatic field analysis, it was observed that creating a slot in a collector plate introduced an insulating air gap which significantly alters the electric field. To study the influence of such insulating air gaps on electrostatic field distribution, the collector plates were modelled with slots having varied geometries (triangle, square, rectangle, semicircle and circle). The corresponding electrostatic fields are depicted in Figure 1. By analyzing the electric field plots, the region of fiber alignment within the slot geometry could be predicted. The analytical predictions were compared with electrospun fibers obtained experimentally on collector plates to estimate the accuracy of predictions. Figure 1a shows the electrostatic field pattern in a square slot. The field arrows are parallel at the middle of the square. The field near the corners could be resolved in order to obtain parallel field along lines perpendicular to the bisector of the vertex. Hence, the fibers are expected to be aligned at the middle of the slot and at the corners. The fibers follow the direction of the lines perpendicular to the bisector of the vertex. As depicted in Figure 1b, the field distribution within the collector with a rectangular slot is very much similar to that of the parallel plate electrodes reported in literature. Hence better alignment of the fibers is expected in the middle of the slot, except at the extreme edges where the field is randomly oriented. Figure 1c represents the electric field lines in a rectangular slot with circular ends. In this case, the lateral com-

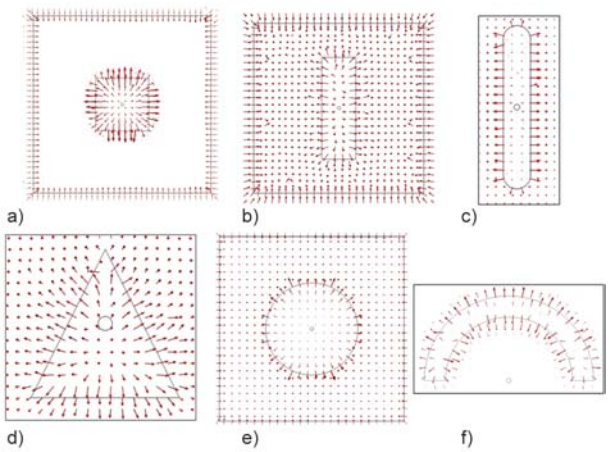

Figure 1. Electric field distribution in various geometric slots: (a) square, (b) rectangular, (c) rectangular slots with circular ends, (d) triangular (e) circular and (f) semi annular slots

ponent is radial near the circular ends and parallel in the rectangular portion. The parallel directions pointing outward indicate repulsive field in the slotted portion. This parallel repulsive electrostatic field is similar to that of the parallel plate collectors reported in literature and hence good fiber alignment is expected in the rectangular region. But, at the ends there is no such uniform field exists and hence random fiber orientation is expected. The electric field plot for triangular slot in Figure 1d indicates that the field tends to bend at the edges creating a lateral component. The combined effect of the lateral component of the two intersecting edges induces the fiber alignment. The electrostatic field at the corners could be resolved to obtain a parallel repulsive field in the direction normal to the bisector of the vertex. Thus, the fibers are expected to be aligned in the direction normal to the bisector of the vertex. Since the field direction is axial at the center of the triangle fiber formation in this region is difficult. The electrostatic field in circular slot shown in Figure 1e is uniformly radial in all directions; therefore the fibers are expected to be straight without any curvature but could not be aligned in a particular direction since the field is uniform in all directions. Figure 1f depicts electrostatic field in the semi annular slot indicating radial electric field distribution. The lateral component of the field is parallel between the slots and hence, reasonable fiber alignment is expected in the slotted portion. The fiber alignment direction is supposed to be radial in accordance with the electric field. According to the electrostatic field analysis, among all the geometrical slots used for this study, rectangular slots with circular end showed maximum alignment of nanofibers in larger area compared to other geometries, which was further confirmed from electrospinning experiments using various geometries. Hence, collectors having rectangular slot with circular ends was chosen for further studies. Figure 2 shows various geometrical collectors (semi annular, triangular, square, rectangular and spherical) used for this study and the corresponding optical microscopic images of the electrospun PVA-MWCNT fibers which was found to be in accordance with electrostatic field analysis.

From the electrostatic analysis, it is evident that the electric field lines tend to bend near the slot edges

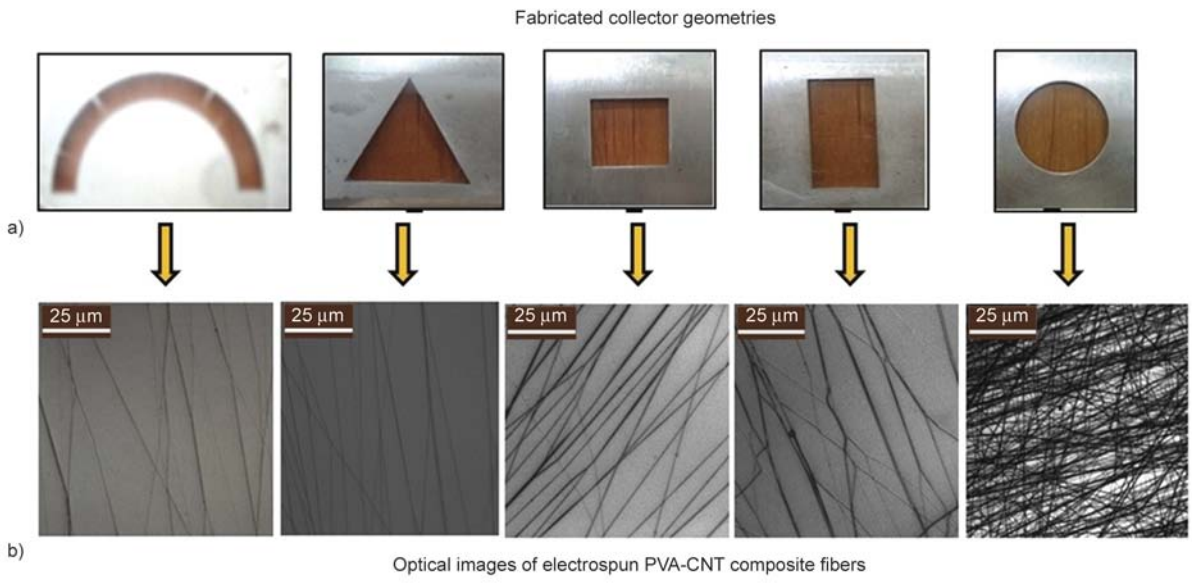

Figure 2. (a) Photographs of various geometrical collectors (semi annular, triangular, square, rectangular and spherical) and (b) corresponding optical microscopic images of the electrospun PVA-MWCNT fibers

in rectangular slot with circular edges as depicted in Figure 3b, 3c (the arrows near the slot edges were slightly bent, whereas arrows indicate the direction of the electric field). This bending of field lines creates a lateral component of the electric field in the plane of collector plate. The direction of the lateral component depends upon the geometry of the slot. From this analysis, the alignment direction of the nanofibers could be easily predicted. Hence, it is expected from this study that for a rectangular slot with circular ends, the parallel portions can produce aligned nanofibers, whereas, the circular ends cannot produce any aligned nanofibers. Further experiments using electrospinning proved that this prediction is valid and explained in the following sections. The as-produced electrospun nanofiber can be considered as a string of positively charged elements connected through a viscoelastic medium [39]. As

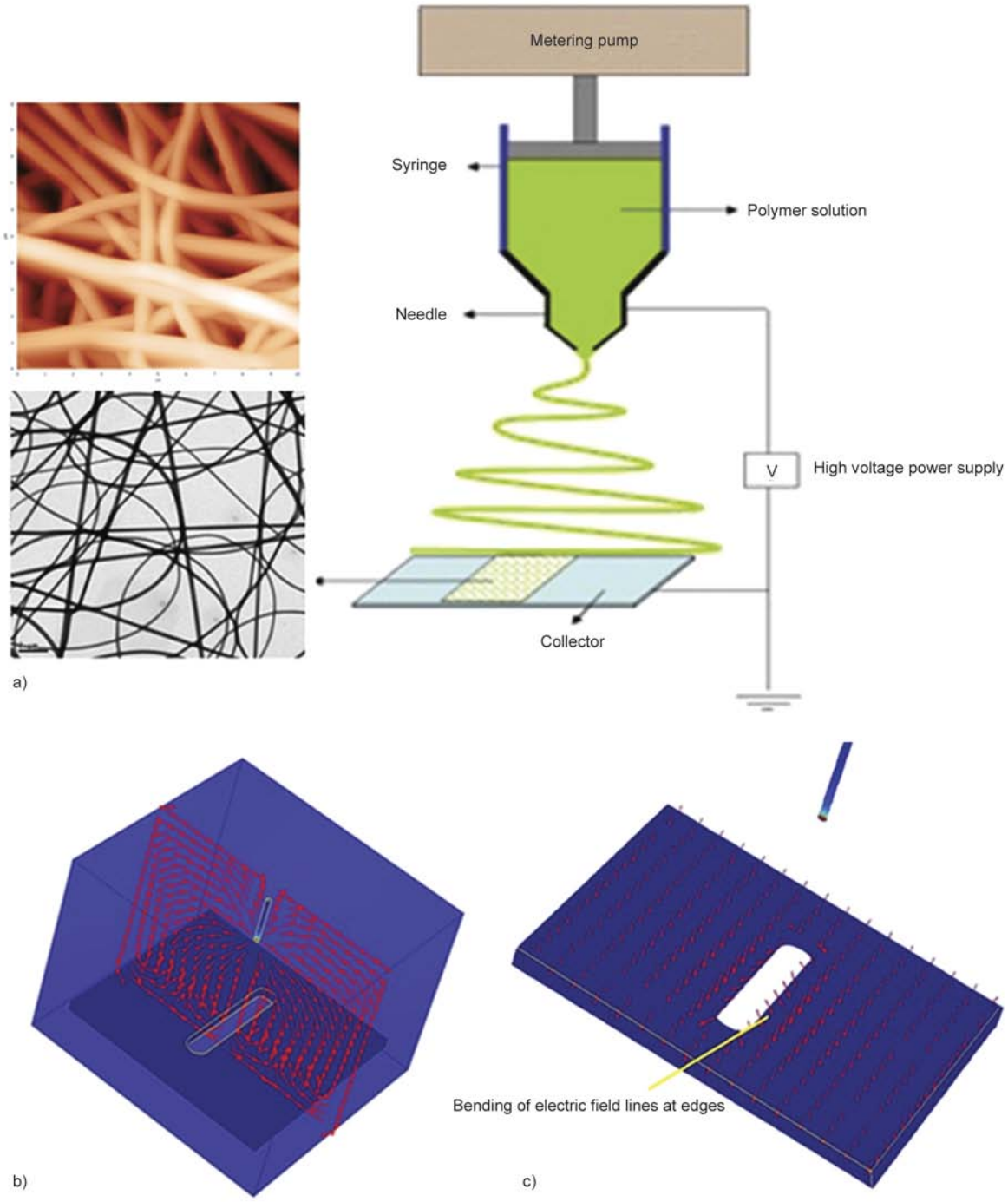

Figure 3. (a) Schematic representation of electrospinning (b) 3D view of electric field of rectangular slot with circular ends and (c) bending of electric field lines at edges of the slots

the charged fibers approach the vicinity of the electrodes, charges on the fiber start inducing opposite charges on the surfaces of the electrodes. Since Coulomb interactions are inversely proportional to the square of the separation between charges, the two ends of the fiber closest to the electrodes should generate the strongest electrostatic force. This force stretches the nanofiber across the gap, perpendicular to the edges of the electrode. Though the fibers deposited directly on the electrode get immediate discharge, those present in the air slots remain charged. Thus, the electrostatic repulsion between the deposited and the upcoming fibers enhances the alignment process.

3.2. Microscopic analysis of PVA-MWCNT composite nanofibers

Figure 3a depicts the schematic representation of the electrospinning process used for the fabrication of nanofibers. Inset shows the representative AFM and TEM images of the PVA-MWCNT nanofibers formed on a flat aluminium collector plate without any geometrical slots. This clearly shows the random orientation of the PVA-MWCNT nanofibers on the collector plate. The feed solution used for electrospinning was an aqueous dispersion of 10 wt% PVA and 1 wt% MWCNT. In order to confirm the presence of MWCNTs embedded in PVA nanofibers, the PVA-MWCNT composite fibers were first electrospun onto carbon coated copper grids for high resolution transmission electron microscopic analysis. Figure 4 depict a comparative analysis of bare PVA nanofibers and PVA-MWCNT composite nanofibers produced directly on TEM grid by electrospinning using HRTEM. Figure 4a, 4b shows the TEM images of bare PVA nanofibers having diameter in the range of 180–380 nm. The diameter of PVA-MWCNT was found to be decreased slightly (100–345 nm) with the loading of MWCNT as depicted in Figure 3c–3f. The high resolution images show the presence of embedded multiwalled carbon nanotubes in the electrospun PVA nanofibers as highlighted in Figure 4d–4f. The diameter of embedded carbon nanotubes was found to be ~20 nm. In order to verify the analytical predictions based on electrostatic field distribution discussed in the above section, electrospinning experiments were carried out using the collector plates having varied slot geometries machined using EDM. The as-produced fibers were electrospun onto each collector geometries and were characterized using TEM, SEM and Optical microscopy.

Figure 5 depict the SEM images of the fibers electrospun on rectangular slotted collector with rounded ends. It is evident that the direction of fiber alignment is parallel between the two opposite edges of the slot. The fibers were found to be well-aligned at the centre region of the slot as indicated in Figure 5a–5c and at the rounded end portion significant alignment could not be achieved due to the intermixing of radial alignment (Figure 5d). The results were matching well with the electric field predictions performed on the rectangular slotted collectors with circular ends. The fiber alignment at the edge of the slot also was not satisfactory as it represents the zone of transition from random fiber orientation over the flat portion of the collector to the well aligned region between the slots. The radial distribution of the field at the rounded end portions did not cause any significant alignment of fibers. In addition to this, the residual charges of the previously formed fibers may also influence the fiber alignment. Effect of spinning time was studied to infer how the thickness of the mat influences the alignment of nanofibers. PVA-MWCNT nanofibers were collected after electrospinning for 1, 5, 10, 20 and 30 minutes. Figure 6a–6e shows the SEM images of PVA-MWCNT nanofibers collected using 10 mm rectangular slotted collectors with circular ends with increasing electrospinning time until 30 minutes. It is evident that with increase in the electrospinning time, the degree of alignment was decreasing. Figure 6f shows the SEM image of bare PVA nanofibers collected after 10 minutes of electrospinning. Table 1 summarises the effect of electrospinning time on the degree of alignment of the nanofibers. The analysis of fiber orientation also shows that the degree of orientation of the nanofibers was not significantly affected by MWCNT loading, but it definitely decreased the diameter of the composite nanofibers formed as clear from Figure 5. The slight decrease in diameter for PVA-MWCNTs nanofibers compared to bare PVA nanofibers during alignment may be due to the contribution of the conductive components, MWCNTs reinforced in PVA. In addition, the hydrogen bonding interactions between the hydroxyl groups present in PVA and carboxyl groups present on the acid treated MWCNTs can also contribute to the reduction in PVA-MWCNT fiber diameter. The

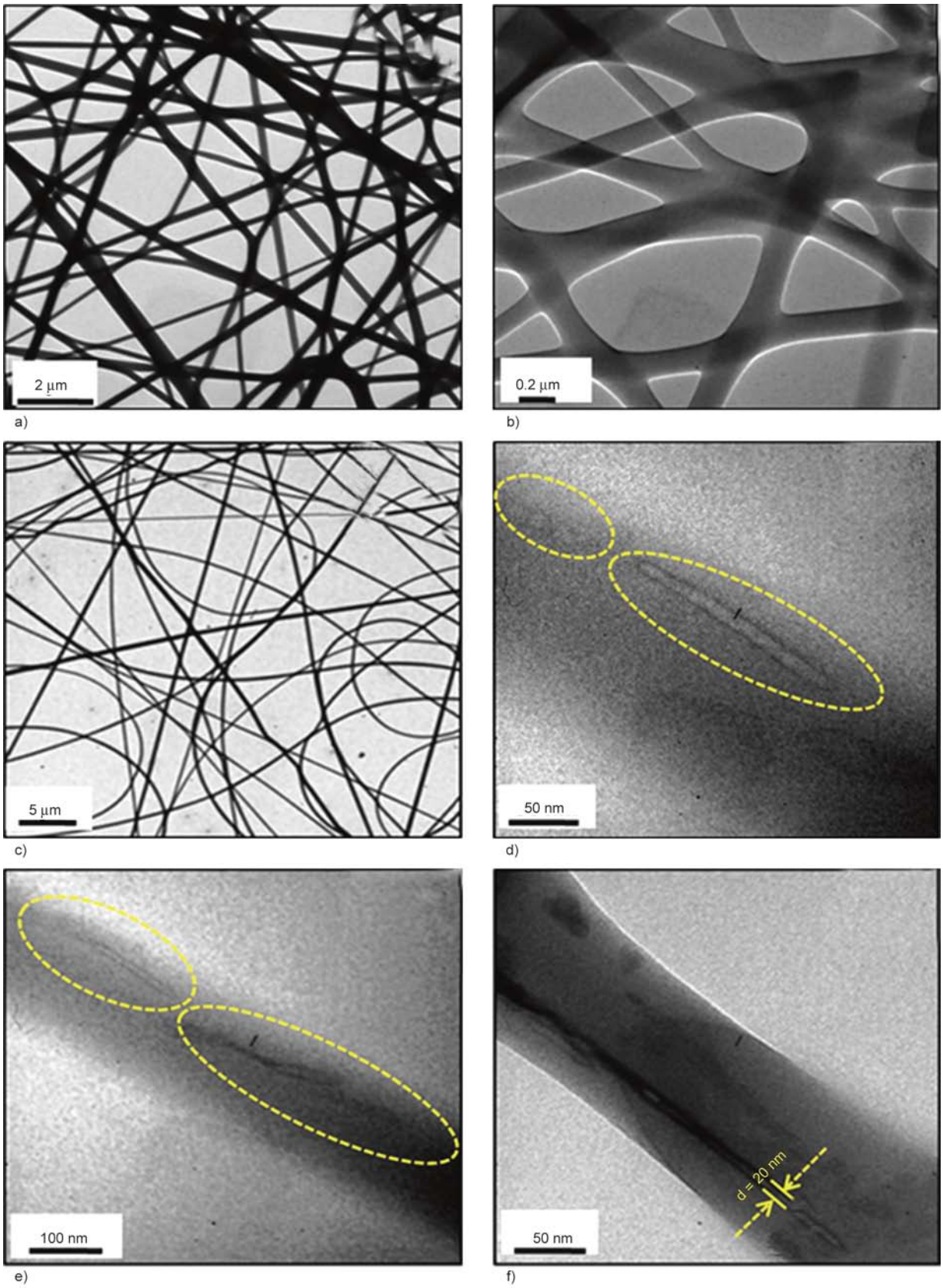

Figure 4. (a, b) Representative HR-TEM images of 10 wt% PVA nanofibers and (c–f) PVA-MWCNT (1 wt%) composite nanofibers produced by electrospinning process. Highlights: MWCNTs embedded in PVA nanofibers.

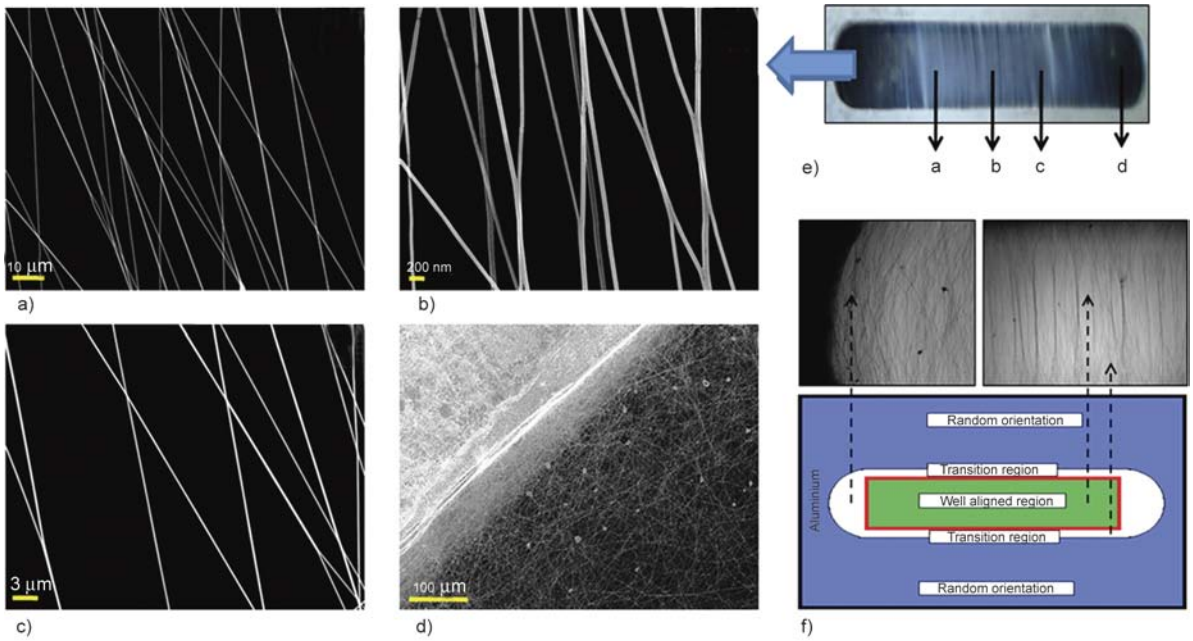

Figure 5. Representative SEM images of (a–d) the electrospun PVA-MWCNT composite nanofibers at varied places as indicated in (e) rectangular slot (10 mm) with circular ends and (f) schematic representation of regions of alignment on a rectangular slotted collector with circular ends and corresponding optical microscopic images

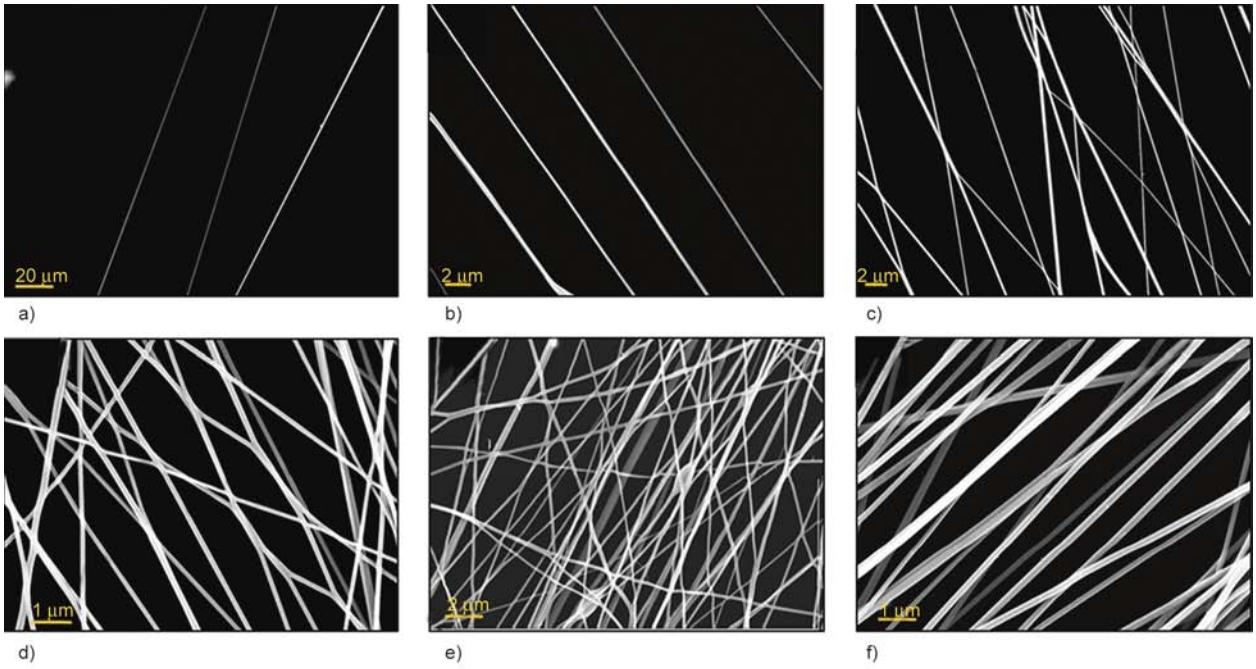

Figure 6. SEM images of PVA-MWCNT nanofibers collected using 10 mm rectangular slotted collectors with circular ends for electrospinning time (a) 1 min, (b) 5 min, (c) 10 min, (d) 20 min, (e) 30 min and (f) bare PVA nanofibers collected for 10 min

results indicate that the present technology can be used for aligned nanofiber integration onto devices, whereas, it is difficult to use this method for applications related to large area production of thick aligned mats.

Experiments were also performed by varying the slot widths of the rectangular slotted collectors with circular ends. It was observed that the fiber alignment was good in slots of 5, 7.5 and 10 mm, whereas, the fiber alignment was not satisfactory in the case of 20 mm slot. In the case of the collector with 20 mm slot, the slot width could be too long for the nanofibers to be supported between the slot edges. The fibers were unable to support in between the slot edges and were tending to break. The influence of the fiber diameter on slot width was studied after

Table 1. Degree of alignment of PVA-MWCNTs and PVA nanofibers as a function of electrospinning time

Spinning time [minutes]	Degree of alignment [°]
1	91
5	88
10	94
20	89
30	82
10 (PVA)	90

Table 2. Variation of average diameter as a function of slot width for rectangular slots with circular ends

Slot width [mm]	Average fiber diameter [nm]	Standard deviation [nm]
5	672	61.48
7.5	399	74.37
10	281	36.67
20	265	42.48

analyzing the corresponding SEM images. Figure 7 shows the representative SEM images of the electrospun nanofibers deposited on the rectangular collector having circular ends with slot widths, 5, 7.5, 10 and 20 mm respectively. The fiber diameter was found to be decreasing with increasing slot width. Average diameters of fibers along with standard deviation are listed in Table 2. Figure 8a depicts the plot showing the mean fiber diameter (collected using rectangular slotted collectors with circular ends) vs. slot width. The electrospinning experiments were carried out by fixing the parameters, such as, flow rate, voltage, needle gauge and screen distance and varying the slot width of the collector. The only change introduced was the modification in the electric field; hence the decrease in the fiber diameter must be directly related to the electric field influenced by slot widths. In order to find out the reason for this interesting phenomenon, 2D electrostatic field analysis was carried out for each slot width. The surface plot showing the electric field potential and electric field for rectangular slots with circular ends having 10 mm slot width is shown in Figure 8b. The top narrow rectangle represents the electrospinning needle and the two bottom rectangles represent the slotted collector plate in cross section. The top edge of the collector plate was taken as the X coordinate (–5 to +5) and the axial direction was taken as the Y coordinate. The maximum value of electric field occurs at the slot edges. The electric field lines bending towards the collector edge is resolved into horizontal (E_x) and vertical (E_y) components. From the electrostatic field analysis, it was clear that the E_x is maximum at the edges of the slot. It was found that the X component of the electric field E_x, increases with increasing slot width as shown in Figure 8d. The X component of the electrostatic force increases with increase in slot width, as the electrostatic force is proportional to

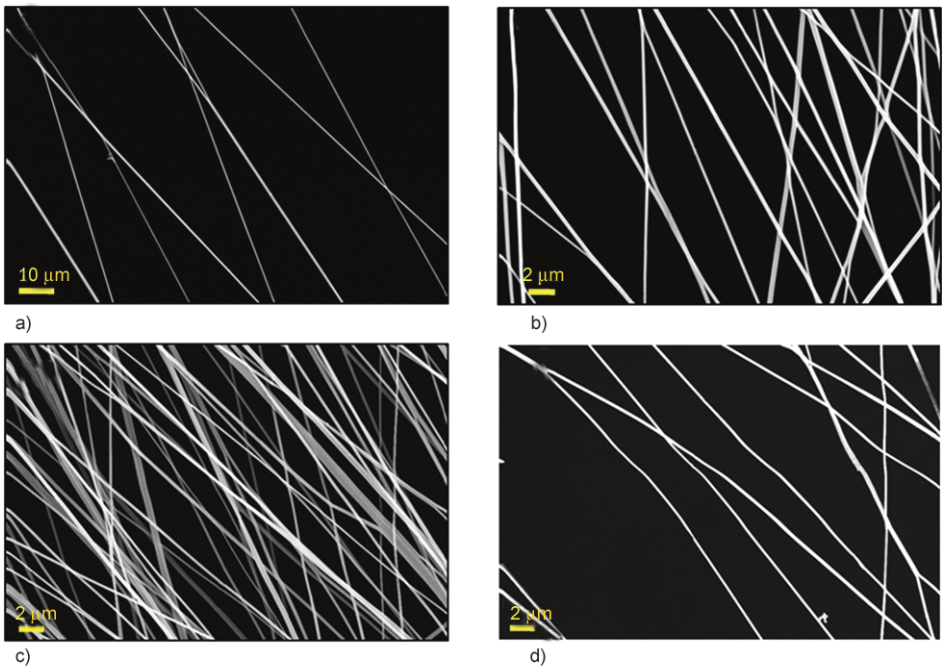

Figure 7. SEM images of aligned nanofibers collected using rectangular slotted collectors with circular ends for the slot width (a) 5 mm, (b) 10 mm, (c) 7.5 mm and (d) 20 mm

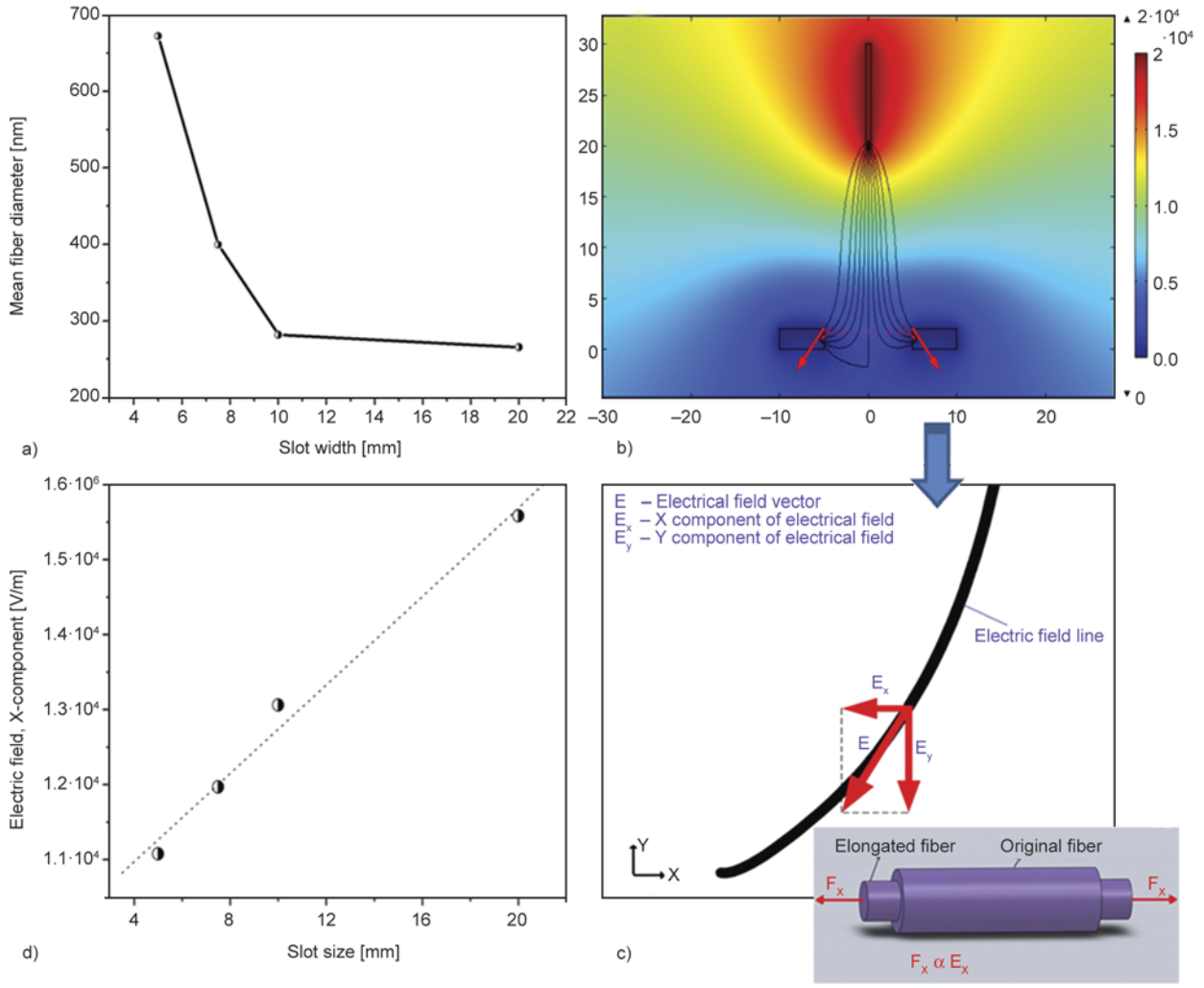

Figure 8. (a) Plot showing the mean fiber diameter (collected using rectangular slotted collectors with circular ends) vs. slot width, (b) surface plot showing electric potential (colour contour) and electric field (arrows and streamlines) for rectangular slotted plates with circular ends having slot width 10 mm, (c) magnified view of a representative electric field line bending towards the collector edge, which has been resolved into horizontal (*X*) and vertical (*Y*) components. Inset shows the schematic representation of fiber elongation due to axial elongation and (d) plot showing electric field (maximum values of *X* component of electric field) as a function of slot widths for rectangular slotted collectors with circular ends

the electric field. Hence, the force along the fiber axis increases with increasing slot size. In Figure 8c, the *X* component of the electrostatic force acting along the longitudinal axis of the fiber stretches the fiber leading to axial elongation. Whenever there is an axial elongation due to Poisson effect, there will be a lateral contraction leading to a reduction in the fiber diameter. Electrostatic field analysis also revealed that by increasing the slot width the electrostatic force along the fiber axis increases, leading to increase in axial strain which induces further reduction in fiber diameter. This best explains the phenomenon of decreasing fiber diameter with increasing slot widths.

Owing to the excellent electrical conductivity of MWCNT, electrical conductivity was found to be increased upon loading these conductive components into the PVA nanofibers. Figure 9 depicts the current-voltage (*I–V*) characteristics of the insulating PVA and conducting PVA-MWCNT nanofibers formed using rectangular slot with circular ends. As evident from the figure, the conductivity is significantly increased upon loading 1 wt% MWCNTs. This may be due to the introduction of MWCNTs into the PVA nanofiber matrix. As evident from TEM analysis, the MWCNTs have aligned parallel to the direction of axis of the nanofiber to form conductive chains during the electrospinning process.

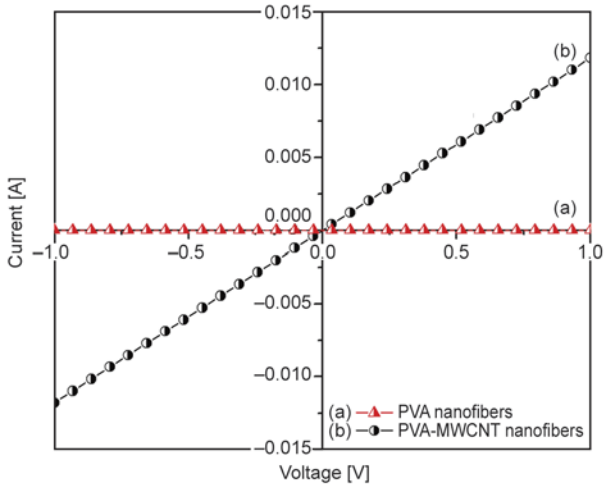

Figure 9. Current-voltage characteristics of (a) PVA nanofibers and (b) PVA-MWCNT nanofibers

The electrical conductivity of PVA-MWCNTs was calculated to be 0.025 S/cm from the *I–V* curves which indicates that the electrospun PVA fibers with aligned conductive components, such as, MWCNTs should be more feasible to conduct electrons when compared with insulating PVA nanofibers and therefore can be ideal candidates for sensor applications. Detailed study on the sensor property analysis of PVA-MWCNT nanofibers is currently ongoing in our laboratory. The investigation shows that the process can be further extended for creating aligned nanofibers onto various transducers having varied geometries and also for biomedical engineering, electronics, and energy storage systems. Apart from that this process can be adopted for the development of a range of materials, such as, polymeric, ceramic and composite based nanofibers. A detailed investigation on the application of this process for microelectrodes is currently investigated in our laboratory for the application of MEMS based sensor devices.

4. Conclusions

To summarize, a simple method based on electrostatic field analysis was used for the prediction of alignment of electrospun nanofibers for various collectors having different geometrical shapes. The nature of fiber orientation in each of the collector geometries were predicted and compared with the as-produced electrospun PVA-MWCNT composite nanofibers using electrostatic field analysis. Among all the collector slots, rectangular slotted collectors with circular ends were produced a good fiber alignment over large collecting area. Both the experimental and theoretical studies clearly indicated the introduction of an insulating region into a conductive collector and significantly influence the electrostatic forces acting on a charged fiber. PVA-MWCNT nanofibers were found to be conducting in nature owing to the presence of reinforced MWCNTs in PVA matrix. With the aid of electrostatic interactions, electrospun nanofibers could be assembled into controllable structures with varied configurations by varying the collector geometry. One of the most interesting features associated with this approach is that, this technique enables the direct integration of nanofibers with controllable configurations into an electrode system. These nanofibers can be fabricated and aligned simultaneously. This process can significantly simplify the production of nanofiber-based devices for biomedical engineering, electronics, and energy storage systems.

Acknowledgements

The authors acknowledge for the support and facilities provided by PSG Sons & Charitable Trust, Coimbatore, INDIA for carrying out the work.

References

[1] Wang M. C. P., Gates B. D.: Directed assembly of nanowires. Materials Today, **12**, 34–43 (2009). DOI: 10.1016/S1369-7021(09)70158-0

[2] Vomiero A., Ponzoni A., Comini E., Ferroni M., Faglia G., Sberveglieri G.: Direct integration of metal oxide nanowires into an effective gas sensing device. Nanotechnology, **21**, 145502/1–145502/8 (2010). DOI: 10.1088/0957-4484/21/14/145502

[3] Li D., Hu J., Wu R., Lu J. G.: Conductometric chemical sensor based on individual CuO nanowires. Nanotechnology, **21**, 485502/1–485502/6 (2010). DOI: 10.1088/0957-4484/21/48/485502

[4] Wang P., Zhao X., Li B.: ZnO-coated CuO nanowire arrays: Fabrications, optoelectronic properties, and photovoltaic applications. Optics Express, **19**, 11271–11279 (2011). DOI: 10.1364/OE.19.011271

[5] Ramakrishna S, Fujihara K., Teo W-E., Yong T., Ma Z., Ramaseshan R.: Electrospun nanofibers: Solving global issues. Materials Today, **9**, 40–50 (2006). DOI: 10.1016/S1369-7021(06)71389-X

[6] Ding B., Wang M., Wang X., Yu J., Sun G.: Electrospun nanomaterials for ultrasensitive sensors. Materials Today, **13**, 16–27 (2010). DOI: 10.1016/S1369-7021(10)70200-5

[7] Teo W. E., Ramakrishna S.: A review on electrospinning design and nanofibre assemblies. Nanotechnology, **17**, R89–R106 (2006). DOI: 10.1088/0957-4484/17/14/R01

[8] Lukáš D., Sarkar L., Martinová, Vodseďálková K., Lubasová D., Chaloupek J., Pokorný P., Mikeš P., Chvojka J., Komárek M.: Physical principles of electrospinning (Electrospinning as a nano-scale technology of the twenty-first century). Textile Progress, **41**, 59–140 (2009).
DOI: 10.1080/00405160902904641

[9] Bisht G. S., Canton G., Mirsepassi A., Kulinsky L., Oh S., Rankin D-D., Madou M. J.: Controlled continuous patterning of polymeric nanofibers on three-dimensional substrates using low-voltage near-field electrospinning. Nano Letters, **11**, 1831–1837 (2011).
DOI: 10.1021/nl2006164

[10] Yu D-G., Yu J-H., Chen L., Williams G. R., Wang X.: Modified coaxial electrospinning for the preparation of high-quality ketoprofen-loaded cellulose acetate nanofibers. Carbohydrate Polymers, **90**, 1016–1023 (2012).
DOI: 10.1016/j.carbpol.2012.06.036

[11] Yu D-G., Liu F., Cui L., Liu Z-P., Wang X., Bligh S. W. A.: Coaxial electrospinning using a concentric Teflon spinneret to prepare biphasic-release nanofibers of helicid. RSC Advances, **3**, 17775–17783 (2013).
DOI: 10.1039/C3RA43222J

[12] Cavaliere S., Subianto S., Savych I., Jones D. J., Rozière J.: Electrospinning: Designed architectures for energy conversion and storage devices. Energy and Environmental Science, **4**, 4761–4785 (2011).
DOI: 10.1039/C1EE02201F

[13] Teo W-E., Ramakrishna S.: Electrospun nanofibers as a platform for multifunctional, hierarchically organized nanocomposite. Composites Science and Technology, **69**, 1804–1817 (2009)
DOI: 10.1016/j.compscitech.2009.04.015

[14] Huang Z-M., Zhang Y-Z., Kotaki M., Ramakrishna S.: A review on polymer nanofibers by electrospinning and their applications in nanocomposites. Composites Science and Technology, **63**, 2223–2253 (2003).
DOI: 10.1016/S0266-3538(03)00178-7

[15] Orlova Y., Magome N., Liu L., Chen Y., Agladze K.: Electrospun nanofibers as a tool for architecture control in engineered cardiac tissue. Biomaterials, **32**, 5615–5624 (2011).
DOI: 10.1016/j.biomaterials.2011.04.042

[16] Carnell L. S., Siochi E. J., Holloway N. M., Stephens R. M., Rhim C., Niklason L. E., Clark R. L.: Aligned mats from electrospun single fibers. Macromolecules, **41**, 5345–5349 (2008).
DOI: 10.1021/ma8000143

[17] Jana S., Cooper A., Ohuchi F., Zhang M.: Uniaxially aligned nanofibrous cylinders by electrospinning. Applied Materials and Interfaces, **4**, 4817–4824 (2012).
DOI: 10.1021/am301803b

[18] Khamforoush M., Mahjob M.: Modification of the rotating jet method to generate highly aligned electrospun nanofibers. Materials Letters, **65**, 453–455 (2011).
DOI: 10.1016/j.matlet.2010.10.060

[19] Theron A., Zussman E., Yarin A. L.: Electrostatic field-assisted alignment of electrospun nanofibres. Nanotechnology, **12**, 384–390 (2001).
DOI: 10.1088/0957-4484/12/3/329

[20] Huang Y., Duan X., Wei Q., Lieber C. M.: Directed assembly of one-dimensional nanostructures into functional networks. Science, **291**, 630–633 (2001).
DOI: 10.1126/science.291.5504.630

[21] Katta P., Alessandro M., Ramsier R. D., Chase G. G.: Continuous electrospinning of aligned polymer nanofibers onto a wire drum collector. Nano Letters, **4**, 2215–2218 (2004).
DOI: 10.1021/nl0486158

[22] Chvojka J., Hinestroza J. P., Lukas D.: Production of poly(vinylalcohol) nanoyarns using a special saw-like collector. Fibres and Textiles in Eastern Europe, **21**, 28–31 (2013).

[23] Yang L., Yuan W., Zhao J., Ai F., Chen X., Zhang Y.: A novel approach to prepare uniaxially aligned nanofibers and longitudinally aligned seamless tubes through electrospinning. Macromolecular Materials and Engineering, **297**, 604–608 (2012).
DOI: 10.1002/mame.201100195

[24] Wang Y., Wang G., Chen L., Li H., Yin T., Wang B., Lee J. C-M., Yu Q.: Electrospun nanofiber meshes with tailored architectures and patterns as potential tissue-engineering scaffolds. Biofabrication, 015001/1–015001/9 (2009).
DOI: 10.1088/1758-5082/1/1/015001

[25] Xie J., MacEwan M. R., Ray W. Z., Liu W., Siewe D. Y., Xia Y.: Radially aligned, electrospun nanofibers as dural substitutes for wound closure and tissue regeneration applications. ACS Nano, **4**, 5027–5036 (2010).
DOI: 10.1021/nn101554u

[26] de Volder M. F. L., Tawfick S. H., Baughman R. H., Hart A. J.: Carbon nanotubes: Present and future commercial applications. Science, **339**, 535–539 (2013).
DOI: 10.1126/science.1222453

[27] Spitalsky Z., Tasis D., Papagelis K., Galiotis C.: Carbon nanotube–polymer composites: Chemistry, processing, mechanical and electrical properties. Progress in Polymer Science, **35**, 357–401 (2010).
DOI: 10.1016/j.progpolymsci.2009.09.003

[28] Jeong J. S., Moon J. S., Jeon S. Y., Park J. H., Alegaonkar P. S., Yoo J. B.: Mechanical properties of electrospun PVA/MWNTs composite nanofibers. Thin Solid Films, **515**, 5136–5141 (2007).
DOI: 10.1016/j.tsf.2006.10.058

[29] Ge J. J., Hou H., Li Q., Graham M. J., Greiner A., Reneker D. H., Harris F. W., Cheng S. Z. D.: Assembly of well-aligned multiwalled carbon nanotubes in confined polyacrylonitrile environments: Electrospun composite nanofiber sheets. Journal of the American Chemical Society, **126**, 15754–15761 (2004).
DOI: 10.1021/ja048648p

[30] Dror Y., Salalha W., Khalfin R. L., Cohen Y., Yarin A. L., Zussman E.: Carbon nanotubes embedded in oriented polymer nanofibers by electrospinning. Langmuir, **19**, 7012–7020 (2003).
DOI: 10.1021/la034234i

[31] Yeo L. Y., Friend J. R.: Electrospinning carbon nanotube polymer composite nanofibers. Journal of Experimental Nanoscience, **1**, 177–209 (2006).
DOI: 10.1080/17458080600670015

[32] Huang S., Yee W. A., Tjiu W. C., Liu Y., Kotaki M., Boey Y. C. F., Ma J., Liu T., Lu X.: Electrospinning of polyvinylidene difluoride with carbon nanotubes: Synergistic effects of extensional force and interfacial interaction on crystalline structures. Langmuir, **24**, 13621–13626 (2008).
DOI: 10.1021/la8024183

[33] Chen D., Liu T., Zhou X., Tjiu W. C., Hou H.: Electrospinning fabrication of high strength and toughness polyimide nanofiber membranes containing multiwalled carbon nanotubes. The Journal of Physical Chemistry B, **113**, 9741–9748 (2009).
DOI: 10.1021/jp9025128

[34] Zhang Q., Chang Z., Zhu M., Mo X., Chen D.: Electrospun carbon nanotube composite nanofibres with uniaxially aligned arrays. Nanotechnology, **18**, 115611/1–115611/7 (2007).
DOI: 10.1088/0957-4484/18/11/115611

[35] Yee W. A., Nguyen A. C., Lee P. S., Kotaki M., Liu Y., Tan B. T., Mhaisalkar S., Lu X.: Stress-induced structural changes in electrospun polyvinylidene difluoride nanofibers collected using a modified rotating disk. Polymer, **49**, 4196–4203 (2008).
DOI: 10.1016/j.polymer.2008.07.032

[36] Yang D., Lu B., Zhao Y., Jiang X.: Fabrication of aligned fibrous arrays by magnetic electrospinning. Advanced Materials, **19**, 3702–3706 (2007).
DOI: 10.1002/adma.200700171

[37] Tamura T., Kawakami H.: Aligned electrospun nanofiber composite membranes for fuel cell electrolytes. Nano Letters, **10**, 1324–1328 (2010).
DOI: 10.1021/nl1007079

[38] Rosca I. D., Watari F., Uo M., Akasaka T.: Oxidation of multiwalled carbon nanotubes by nitric acid. Carbon, **43**, 3124–3131 (2005).
DOI: 10.1016/j.carbon.2005.06.019

[39] Li D., Wang Y., Xia Y.: Electrospinning of polymeric and ceramic nanofibers as uniaxially aligned arrays. Nano Letters, **3**, 1167–1171 (2003).
DOI: 10.1021/nl0344256

eXPRESS Polymer Letters Vol.9, No.2 (2015) 119–128
Available online at www.expresspolymlett.com
DOI: 10.3144/expresspolymlett.2015.13

Improvements in thermoforming simulation by use of 3D digital image correlation

B. Van Mieghem[1,2*], *F. Desplentere*[2,3], *A. Van Bael*[1,2], *J. Ivens*[2,4]

[1]KU Leuven, Technology Campus Diepenbeek, Wetenschapspark 27, 3590 Diepenbeek, Belgium
[2]KU Leuven, Department of Materials Engineering, Kasteelpark Arenberg 44, 3001 Heverlee, Belgium
[3]KU Leuven, Technology Campus Ostend, Zeedijk 101, 8400 Ostend, Belgium
[4]KU Leuven, Technology Campus De Nayer Sint-Katelijne Waver, Jan De Nayerlaan 5, 2860 Sint-Katelijne-Waver, Belgium

Received 10 July 2014; accepted in revised form 23 September 2014

Abstract. Numerical simulation tools for the thermoforming of unfilled thermoplastic polymers already exist for a while, but are seldom used to full extent in industry. When it is used, it is mostly only for comparative studies and prediction of relative wall thickness. One of the major reasons is the difficulty to correctly calibrate and integrate all necessary material and process parameters into the simulation software. This paper introduces and validates a methodology, in which digital image correlation (DIC) is used as the key enabling technology that improves the knowledge of the process parameters and optimizes simulation accuracy by taking away a number of uncertainties and assumptions. DIC in combination with infrared thermal measurements and pressure monitoring is used to track sheet sagging and bubble inflation of a HIPS sheet, the two main process steps in the thermoforming of positive (male) products or the only two steps in the case of free forming. The results of these in-situ measurements are used as a guideline for selecting the correct input parameters in the commercial thermoforming simulation software T-SIM®. A similar methodology can be further implemented for subsequent process steps such as forming and cooling or even to validate the material data used in the simulation software.

Keywords: *modeling and simulation, industrial applications, thermoforming, digital image correlation*

1. Introduction

Thermoforming is a complex process that is characterized by many parameters affecting formability and product quality. The process complexity is further aggravated by the fact that the parameters can not necessarily be set independent of each other – when changing for example the sheet temperature, the tool contact friction, which plays a critical role in the thermoforming process, changes as well [1]. Precisely due to the complexity of the process, simulation software like Accuform's T-SIM® [2], Rheoware's FormView® and ESI's Pam-Form® can be used as a powerful tool in the designing phase of new products and molds, and in the optimization of the process settings with the aim of obtaining products with optimal quality, which generally corresponds to an optimal wall thickness distribution. Although the software is available, thermoforming on an industrial scale remains unfortunately primarily an experience and trial and error based technology. Failure to use simulation software has many causes. Firstly, the software mostly describes an idealized situation, differing from the real industrial environment. For example, the heating of blanks and cooling of tools is expected to be uniform in plane and homogenous through-the-thickness in simulations but this is rarely the case in reality. Secondly, the simulation software does not take into account

*Corresponding author, e-mail: bart.vanmieghem@kuleuven.be

all thermal and physical aspects of this complex process within its material models since not all characteristics of the large amount of possible thermoforming materials, at thermoforming conditions, have been researched and parameterized for usage in simulation software. Different material models were tested and compared to reality in either bubble inflation or actual forming experiments, an extensive overview of previous studies is given by O'Connor *et al*. in [3]. Thirdly, variation of process parameters in practice jeopardizes the process robustness and requires higher safety margins and initial blank thicknesses. Finally, when all abovementioned conditions are met, i.e. the process parameters are under control and a material model is chosen that accurately describes the material behavior, one extra issue remains in order to adequately execute a simulation that yields results that can be linked back to the process itself. This issue is the matching of the thermoforming machine settings to the parameters to be set in the simulation software (Figure 1). This is a critical part of the simulation since it is impossible to obtain realistic results when starting with the wrong simulation parameters; no adequate method to define this link has been found in literature by the authors.

In order to match machine settings to simulation software settings, in-situ three-dimensional Digital Image Correlation (DIC) [4], an optical non-contact full-field surface deformation measurement method, is a valuable technique [5]. DIC enables a sub-pixel measurement accuracy of displacements and strains on complex parts. In-situ DIC measurements make it possible to differentiate the effects of each process step (clamping, heating, forming, cooling) when used during the entire forming process. Whereas DIC is widely used for other applications where full field strain measurements are required, the use of DIC in

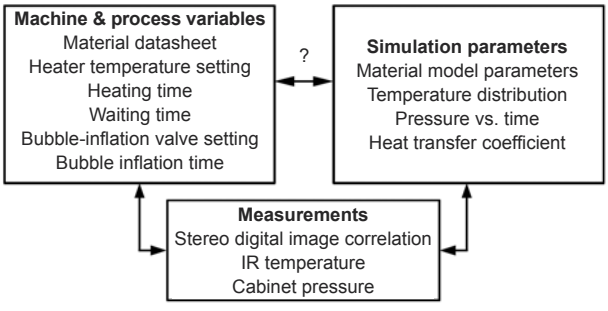

Figure 1. Schematic representation of the (unclear) relationship between process and simulation parameters

thermoforming applications is rare. Only two DIC studies for a thermoforming process are known to the authors [5, 6].

In the following section, a brief overview on how DIC is implemented in the thermoforming process and the specific measures that have to be taken into consideration when using DIC for thermoforming applications are itemized. Further paragraphs will elaborate on how DIC can be used to assist the thermoformer in optimizing the input data needed for correct sheet sagging and bubble inflation simulations, two main process steps in the forming of positive (male) products.

2. Materials and methods

2.1. Digital image correlation in thermoforming

The term digital image correlation refers to the class of non-contact measurement methods that acquire surface images of an object, store them in digital form, and perform image analysis to extract full-field shape and deformation measurements [4]. In order to be able to perform stable and sub-pixel accurate correlation, a random, non-repetitive, isotropic and high contrast speckle pattern has to be applied to a blank in order to ensure distinction between the pixels. For thermoforming applications in particular, some extra criteria come into play namely: temperature resistance (no discoloration, non-toxic at forming temperature), high strain resistance without cracking (risk of losing correlation), an impeccable bonding of the speckle with the blank (polymers tend to have low surface energy) and last but not least: for industrial applications, it should be easy, fast and cheap to apply. The best industrial option would be digital or silk screen printing. Paints and inks that meet the abovementioned requirements are commercially available, one example is the VUTEk GS-TF ink from EFI [7]. For current experiments, the sheet surface is spray speckled with a black custom-made spray-paint (Flanders Color – F122304 WB Elastic ACRYLIC) meeting all the requirements as specified above. Next, since a (grey scale) pixel-value is not a unique signature, a so-called subset is introduced which is a small, mostly square, surface of pixels that contains a combination of speckles and represents a unique signature in the picture. It is that subset that will be compared between the undeformed state (flat blank) and the deformed state (thermoformed product). Since the subset can change

position, shape and size during the forming process, the coordinates of each subset are related through a deformation matrix which is dependent on the expected deformation mode. For a rigid body motion, only a first order term is considered, but when an affine or irregular transformation is expected, higher order terms need to be used. Details on the exact process flow and the choice of the correlation algorithms are presented in [8] and [9]. The way DIC is implemented for the bubble inflation process is represented in Figure 2.

In this particular case, stereoscopic images are captured at a frame rate of 5 fps during the heating, sagging and bubble inflation phase and correlated in the 3D module of the academic correlation software MatchID (http://www.matchid.org). This software was benchmarked to the results of commercial systems [10] and it was found that for the bias, MatchID is in an identical range as VIC (Correlated Solutions (http://www.correlatedsolutions.com)) whereas an improved lower standard deviation by a factor of four was achieved. The correlation results in a full field displacement and strain map. If a subsequent conversion from strain to full-field wall thickness is required, it can be generated under the assumption of incompressibility and mass conservation, resulting in volume conservation [11], an hypothesis that has been validated for HIPS in [12] through shrinkage measurements. Further described experiments make use of a spray painted stochastic elliptical laser cut pattern where the minor axis of the undeformed ellipses at starting distance from the cameras correspond to 4 pixels, which is just above the minimum speckle size of 3 pixels that is appropriate for accurate matching and to ensure reasonable intensity pattern reconstruction via interpolation [4]. The oversizing of the speckles take already into account the increasing distance of the blank with respect to the cameras during sagging, leading to speckle size reduction. A subset size of 21 by 21 pixels and a step size of 10 pixels is chosen to ensure reasonable accuracy in the subset matching process. All important parameters necessary to evaluate the accuracy of the results are summarized in Table 1.

Concerning the hardware setup, two AVT Stingray F-201 cameras with Pentax high resolution, low distortion, 8 mm lenses are mounted on top of an Illig UA200ED cabinet thermoforming machine at a distance of approximately 1200 mm. This distance, combined with a correct aperture setting (*f*/8) and a

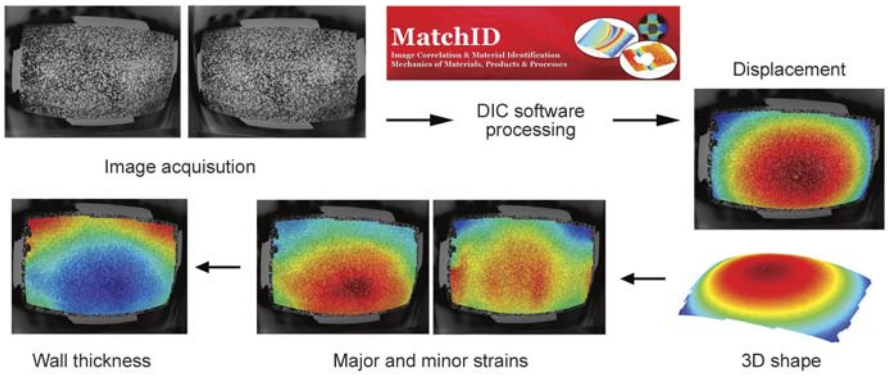

Figure 2. DIC applied to the bubble inflation process

Table 1. Digital image correlation parameters

Average noise Camera 0	0.6990%	**Displacement**		
Average noise Camera 1	0.6958%	Spatial resolution [px] and [mm]	21	13.104
Image pre-Filtering	Gaussian – Kernel 5	In-plane resolution [mm]	0.009269	
Subset size [px] / Step size [px]	21 / 10	Out-of-plane resolution [mm]	0.026502	
Correlation criterion	Zero-normalized sum of squared differences	**Strain**		
Shape function	Affine	Smoothing method	Bilinear quadrilateral	
Interpolation function	Bicubic polynomial	Strain tensor	Logarithmic Euler-Almansi	
Correlation progress	Spatial + Update reference (~ incremental)	Strain window [px]	10	
Measurement points	3256	Virtual strain gage [px] and [mm]	91	56.784
Total number of images	680	Spatial resolution [px] and [mm]	111	69.264
Pixel per mm [px/mm]	0,624	Resolution [μm/m]	68	

shutter time of 8 ms ensures that the product to be formed will be completely visible in the field of view of the cameras, the necessary depth of field is achieved and motion blur is reduced to a minimum. In order to get a uniformly lighted surface, two fluorescent diffuse spotlights are mounted on top of the thermoforming machine at an angle of 45° with respect to the thermoforming sheet. The cameras are first calibrated with an A3 format standardized dotted calibration pattern in order to capture the intrinsic (focal length in x and y direction, skew factor, distortion coefficient and principle point in x and y direction) and extrinsic (distance between the cameras in x, y and z direction and three inter-camera rotation angles) camera parameters.

One critical observation has to be made on the limitations of DIC in thermoforming: the area of interest where a DIC measurement is required needs to be in the field of view of the cameras during the forming process, making the process not ideally suited for matched die forming, pressure forming and for some plug assisted vacuum forming process variants. It is on the contrary ideally suited for standard vacuum forming processes and free forming process variants.

2.2. Simulation software

The aim of this research is to accurately simulate sheet sagging and bubble inflation, occurring during the heating step of most drape formed positive (male) products, in T-SIM® (V4.7a release 1). T-SIM® is a commercial thermoforming simulation software that uses the nonlinear time-dependent viscoelastic K-BKZ model that was proposed by Kaye [13] and Bernstein *et al.* [11]. Time-temperature superposition is obtained by the WLF equation [14].

In T-SIM®, in order to simulate sagging, no time dependent heating profile can be assigned to the sheet as it does occur in reality. In reality the sheet is at room temperature when clamped and subjected to a heating profile until the forming temperature is reached. Figure 3 and Figure 4 plot the infrared surface temperature as a function of time measured at the center of the upper side of the sheet during a positive thermoforming process of a 1 mm starting thickness HIPS sheet (in red). The blue bullets represent the differential pressure of the cabinet with respect to the surrounding. The steps that can be distinguished are: the gradual heating of the sheet with decreasing slope; the retraction of the heaters which is the turning point of the temperature curve; the bubble inflation phase which speeds up the cooling process; and finally the contact with a cold aluminum mold steepening the decreasing temperature curve even more due to the much higher heat transfer coefficient towards the mold compared to the air. The gradual heating results in a gradual loss of stiffness and consequent gradual sagging of the sheet. Since sheet sagging, if not well controlled, has a major influence on the final product thickness distribution [12], it should be accurately simulated as well. A temperature profile cannot be simulated in T-SIM® and the only way to incorporate sagging in a complete process simulation is by incorporating a waiting time at forming temperature. The weight of the sheet and gravity will induce sagging at the forming temperature. Obviously this waiting time is hard to predict since no reference data is available at the time a simulation is normally per-

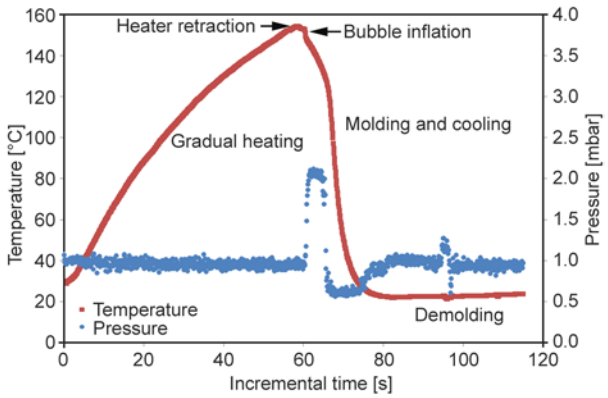

Figure 3. Typical temperature and pressure profile of a 1 mm thick HIPS sheet throughout heating, forming and cooling on an aluminum male mold

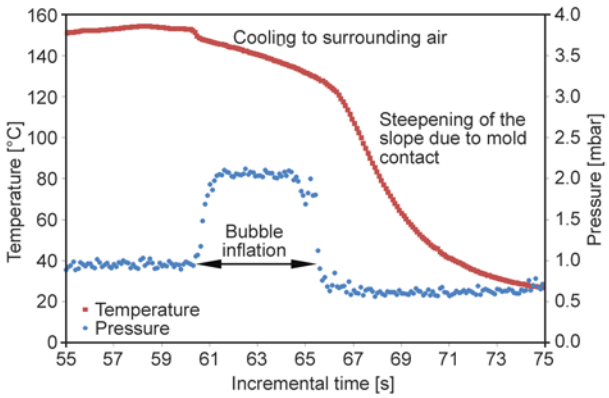

Figure 4. Detail of Figure 3 with focus on the bubble inflation

formed, i.e. at the start of a new production run. In order to set the correct waiting time, DIC is used as an auxiliary tool to measure the amount of sagging as function of time during heating. In the following paragraphs describing the experiments, the sheet is heated equally in the plane of the sheet, no patterned heating is used, edge effects are neglected and through-the-thickness temperature gradients are not considered.

In a second step, as is common practice for male molds, a bubble is inflated to acquire a more uniform material distribution of the final product [17]. Again, it can be understood that the height of the bubble, and the related strains in the sheet, will affect final wall thickness distribution and should therefore be predicted as accurately as possible by the simulation software. In T-SIM®, the bubble can be simulated by setting a pressure gradient (in kPa) as function of time (in milliseconds). On most of the thermoforming equipment used nowadays, the air flow, responsible for the pressure buildup underneath the sheet, is set by a proportional (often manual) valve. The direct link with the pressure as function of time used in simulation software is not that obvious to define. Again DIC, this time in combination with a pressure sensor in the lower cabinet of the thermoforming machine, enables for an accurate measurement of the bubble height and shape. Figure 5 schematizes the experimental setup. The validity of this approach has already been proven by Li *et al*. [16] who optimized the material parameters of the Mooney-Rivlin hyperelastic model in a bubble inflation test by observing the bubble shape with a high-speed optical surface measurement system. The system that the researchers used can be considered as a precursor of the present DIC systems without the possibility of determining in-situ strain and thickness.

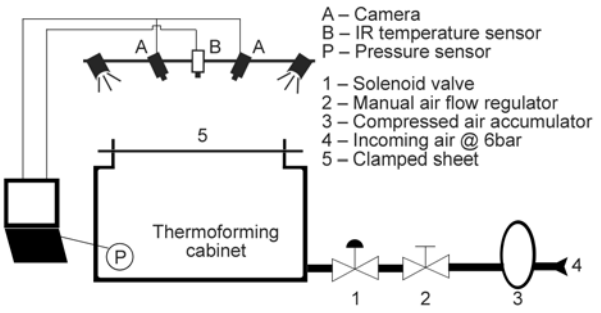

Figure 5. Measuring setup for sheet sagging and bubble inflation

2.3. Thermoforming equipment and material

The further described thermoforming tests have all been performed on an Illig UA200ED hydraulic thermoforming machine equipped with ceramic Elstein infrared heating elements installed in an upper and lower heater bank. The incoming air pressure of 6 bar is accumulated in a 90 L pressure vessel followed by a manual ball valve for the air flow setting and a solenoid valve to determine the time for the pressure build up. The free volume of the lower cabinet of the thermoforming machine and the piping connecting the cabinet to the accumulator is calculated approximately as 5170 L. In an ideal situation and assuming air as an ideal gas, the maximum pressure without edge losses that can be achieved when connecting the air accumulator to the lower cabinet would be 103 mbar. In order to accurately follow up the pressure build-up in the bubble inflation stage, a 0–1 bar pressure sensor (IFM electronics PA9027) is mounted in the lower cabinet. Only the lower heating bank is used to heat the sheet in order to keep the top surface free for monitoring the sheet deflections. The temperature is registered with an infrared (Fluke 576) thermometer at a rate of 10 Hz, a spot size of 23 mm (distance from the sheet 500 mm) and with an accuracy of ±0.75% of the reading. The sensor emissivity is set to 0.96, the average value obtained from material emissivity measurements of the used material. The clamping frame dimensions are set at 850 mm by 670 mm. The heater retraction takes 3.7 seconds to complete.

The material used for this investigation is an extruded grade of high impact polystyrene (HIPS: Metzeler – Metzoplast SB/HK), thickness 1 mm. In T-SIM® the sheet is modeled as 850×670 mm^2 with a thickness of 1 mm and consists of 9180 triangular element, fully constrained on the edges. A uniform sheet temperature of 150°C and an ambient temperature of 25°C is assumed. With current single sided infrared heating conditions and considering constant material parameters and constant convection losses at the sheet surfaces, a maximal gradient of 10°C between top and bottom of the sheet at the end of the heating stage is calculated by the finite differences method. After the retraction of the heaters, which takes 3.7 seconds, the maximal gradient within the 1 mm sheet drops below 2.5°C.

The material model parameters are based on the default HIPS material available in T-SIM's material library and are characterized by the K-BKZ Wagner I model (without strain hardening) with 8 pairs of relaxation moduli as function of time. Temperature effects are included by the WLF temperature dependency of the material parameters [14]. The time-integral constitutive equation is described by Equation (1) [17]:

$$\tau = \int_{-\infty}^{t} m(t - t')h(I_1,I_2)C^{-1}(t')\mathrm{d}t' \quad (1)$$

where τ is the resulting stress, m is the memory function, h is in this case the Wagner I damping function and C^{-1} is the left Cauchy-Green strain tensor. The memory function can be written as a sum of exponential functions involving couples of relaxation times (λ_k) and relaxation moduli (a_k) for N relaxation modes (Equation (2)):

$$m(t - t') = \sum_{k=1}^{N} \frac{a_k}{\lambda_k} e^{-\frac{t-t'}{\lambda_k}} \quad (2)$$

The Wagner I damping function h is defined by a single parameter α and the two strain invariants I_1 and I_2 (Equation (3)) [18]:

$$h(I_1,I_2) = \frac{1}{1 + \alpha\sqrt{(I_1 - 3)(I_2 - 3)}} \quad (3)$$

An overview of the material parameters necessary for this model are listed in Table 2. Only the heat capacity (1.2 kJ/(kg·K)) and the thermal conductivity (0.17 W/(m·K)) were modified with respect to the standard database data, according to the material supplier datasheet as these parameters play a critical role in the temperature gradient of the sheet as a function of time. Simulation is run with automatic step calculations.

Table 2. Relaxation spectra for HIPS from T-SIM® material database; α = 0.001, WLF parameters: C_1 = 17.44 K, C_2 = 51.6 K with reference temperature T_{ref} = 140°C

k	λ_k [s]	a_k [Pa]
1	0.0001	934 853
2	0.0012	206 823
3	0.017	177 543
4	0.24	122 675
5	3.3	36 507
6	47	4 653
7	640	80
8	8920	7.23

3. Results and discussion

3.1. Sheet heating and sagging

The sheet is heated from the bottom with ceramic heater setting at 300°C and the temperature and the displacement in height-direction of the center of the sheet, the location which is expected to sag the most, is measured from the top side as a function of time throughout the heating phase. Figure 6 represents the temperature and the absolute displacement of an averaged region of 21×21 pixels at the center of the sheet as a function of time. It can be seen that initially the sheet sags gradually. At the glass transition temperature (T_g = 96°C), relaxation undulations occur and disturb the gradual sagging but once T_g passed, sagging gradually continues with an increasing slope. At the point of retraction of the heaters (150°C sheet temperature), the sheet has sagged approximately 12 mm. During the heater retraction time (3.7 s) the sheets sags another 13 to 25 mm in total. This quick increase can be explained by the disappearance of the buoyancy effect: the convection of the hot air underneath the sheet creates a supporting force during heating, from the moment the heaters retract, this lifting effect is no longer present and the sheet sags with increased speed. A similar effect is expected to be present at the moment there would be a delay between sheet sagging compensation, which is not used in present study, and subsequent bubble inflation or vacuum forming.

In order to simulate sagging correctly, in T-SIM®, the sheet is initially set to 150°C and subjected to gravity for a period of time (waiting time) during which the sheet sags and cools down due to its exposure to ambient air. The cooling is dominated by convective heat transfer from the sheet to the environ-

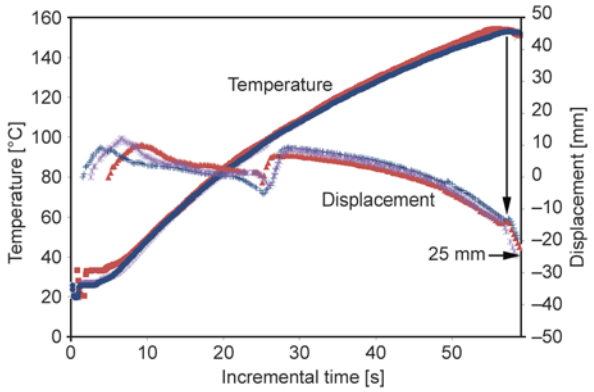

Figure 6. Temperature and displacement of the center of the sheet as a function of time during heating phase (3 repeats)

ment and a minor portion by radiation. This statement is confirmed by performing a finite element transient thermal simulation (Siemens Unigraphics NX) of the cooling of a plate with realistic size and process conditions. Since separating these two effects is a complex process and radiation cooling parameters cannot be set separately in T-SIM®, the total cooling is represented by a convective coefficient. From literature [15], it would be acceptable to take 5.7 W/(m^2·K) as a realistic convective heat transfer coefficient, but in present study the real coefficient is calculated by performing a heat-cool cycle on a 1 mm sheet without application of any pressure or vacuum. The temperature of the first 5 seconds of the decreasing slope, which is quasi-linear, is then fitted according to Newton's law of cooling; which is a discrete analog of Fourier's law, with different values for the heat transfer coefficient (Equation (4)):

$$T_t = \left[(T_{(t-1)} - T_{amb}) \cdot e^{-\frac{\theta_{(t)} \cdot h}{\rho \cdot c_p \cdot L_{(t)}}} \right] + T_{amb} \qquad (4)$$

with temperature T, time t, ambient temperature T_{amb}, time increment θ, convective heat transfer coefficient h, density ρ, heat capacity c_p and characteristic thickness L – which is the thickness of the sheet. From Figure 7 it is clear that the best matching convective heat transfer coefficient for the measured free cooling curve has a value of 16 W/(m^2·K). In order to illustrate the effect of the coefficient on the slope of the curve, curves for h = 5.7 W/(m^2·K) and h = 30 W/(m^2·K) are also drawn.

As the T-SIM simulation software cannot cope with gradual heating and sagging of the sheet, the delay time in the simulations was chosen so that it corresponds to the same amount of sagging as observed experimentally by DIC measurements. This results in an artificial delay time of 5 ms for the sheet. The 25 mm deep sagged shape after 5 ms is exported and used as the reference shape in the subsequent bubble inflation simulation. The choice of the correct waiting time, reflecting the correct sagging amount, would be an impossible task without accurate experimental data. Because of the short amount of time and the heat transfer coefficient of 16 W/(m^2·K) between sheet and surrounding air, the sagging process does not affect the initial temperature of the sheet much in the simulations. An average through thickness temperature drop of only 1°C is found.

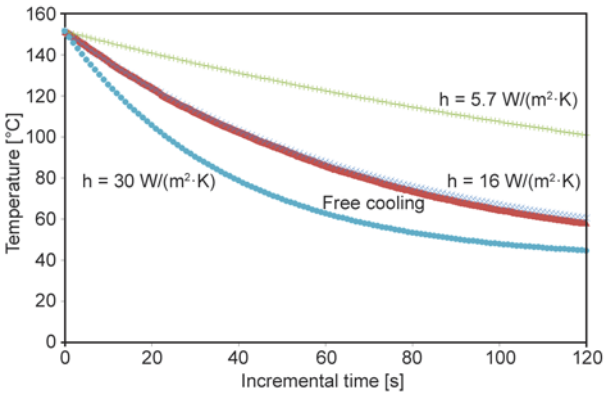

Figure 7. Fitting a cooling curve for a 1 mm (initial thickness) HIPS sheet at starting temperature of 150°C with different convective heat transfer coefficients. 16 W/(m^2·K) yields the best results

3.2. Bubble inflation

At first, bubble inflation is simulated in T-SIM® with settings from literature [15]: pressure between 140–280 mbar during 5 seconds which is the time needed for a typical male mold on the Illig machine to reach its top position; convective heat transfer coefficient should be between 5.7 W/(m^2·K) for quiescent air and 57 W/(m^2·K) for forced air convection (chosen value for simulation: 16 W/(m^2·K) from previous experiments) and an ambient temperature of 25°C. These settings however result in unrealistic bubble inflation heights reaching more than 1200 mm followed by sheet bursting. For more realistic simulation results, it is recommended to experimentally determine the combination of temperature, pressure and strain measurements.

The pressure build-up during bubble inflation, which is an equipment related value that is affected by the general air pressure on the incoming line, the diameter and resistance of the piping, the setting of the air flow valve, the volume of the compressed air accumulator vessel (if available), the volume of the lower cabinet that needs to be filled and the losses due to non-perfect airtight closure of the lower cabinet, is monitored with the 0–1 bar pressure sensor connected to a high resolution data acquisition system (16 bit) at a rate of 10 Hz. Experiments showed that the position of the pressure monitoring device in the cabinet is of little importance on the pressure values. To characterize the machine, in a first step, the effect of the different settings of the air flow valve (1–10) on the pressure are tested with a rigid sheet clamped in the machine to close the cabinet. The pressure as a function of time is plotted in Figure 8. With valve settings 1 and 2, the opening of the

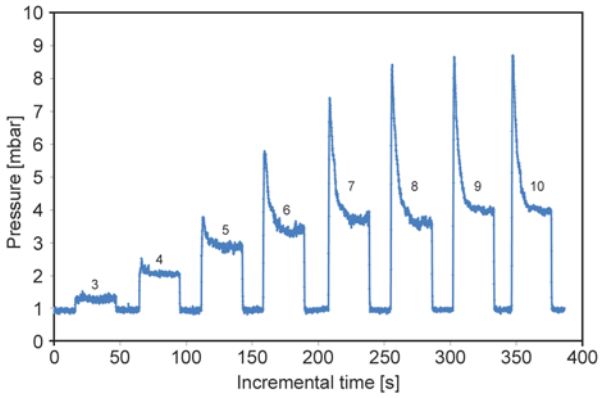

Figure 8. Lower cabinet pressure as a function of time for the different flow valve settings.

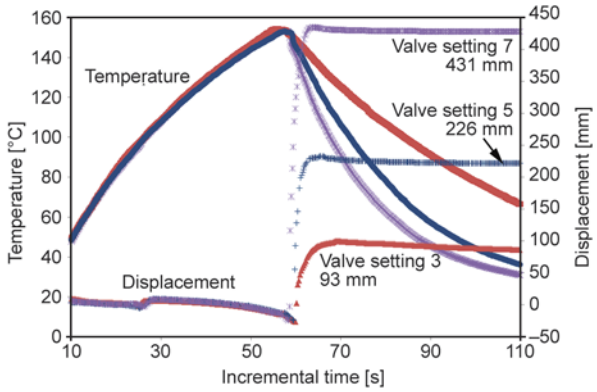

Figure 9. Temperature and displacement of the center of the sheet as a function of time for three settings of the pressure valve

valve is too small to overcome the losses and the pressure gradients are therefore not represented in the graph. As a general observation on Figure 8, it can be noticed that irrespective the setting of the valve, in the first 500–1000 ms a quick pressure is built-up due to the fast decompression of the compressed air inside the accumulator vessel. The higher the setting of the air flow valve, the higher the peak value becomes. Once the accumulator is empty, the pressure only depends on the direct flow rate from the incoming pneumatic airline, affected by the throttling effect of the ball valve, reduced by the leakage losses. The pressure value decreases to a stable value representing the equilibrium between the leakage losses and the fresh incoming air. From setting 7 and above, the pressure in the equilibrium phase is practically identical. The measured pressure gradients are machine specific and only need to be monitored once, since they are unaffected by the type of material or mold used. Important to remark is that for some faster applications where the bubble inflation step takes less than 1 second, the pressure gradient will still be in the rising part of the curve. In the current research, inflation takes 5 seconds meaning that not only the rising part but also the rest of the profile needs to be used.

After the heating phase, the sagged sheet is subjected to a bubble inflation step with three different settings of the air flow valve (3, 5 and 7), leading to three different strain rates and displacements of the center point of the bubble (Figure 9). With valve settings below 3 (meaning 30% of the maximum valve opening) the pressure is insufficient to lift the sheet, above 7 (70%) the sheet ruptures. Concerning the response on the pressure build-up, one can distinguish two effects: the higher the pressure, the higher the bubble will be, which is obvious, and the faster the sheet will cool down. The faster cooling response is caused by two phenomena: firstly, the higher the pressure, the more turbulent the air will be, leading to a higher heat transfer coefficient between sheet and air and secondly, since the sheet thickness reduces at the same time, the local heat flux density increases inversely proportional to the sheet thickness according to Fourier's law of heat conduction. Similarly to the calculation of the convective heat transfer coefficient during sagging, the linear part of the decreasing cooling slope is fitted according to Equation (4). The only difference is that the effective thickness reduction as a function of time ($L_{(t)}$), as calculated using DIC data, is taken into account. The correct calculation of the heat transfer coefficient is not possible if the thinning effect during the bubble inflation is not included, this is what the real advantage of DIC means in this case. A detailed description of the use of DIC for online thickness measurement can be found in [5]. The calculated coefficients are 26, 31 and 32 W/m²K for valve settings 3, 5 and 7 respectively (Figure 10).

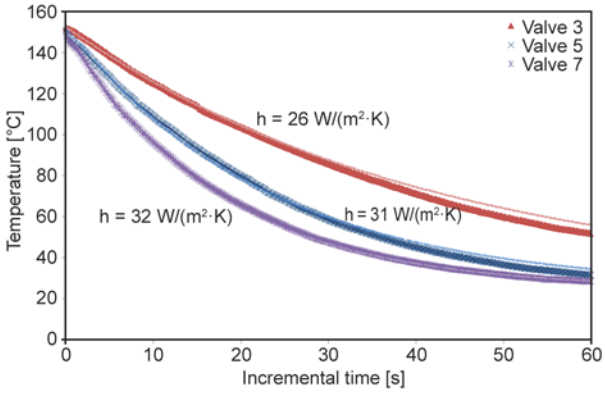

Figure 10. Fitting of the convective heat transfer coefficients to the cooling curves during bubble inflation for valve settings 3, 5 and 7

The calculated convective heat transfer coefficient and the pressure gradient during 5 seconds for valve setting 3 are entered in T-SIM® and a simulation is run leading this time to a more realistic bubble height of 90.5 mm. When comparing the bubble height obtained with T-SIM® to the DIC measurements (93 mm after 5 seconds (Figure 9)), it can be concluded that the result are within an allowable tolerance (3%) and that the material model for the simulated strain rates and temperatures is adequate. A similar simulation strategy is adopted for inflation valve settings of 5 and 7 but in these cases, the simulation needed to be interrupted after 1.5 and 1 s respectively since stress-strain and temperature extrapolation errors occurred around 135°C. This simulation problem does not affect the fact that the methodology can be used with proper functioning thermoforming simulation software. The respective height deviations from the DIC data are with these valve settings 12 and 9%.

Next to the bubble height, which is a single point value, the 3D point cloud of the top surface of the final shape obtained with valve setting 3 is exported, meshed and matched to the exported final shape of the bubble created in T-SIM® using GOM Inspect® V7.5, a freeware 3D inspection and mesh processing software for dimensional analysis of 3D point clouds (http://www.gom.com). The matching process proves that not only the height of the bubble is correct, but that there is also a quasi-perfect agreement in bubble shape (Figure 11).

The real asset of using DIC and measuring the shape of a whole surface instead of a single point in the middle as can be done by a height acquisition device or a light curtain, which is currently industrially used to measure the bubble height, is that also wanted or unwanted asymmetries created either by un-uniform heating in plane or by extrusion anisotropy caused by the prior sheet extrusion process [12], can also be identified and matched.

It is expected that the adopted methodology is applicable for any unreinforced thermoplastic material as long as the assumption of volume conservation is valid and no through thickness shear occurs since this could lead to erroneous predictions of the final thickness based on measurements of the non-mold contact surface. However, if there is a need for extrapolating the results to thicker plates, care must be taken during heating to minimize the through thickness temperature gradient.

4. Conclusions

In this paper, DIC is used together with online temperature and pressure measurements to track sheet sagging and bubble inflation of a HIPS sheet. The measurements are used to set the correct input values (amount of sagging, pressure gradient, temperature, convective heat transfer coefficient) in a commercial thermoforming simulation software T-SIM®. For the experiment with a 850×670×1 mm sheet, a waiting time of 5 ms at forming temperature (150°C) could be defined, leading to 25 mm sagging. For the bubble inflation, the real pressure gradient in combination with the thickness-corrected convective heat transfer coefficient, from temperature and DIC measurements, are required to predict the bubble height within an acceptable accuracy of around 3% where simulation was practically impossible without this knowledge. The simulation software can now be used to optimize bubble height and shape and the simulation parameters can directly be linked back to the machine settings since the actual pressure profiles are known. The methodology can in this way be used to generate experimental data in a very easy and straightforward way in order to optimize simulation accuracy and shorten the trial and error methodology used nowadays.

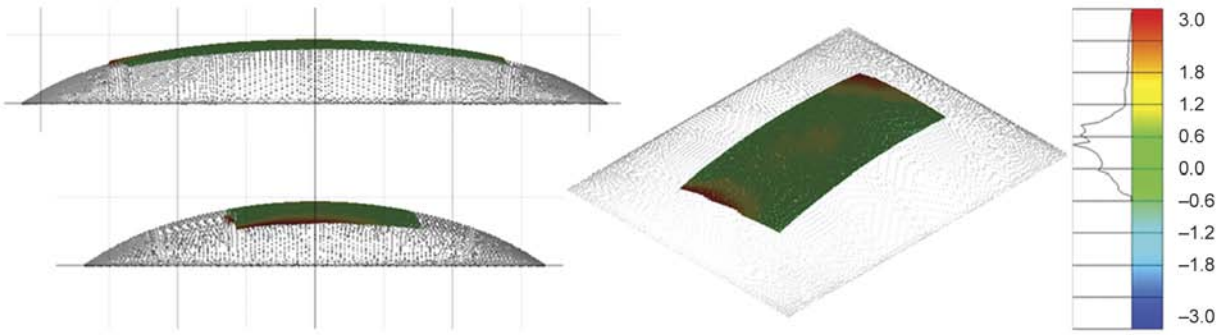

Figure 11. 3D matching of DIC and T-SIM® shape of a bubble inflated with valve setting 3. Color scale in mm.

A similar approach can be further implemented for other materials and material thicknesses, process steps such as forming and cooling or it can be used to validate the material parameters of the KBK-Z (or any other material) model by implementing a reverse engineering approach on different pressures and temperatures.

Acknowledgements

The authors would like to thank the MeM2P group of KU Leuven campus Ghent for providing the DIC platform MatchID3D and their technical support.

References

[1] Martin P. J., McCool R., Härter C., Choo H. L.: Measurement of polymer-to-polymer contact friction in thermoforming. Polymer Engineering and Science, **52**, 489–498 (2012). DOI: 10.1002/pen.22108

[2] Novotný P., Sáha P., Kouba K.: Fitting of K-BKZ model parameters for the simulation of thermoforming. International Polymer Processing, **14**, 291–295 (1999). DOI: 10.3139/217.1543

[3] O'Connor C., Martin P. J., Sweeney J., Menary G., Caton-Rose P., Spencer P. E.: Simulation of the plug-assisted thermoforming of polypropylene using a large strain thermally coupled constitutive model. Journal of Materials Processing Technology, **213**, 1588–1600 (2013). DOI: 10.1016/j.jmatprotec.2013.02.001

[4] Sutton M. A., Orteu J., Schreier H.: Image correlation for shape, motion and deformation measurements: Basic concepts, theory and applications. Springer, New York (2009).

[5] Van Mieghem B., Lava P., Debruyne D., van Bael A., Ivens J.: Digital image correlation for on-line wall thickness measurements in thick gauge thermoforming. Key Engineering Materials, **554–557**, 1583–1591 (2013). DOI: 10.4028/www.scientific.net/KEM.554-557.1583

[6] Seefried A., Drummer D.: The effects of radiation cross-linking and process parameters on the behavior of polyamide 12 in vacuum thermoforming. Polymer Engineering and Science, **52**, 884–892 (2012). DOI: 10.1002/pen.22155

[7] Craig S.: Direct digital UV imaging for deep draw thermoforming. Thermoforming Quarterly, **32**, 24–26 (2013).

[8] Lava P., Cooreman S., Coppieters S., De Strycker M., Debruyne D.: Assessment of measuring errors in DIC using deformation fields generated by plastic FEA. Optics and Lasers in Engineering, **47**, 747–753 (2009). DOI: 10.1016/j.optlaseng.2009.03.007

[9] Pan B., Qian K., Xie H., Asundi A.: Two-dimensional digital image correlation for in-plane displacement and strain measurement: A review. Measurement Science and Technology, **20**, 062001/1–062001/17 (2009). DOI: 10.1088/0957-0233/20/6/062001

[10] Reu P. L.: Experimental and numerical methods for exact subpixel shifting. Experimental Mechanics, **51**, 443–452 (2011). DOI: 10.1007/s11340-010-9417-4

[11] Bernstein B., Kearsley E. A., Zapas L. J.: A study of stress relaxation with finite strain. Journal of Rheology, **7**, 391–410 (1963). DOI: 10.1122/1.548963

[12] Van Mieghem B., Van Bael A., Ivens J.: Impact assessment of extrusion anisotropy on quality of thermoformed products. in 'Proceedings of Composites Week @ Leuven and TexComp-11 Conference, Leuven, Belgium', 1–8 (2013).

[13] Kaye A.: Non-Newtonian flow in incompressible fluids. College of Aeronautics, Cranfield (1962).

[14] Williams M. L., Landel R. F., Ferry J. D.: The temperature dependence of relaxation mechanisms in amorphous polymers and other glass-forming liquids. Journal of the American Chemical Society, **77**, 3701–3707 (1955). DOI: 10.1021/ja01619a008

[15] Throne J. L.: Technology of thermoforming. Hanser, Munich (1996).

[16] Li Y., Nemes J. A., Derdouri A. A.: Membrane inflation of polymeric materials: Experiments and finite element simulations. Polymer Engineering and Science, **41**, 1399–1412 (2001). DOI: 10.1002/pen.10840

[17] Wagner M. H.: Analysis of time-dependent non-linear stress-growth data for shear and elongational flow of a low-density branched polyethylene melt. Rheologica Acta, **15**, 136–142 (1976). DOI: 10.1007/BF01517505

[18] Wagner M. H., Demarmels A.: A constitutive analysis of extensional flows of polyisobutylene. Journal of Rheology, **34**, 943–958 (1990). DOI: 10.1122/1.550107

eXPRESS Polymer Letters Vol.9, No.2 (2015) 129–142
Available online at www.expresspolymlett.com
DOI: 10.3144/expresspolymlett.2015.14

An evaluation of the reproducibility of capacitive sensor based in-plane permeability measurements: A benchmarking study

H. Grössing[1*], *D. Becker*[3], *S. Kaufmann*[1], *R. Schledjewski*[1,2], *P. Mitschang*[3]

[1]Christian Doppler Laboratory for High Efficient Composite Processing, Montanuniversität Leoben, Otto Glöckl-Straße 2, 8700 Leoben, Austria
[2]Chair in Processing of Composites, Department Polymer Engineering and Science, Montanuniversität Leoben, Otto Glöckl-Straße 2, 8700 Leoben, Austria
[3]Institut für Verbundwerkstoffe GmbH, Erwin-Schrödinger-Straße, Gebäude 58, 67663 Kaiserslautern, Germany

Received 17 July 2014; accepted in revised form 27 September 2014

Abstract. A benchmark study for permeability measurement is presented. In the past studies of other research groups which focused on the reproducibility of 1D-permeability measurements showed high standard deviations of the gained permeability values (25%), even though a defined test rig with required specifications was used. Within this study, the reproducibility of capacitive in-plane permeability testing system measurements was benchmarked by comparing results of two research sites using this technology. The reproducibility was compared by using a glass fibre woven textile and carbon fibre non crimped fabric (NCF). These two material types were taken into consideration due to the different electrical properties of glass and carbon with respect to dielectric capacitive sensors of the permeability measurement systems. In order to determine the unsaturated permeability characteristics as function of fibre volume content the measurements were executed at three different fibre volume contents including five repetitions. It was found that the stability and reproducibility of the presented in-plane permeability measurement system is very good in the case of the glass fibre woven textiles. This is true for the comparison of the repetition measurements as well as for the comparison between the two different permeameters. These positive results were confirmed by a comparison to permeability values of the same textile gained with an older generation permeameter applying the same measurement technology.
Also it was shown, that a correct determination of the grammage and the material density are crucial for correct correlation of measured permeability values and fibre volume contents.

Keywords: *polymer composites, reinforcements, processing technologies*

1. Introduction

Liquid Composite Moulding (LCM) techniques, such as the resin transfer moulding (RTM), the vacuum assisted resin infusion (VARI) or the vacuum assisted resin transfer moulding (VARTM) process, are composite manufacturing processes which become very popular these days. Especially RTM is in the focus of interests of a variety of industries, such as aerospace, automotive, transport as well as sports and recreation, because they enable the ability to manufacture large fibre reinforced polymer composite (FRPC) parts of complex shape [1]. Even if the reproducibility of quality is comparably high and the cycle times are relatively low, these are still major issues for further process developments. One of the main advantages using RTM preforms is the opportunity to use a tailored stack of near-net shaped fibre reinforcements. Fibre preforms consist of tech-

*Corresponding author, e-mail: harald.groessing@unileoben.ac.at

nical textiles, such as woven or non-crimp fabric structures, or three dimensional weaves and are constructed with glass or carbon fibres [2]. Nowadays the fibre orientation (preforming) and impregnation are two independent steps of engineering. The reinforcement used for the RTM preform are in a dry state to orientate the fibres in the load specific directions. In the next step, the preform is saturated during the RTM [3, 4]. The matrix in its liquid state, a mixture of a polymeric resin and hardener, is injected into the mould via line or point gates. The injected resin system replaces the air between and in the fibre bundles of the dry reinforcing structure [5]. An important requirement during the development of a new RTM mould is the ability to predict the flow behaviour of the resin during the mould filling phase. A number of flow variables are known which have a direct impact on the mould and process design. For components with an increased geometrical complexity those can only be realistically predicted by using a numerical filling simulation. In order to achieve the best FRP-part quality, a completely filled mould and a totally saturated preform are mandatory. In order to have a full wetted preform the position of the resin injection points and air vents must be well-placed. Currently, attempts are made to substitute the very expensive trial-and-error procedures by flow modelling tools. Numerical filling simulations support the engineers in optimizing the tool design and predicting the mould filling time. Thus, the numerical mould filling simulation tools are important and supporting tools for the advancement of the RTM process [6–10].

An accurate simulation set-up needs reliable input parameters of the time- and curing degree dependent resin viscosity, the preform porosity and the porosity–dependent preform permeability. The permeability behaviour of the textile preform is directly related to the impregnation and filling time [7, 8, 11]. The transmissibility of a porous media, in this case the fibre preform, to liquid flow is described with the term permeability. The common empirical law on fluid flow through porous media was published by Henry Darcy in 1856 [12]. Henry Darcy's law is a general accepted Equation (1) for the description of the one dimensional flow through a porous media:

$$v_x = -\frac{K_x}{\eta}\frac{\Delta p}{\Delta x} \quad (1)$$

where the superficial velocity of the 1D flow is v_x [m/s], K_x [m²] represents the permeability value of the measured preform direction, η [Pa·s] the fluid viscosity of the injected fluid and the term $\Delta p/\Delta x$ [Pa/m] expresses the pressure drop to a specific flow length. Three different kinds of experimental methods of permeability measurements are well-known: 1D flow [13–16], 2D flow [13, 17, 18] and 3D flow [19–22]. Nowadays no defined standard requirements for permeability measurements and calculation procedures are available [23–25]. In the study of Vernet *et al*. [16] there is a description of a way to standardize 1D permeability measurements.

The main aim of this study is the comparison of two identically manufactured dielectric capacitive based in-plane permeability measurement systems located and supervised at two different research sites:

– Lehrstuhl für Verarbeitung von Verbundwerkstoffen (LVV), Leoben, Austria and the
– Institut für Verbundwerkstoffe (IVW) GmbH, Kaiserslautern, Germany.

Despite the fact that the two systems are technically equal, there are several issues which can cause deviations between measurement results. These are:

– systematic differences between the measurement systems and their calibration – a technology sensitive to this issue is not suitable for a standardised permeability measurement
– variation concerning the usage of the possibility for manual interventions in data capturing (e.g. experiment time) and data analysis (e.g. evaluation range)
– differences during sample preparation, storage and handling

Therefore, it is the target of this study to prove that the used system allows a reproducible measurement in spite of these barriers. This proof is a main necessity for the broad acceptance of a system e.g. in serial production for material selection, process design and incoming goods control.

Two different commercially available materials which are typical for industrial customers are used for the comparison measurements. A glass fibre woven textile and a carbon fibre biaxial non-crimped fabric (NCF) are investigated. A comparison of measurements executed at both laboratories should allow an estimation, of the suitability of the measurement methodology for reproducible permeability measurement. Accordingly, the accuracy and

the reliability of the used permeability measurement system will be examined.

2. Review on permeability measurement techniques, benchmark studies and statistical analysis

Literature depicts different methods and systems for permeability measurements as well as for permeability benchmark studies. Diverse references [13–18] are describing 1D and 2D measurement approaches which are able to sense the flow front as a function of time for in-plane permeability calculation. The fact that there are no standardized requirements for permeability measurement systems and no uniform calculation algorithms, permeability values measured in different research labs are differing. This is the reason why institutes and labs performed benchmark studies in the past. Also, the uncertainty of measurements and test rigs were investigated because of the stochastic and statistical influence.

2.1. Permeability measurement techniques

1D permeability measurement

Using 1D permeability measurement setup means that the permeability behaviour is measured in one specific direction. The saturated and unsaturated flow methods can be distinguished in order to predict the preform permeability. During the saturated 1D flow experiment a test fluid continuously flows through the fabric which is placed and compacted in a mould. The steady-state relationship between the fluid flow and the pressure drop across the whole length of the mould [26–28] is measured. For an unsaturated permeability test a dry fibre preform is used. The air which is in the fibre based material is replaced by the liquid medium [26, 28, 29] during the measurement and the flow front is tracked. A number of errors are related with this relatively simple test apparatus. First of all, there are errors, which are caused by small gaps with increased permeability between the preform edges and the mould walls which are referred to as 'Race tracking' [2, 9] or 'edge effect' [30, 31]. Another disadvantage of the 1D test is the fact that three 1D measurements have to be executed for the full description of the in plane permeability tensor since three unknown variables have to be defined. The two perpendicular main directions of the flow and the orientation angle of the main directions with respect to the reference axis. Further problems arise from mould deflections and unsaturated spots [29]. The aim of an international benchmark study [16] was to eliminate the edge effects and errors by using a defined measurement method on each research lab.

2D permeability measurement

In case of an anisotropic material an ellipse occurs during commonly used centre point injection. The determination of the preform permeability values and the orientation angle of the occurring ellipse to a reference axis are still challenging problems from experimental and theoretical points of view. The knowledge about the timely flow front advancement is the most important fact for an accurate permeability calculation [32–37]. In order to calculate the permeability values of the investigated preform, the major and minor axis lengths of the occurring ellipse are needed. They are needed to determine the corresponding highest (K1) and lowest (K2) in-plane permeability values with a mathematical algorithm after having executed the permeability measurement. Adams and coworkers [32–35] and Chang and Hwang [36] are describing two different and independent algorithms for in-plane permeability calculation. Anisotropy α is a coefficient which describes the relationship between the major and minor axis permeability. The anisotropy coefficient is defined as the quotient of K2 and K1 [32, 36, 37].

For the in-plane permeability measurements different permeability test rigs are described in the literature. On the one side there are test rigs which are using sensors for flow front detection during the fluid injection. These sensors are embedded in metal mould halves [6, 17, 24, 29]. On the other side there are systems with a visual aid – a camera system – and a transparent upper mould half tool for flow front tracking exist [13, 38, 39]. Both show specific advantages and disadvantages. Mainly, the embedded mould sensors allow usage in a rigid steel mould which makes the system more insensitive against possible deflections. On the other side, transparent moulds allow a more exact skin flow front detection.

2.2. Benchmark studies

Literature depicts numerous studies for the comparison of different permeability measurement systems and methods as well as numerical error and statistical uncertainty analysis.

In order to investigate the comparability of permeability measurements on different systems Lundström *et al*. [13] executed permeability measurements at three different institutes with the same magnitude of materials. In this round robin study saturated and unsaturated 1D permeability tests, as well as 2D permeability tests were performed. The results showed a good reproducibility and a standard deviation between 10 and 30% between the institutes. The unsaturated 1D flow tests showed the best repeatability in the results with a standard deviation of 8.5 respectively 15%. It should also be pointed out here that the measured permeability values are increasing from the 2D method compared to the saturated 1D- and the 1D unsaturated flow techniques. Comparisons between the institutes and the same measurement method as well as between the 1D and 2D method showed a reproducibility of the results within the range of every single measurement method. They also obtained that there is no significant difference between saturated and unsaturated permeability. However, in a literature review performed by Dungan and Sastry [40] it was found, that the relation of saturated to unsaturated permeability can range from 1/4 to 4.

In the first international benchmark exercise Arbter *et al*. [41] accomplished permeability measurements on 11 institutes using 16 different measurement systems. Saturated and unsaturated 1D test rigs as well as 2D permeameters were used in these studies. The comparison of the results of the permeability measurements with the 16 different systems showed deviations in the range of an order of magnitude. The standard deviation of the permeability characteristics determined in this benchmark was about 1.000%. Also the calculated anisotropy coefficient alternates by a factor of two between the different systems. In the second round the participants of the international benchmark study [16] used a standard RTM mould with an acrylic or a glass plate as upper mould half tool for executing the 1D permeability measurements. In order to avoid leakage during the fluid injection, a sealing rubber was positioned between the lower and upper mould half tool. The sample size was also an identified parameter that was chosen for the second measurement round. All preforms used for permeability measurements were larger than the representative elementary volume of the fabric. This was taken into account to eliminate the stochastic non-uniformity of the weaving pattern. Also the fibre volume content was fixed with 45%. Other process parameters like the injection pressure (1 bar) and the test fluid (silicon oil) were set in order to eliminate their effect on the fluctuation on the determined data. The standard deviation of the permeability characteristics determined in second round of the international benchmark was below 25%.

In both mentioned round robin studies nearly the same main sources of errors were pointed out: The accuracy of the measurement of the physical quantities, errors in cavity dimensions, changes in cavity dimensions during measurements, influences from the used liquid and the aberration of the values used for the permeability calculation algorithm. In addition the deviation of the used textile properties, the batch quality, the deviance in fibre orientation, the distance between the rovings and the differences in areal weight had an influence on the permeability calculation results. The influence of material in homogeneities are higher to assess than the experimental errors [13, 41].

2.3. Statistical analysis

Pan *et al*. [42] conducted a statistical investigation of 1D permeability measurements of woven and knitted fabrics in order to predict significant statistical influences on permeability measurements. In this study race tracking near the mould walls, variations in the areal weight and deformation effects of the measured textile using a two part tool were found to be influencing factors on the permeability. On the other side the measurement results are not affected by the experience of the executing person.

Endruweit and coworkers [43–46] performed numerical and experimental analysis dealing with the deviation of geometrical parameters of technical textiles and their influencing factors on the permeability. The experimental error for their specific test case, including the estimation of parameters which are dependent on the process like injection pressure, flow front velocities, porosity and fluid viscosity, sums up to a maximum of 14%. Accordingly, all variations which are above this error margin are related to the textile properties. As this is the case a unit cell based on a non-crimp fabric (NCF) was developed. Rovings with an elliptical shape were supposed and parameters for the major axis diameter (roving width) and the roving distances were considered for the variation of the geometrical

parameters. Both factors are determining the variation of the fibre orientation angle, which increases with the decreasing quotient of roving width and roving distance. The variation of the fibre angle by using woven fabrics is assigned by available gaps between the rovings and the stitching seams by utilizing NCF's. These parameters were implemented in the numerical model and were statistically varied. Afterwards the results were compared to optical permeability measurements. The experimental results showed a trend to the normal curve of distribution and to the standard deviation of 9 to 29%. The higher the ratio of roving width to the roving distances, the lower was the local permeability variation and the more similar was the real flow front shape to an ideal ellipse. With the variation of the local permeability the global permeability was decreasing too but the global permeability was decreasing with increasing ratio of roving width to roving distances. This was explained by considering the global textile. In case of high local deviations the consideration of the global textile behaviour gets more uniform due to compensational effects. The numerical developed model showed results in the same range as monitored during the experimental permeability characterization. But it has to be mentioned that effects like nesting, which are important for high roving distances and higher fibre volume contents, were not taken into account.

Fauster *et al*. [47] addressed their scientific work to statistical analysis of material and process parameters in order to predict the error of measurement of an optical permeameter. An analytical approach based on the law of error propagation first order as well as the Monte-Carlo simulation was used in this study. The results supply a good agreement. The considered parameters were the major and minor axis length of the occurred ellipse, the viscosity of the fluid, the injection pressure, the injection radius in the middle of the preform to eliminate the through thickness impregnation, the cavity high as well as material parameters like the fibre density and the areal weight. The supposed exactness of the measurements for the major and minor axis length of the detected ellipse were 0.1%, for the fibre density 0.25% and for of the areal weight 5%. The assumptions of the variance of the results were theoretically determined with 1%. In addition both models calculated a variation of 8% for K1 and K2.

Due to the high standard deviations during permeability measurements Morren *et al*. [25] developed a solid epoxy test specimen as a reference sample for permeability measurements. The specimen was produced with a stereo lithography technique. This porous structure has the same main features as real fibre textiles. It has the same order of degree of the pore sizes and a similar interconnectivity and tortuosity of the pores. Using this test specimen for permeability measurements a standard deviation of less than 5% was reached.

In summary it can be seen that the results of permeability measurements are differing between the used permeability measurement methods (1D and 2D), but there are also inherent differences given when using the same method. This is attributed to the differences of the mechanical design and the used techniques as well as to experimental errors and variations of the textile properties. In respect to the determination of accurate and comparable permeability values and the prediction of reliable process conditions, a minimization of the material property variation, the acquisition and analysis of the special features of each single measurement system as well as the basic understanding of the geometrical variations according to the permeability characteristics are necessary. It is also very important to know, that the statistical uncertainty of material and process parameters are affecting the calculated permeability coefficients with an uncertainty of 8% [16, 41–47].

3. Experimental set-up, materials and approach

3.1. Experimental set-up: 2D permeability measurement system

The bases of the study were two similar 2D in-plane permeability measurement systems which apply capacitive sensor technology for flow front tracking. The methodology was developed and patented by the IVW [48]. The current system '2-D-Capa-Perm' of the IVW states the third generation including changes in sensor positioning and number, sensor and peripheral electronics, sensor coating and data capturing and processing software. The company Präzisonsmaschinenbau Bobertag (PMB) GmbH built up the system for the LVV in 2013. Both systems are equal concerning the sensor arrangement. A cavity geometry of 480 by 480 mm^2 is resulting due to the sensor lengths. The sensors

are embedded in the lower mould half and the cavity high is locally not affected by the sensors. Two different sensor lengths are used. The sensor length for the east (E) and west (W) direction are 185 mm and the sensors for the other six directions have a length of 105 mm. The sensitive width of all eight sensors is 5 mm. They comprise eight actinoid positioned dielectric capacitive sensors as schematically illustrated in Figure 1.

In the upper mould a central injection point is given which results in a radial or elliptical flow, depending on the isotropy respectively anisotropy of the flow behaviour. The flow front is quasi-continuously tracked by the capacitive sensors. The dielectric properties of the inserted fibre structure inside the mould change due to increasing saturation [49]. The sensors capture the change of capacitive equivalent which represents the dielectric properties of the fibre structure lying above their sensitive area. Knowing the capacitive equivalent of the sensor when covered by dry respectively fully saturated textile, allows the derivation of the flow front position on the sensor out of the development of the sensor´s capacitive equivalent over time. The correlation of flow front position and level of saturation is linear. Since eight sensors are given, at each point of experiment time, eight coordinates of the flow front are available. The elliptic equation of a perfectly point-symmetric ellipse can be defined by only three coordinates. However, if only three sensors are given, it is not possible to make a statement about the deviation of the true flow front from the assumption of the ideally point-symmetrical ellipse. With the eight sensors, it can be analyzed how well the assumption fits, which is also an indicator for how accurate the permeability calculation can be. Furthermore, this offers the possibility of statements on the material homogeneity, e.g. by comparing the flow front progression on opposing sensors. The 8-sensor system allows an averaging of opposing sensors which minimizes the sensitivity for local material inhomogeneities, while the information about these inhomogeneities is not lost.

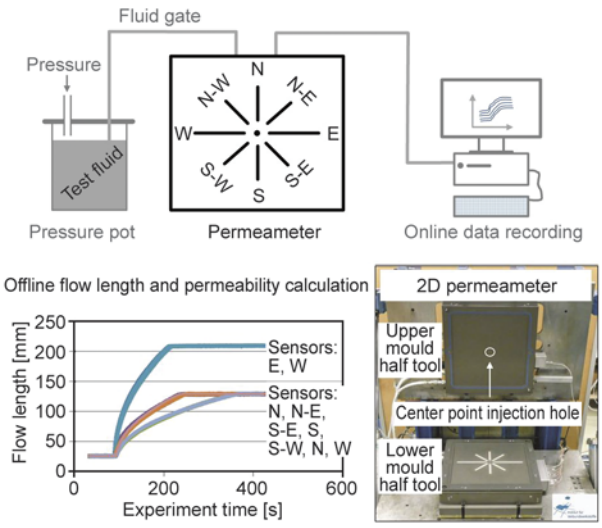

Figure 1. Schematic overview of the used sensor arrangement, the offline analysis and the permeability measurement set-up

Out of the elliptic equation, the calculation of length and orientation of the half-axes is possible. This is done for every time step. According to Adams *et al*. [34] to the fluid motion can be described by the continuity equation for incompressible flow by Equation (2) and Darcy's law in the tensorial form by Equation (3):

$$\nabla \cdot v_0 = 0 \tag{2}$$

$$v_0 = -\frac{k \cdot \nabla p}{\eta} \tag{3}$$

thereby, v_0 is the superficial velocity which is the product of flow front velocity and porosity. Correspondingly, besides the flow front movement also the pressure drop and the viscosity have to be known. Assuming the pressure at the flow front to be atmospheric the pressure drop equals the set injection pressure (gauge). The temperature-based viscosity was preliminarily measured and the fluid injection temperature is measured online. Based on this data the calculation of the permeability is possible using the methodology presented by Adams and coworkers [32–35].

Several different cavity heights between 1.45 and 8 mm can be realized by highly accurate steel frames. By varying the cavity height and the number of layers numerous different fibre volume contents can be set. Both measurement systems are arranged on mould carriers. A schematic representation of the permeability measurement method, the offline flow front length calculation and on the used test rig are given in Figure 1.

The software used for the calculation of the permeability out of the captured sensor data was the same at both research sites.

Table 1. Material data of the used reinforcements for 2D permeability determination

Material	Fabric type	Fibre material	Grammage
Hexcel 1102	Woven fabric, 2/2 twill weave, balanced	Glass fibre	290 g/m^2
Saertex X-C	Non crimp fabric, Biaxial, ±45°	Carbon fibre	588 g/m^2

3.2. Materials and sample preparation

The measurements have been executed with two dual-scale textiles differing concerning the material type, the fibre material and the grammage. Their characteristics are listed in Table 1.

In order to minimize effects of sample preparation on the results of the comparison, the preforms used for the measurement series were manufactured uniformly in one laboratory (Leoben, Austria). They were directly stacked to the intended final number of layers and cut using a CNC cutter. Subsequently, they were transferred to the IVW. The preform geometry was square shaped with an edge length of 465 by 465 mm^2. In order to ensure a vertically straight flow front an injection hole of 13 mm diameter was cut out in the middle of the preform providing a flow channel through the thickness. Before every single measurement the preforms were weighed on a scale to evaluate the material inhomogeneity. As a test fluid rape seed oil was used. The viscosity-temperature characteristics were determined separately in each lab using an Anton Paar couette- respectively a Brookfield spindle rheometer under standardized lab conditions.

3.3. Approach

In order to evaluate the reproducibility of the results, the permeability at three different fibre volume contents was measured independently at both research sites. This allows the interpolation of the data based on data iteration with an exponential function, which allows a very good accordance to the actual measurement data. Thus, it was possible to use the same number of layers at both research sites, even if the cavity heights weren't exactly equal. Changing the number of layers can have an influence on the results even if the influence is small [50, 51].

The industry asks for reliable results which are acceptable within the repeat tests. Due to the high material costs and the measurement expenditure the measurement series should be kept to a minimum. Therefore at each fibre volume content five measurements with five preforms were performed for statistical coverage. Deviation between the single measurements gives indication about material homogeneity and measurement errors.

At first the measurement results of both institutes were directly compared, without any instruction for determination of analysis parameters. Subsequently single parameters were varied in order to estimate their influence on the reproducibility.

These parameters were:

– Time frame for permeability calculation
– Grammage of samples (individually weighed vs. averaged)

As mentioned, the permeability calculation is possible using different sensor triplets. The sensors are denoted by cardinal directions (Figure 1). Within the presented study the opposing sensors were averaged. Then the permeability was independently calculated based on the triplet (N/S, N-E/S-W, E/W) and (N/S, N-W/S-E, E/W). The resulting permeability values and orientation angles are then also averaged.

The presented work focused on the empirical determination of in-plane permeability values with two similar permeability measurement systems. The instrument errors, the error propagation as well as the human influence during sample preparation and through measurement execution were not taken into consideration.

4. Results and discussion

4.1. Independent data analysis at LVV and IVW

Figure 2 shows the comparison of the results gained at both research sites for the glass fibre woven textiles. The time frame for analysis was independently set and the viscosity curve corresponded to the different measurement liquids used. As can be seen in the diagram of Figure 2 the data is in very good agreement. The diagram shows the permeability over the fibre volume content which corresponds to 1-porosity. Thus, increasing fibre volume content states a decreasing pore space available for flow, which decreases permeability. The minimum and maximum deviations are at 1.6 and 4.98% respectively. The chosen material perfectly suits the require-

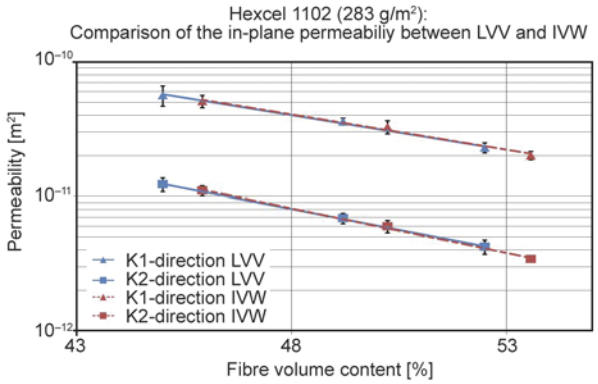

Figure 2. Comparison of the in-plane permeability values for the glass fibre woven textile independently calculated at IVW and LVV

ments for a comparison, since the variation coefficient is comparably low (between 4.52 and 17.28%) in the light of the huge amount of materials which have been investigated at both research sites (e.g. [50]). Thus the deviation between the LVV and the IVW results is smaller than the standard deviation between the repetition measurements.

Besides the comparison between IVW and LVV the IVW results were also compared to results gained during a previous study at the institute. Rieber [50] has investigated the same material at equal cavity heights – number of layers combinations. However, it was a different batch of the material and the grammage has slightly changed in the data which results in differing fibre volume contents. Also, the system '2D-COMP' was used, which states the 2nd generation in-plane permeameter and thus the predecessor of the currently used system. The comparison is shown in Figure 3, where again the permeability is shown over the fibre volume content. Again, the deviation between the results is smaller than the standard deviation. The similarity of the results shows the homogeneity of the chosen mate-

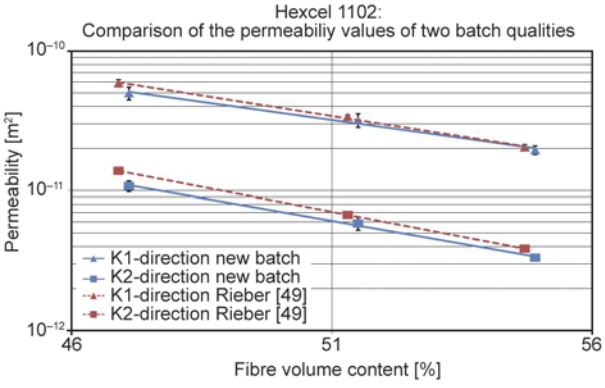

Figure 3. Comparison of IVW results with results from Rieber [50]

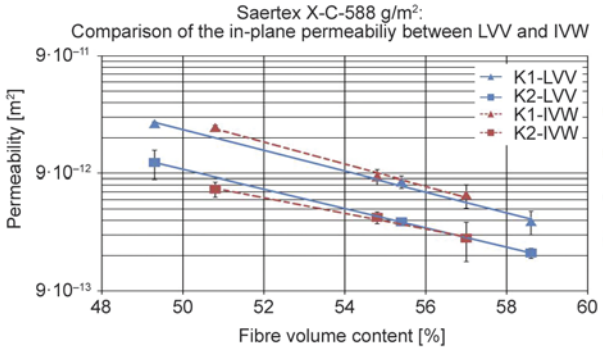

Figure 4. Comparison of the permeability values for the carbon fibre NCF independently determined at IVW and LVV

rial, but also the high reproducibility of the measurement with the capacitive technology.

The comparison of the results for the carbon fibre non-crimp fabric showed higher deviations. The results are shown in Figure 4. However, the permeability values show good accordance.

The minimum and maximum calculated standard deviations are 3.66 and 22.77% for K1 and 4.16 and 41.00% for K2. The comparison of both research sites showed that there is an average difference of 3.77% for the permeability of the major and 30.05% for the permeability of the minor axis. In the diagram shown in Figure 4 it can be seen that the anisotropy is higher for the IVW values, which leads to comparably higher K1-values, while the K2 values are comparably lower. Such anisotropy can be caused e.g. when during handling the crimp, which results from the differences in the weft and warp yarn tension during manufacturing, is changed. However, since only one fibre volume content is affected, no in-depth interpretation is meaningful, since the data base is rather small.

4.2. Variation of evaluation time range

The influence of the time range on the evaluation is an indicator for the homogeneity of the material. If the material is perfectly homogenous, it should not make an influence which time range is chosen for permeability calculation, as long as all used sensors are in a valid area (overflow started but not finished). The valid area is illustrated in Figure 5 where the metric flow data as a function of experiment time is shown for each sensor, which allows the calculation of the flow front ellipses. As can be seen, the curve growth is very homogeneous. Due to the faster velocity of the flow front advancement in the East and West direction the slopes of the curves

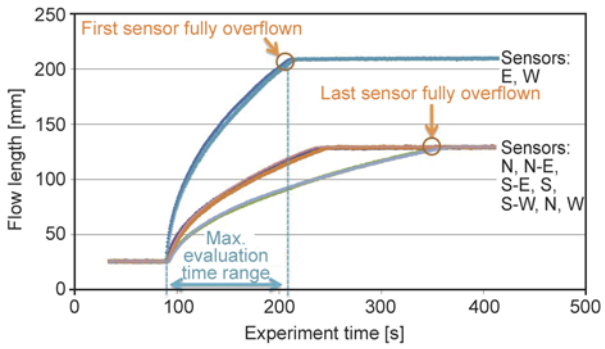

Figure 5. Flow distance over time calculated from each sensor data by using the glass fibre woven textile

have a stronger dependence on the experiment time. The flow front propagation during the permeability measurement is less dependent on the experiment time in the other six directions. That means that the anisotropy of the investigated textile is very high. Due to the fact that the sensors are located 25 mm away from the injection point the maximum detectable flow length increases from the sensor lengths. Thus, the maximum detectable flow lengths are an addition of the distance between the injection point to the sensitive area of the sensor and the sensitive area of the sensors itself. The maximum detectable flow lengths are 210 mm for the east (E) as well as the west (W) sensor and 130 mm for the north (N), the south (S), the north-east (N-E), the south-east (S-E), the south-west (S-W) and the north-west (N-W) sensors. The maximum end time for the analysis – if all sensors are taken into account – is the time point at which the first sensor is fully overflown. Using very inhomogeneous material, the curve of the flow length over the experiment time may be less smooth and show several humps. In this case the automatic detection of the status of full sensor coverage by fluid might catch the wrong hump. In this case a manual correction is possible.

In order to quantify the influence of the evaluation time range, 10 s were manually added to respectively subtracted from the value automatically set for end time and the permeability was recalculated. For the GF-textile, which showed even smoother curves, a change between 0.02 und 0.19% was measured for K1, and a change between 0.10 and 0.13% was measured for K2. The initial evaluation time range was 120 s. For both, the glass fibre and carbon fibre textile, the time range was set individual on each research side. This reflects the measurement stability and the material homogeneity. For the CF-textile a change between –6.09 und +5.59% was measured for K1, and a change between –6.96 and 6.89% was measured for K2. The initial evaluation time range was about 280 s. Considering the results of both textiles it can be seen that a change of the evaluation time range has a higher influence on the CF-textile. The reason for this high impact can be explained with the electric properties of the CF and the used sensors. In some cases of measuring CF-textiles it is very difficult to determine the point on which the sensor is fully overflown because the sensor and the CF have an electrical interaction. This interaction at the end of the sensor can be termed as 'sensor creepage'. Thus, the sensor creepage is responsible for the higher deviation if the evaluation time range is changed as well as for the determination of the experiment end.

4.3. Variation of grammage values

As can be seen by the results shown in the previous sections, the influence of the fibre volume fraction on the permeability is very high. Thus, besides an accurate measurement it is also important to correlate the measured value to the right fibre volume fraction. Otherwise the exploitation of the results, e.g. for a numerical filling simulation, will be highly corrupted. Accordingly, in this section is shown, how important the correct definition and determination of the fibre volume content is. Thus their influence on the presented comparison was investigated. Three basic alternatives were examined:

1. Assume the grammage on the data sheet for each measurement
2. Measure the weight of all samples and assume all samples to have the average value
3. Directly account the measured value to the samples

Each option goes together with its advantages and disadvantages. Generally it has to be questioned where grammage deviation between the samples can arise from. Often it is caused by a fringe out at the edges of the sample. In this case it is not very meaningful to account the individual weight to each sample because the grammage in the area relevant for measurement is not affected by the fringe out. On the other side most manufacturers state a possible variation of ±5% which causes huge deviation concerning the fibre volume content. Thus the first option is also not always appropriate. Therefore, the most target-aimed option seems to be to average the weight of all samples. However, knowing the indi-

vidual weight of each sample can help to explain permeability deviations. In the case of the carbon fibre fabric the average grammage was 580.71 g/m^2 (min: 580,40 g/m^2, max: 581.07 g/m^2) while the data sheet stated 588 g/m^2. The resulting difference in fibre volume content can be a main error source for example for flow simulation. The permeability as a function of fibre volume content is one of the most important inputs in the flow simulation. False assumptions concerning the grammage lead to a horizontal shift of the curves. Due to the strong decreasing influence of the fibre volume content on the permeability such an error is as highly unfavourable as an error concerning the measurement itself. It can be concluded, that the influence of grammage variation on the permeability is huge. Thus, when simulating the filling process it should be taken into account that the grammage can vary (e.g. by the 5% stated in the data sheet). A possible solution would be best and worst case simulations based on the minimum and maximum permeability possible.

Grammage is only one side of the problem, when calculating the fibre respectively the pore volume fraction. Figure 6 shows the influence of the grammage on the in-plane permeability calculation.

In order to calculate the fibre volume content out of the areal weight the material density has to be known. For the glass fibre woven material the density of glass is sufficient. In the carbon fibre NCF an additional polyester stitching yarn (PSY) is present. Thus, it has to be decided which density value is to be used. The differences are exemplarily shown in Figure 7. In the first case the pore volume content was calculated taking the PSY into account but assuming it to have the same density as the carbon fibre. In the second case the individual material densities were used. It would also be possible to calculate an effective material density weighted by the respective contributions to the total areal weight of the material. The resulting pore volume fraction would be the same as for the second case. The difference is about two to three percentage points. Regarding the decrease of permeability which is usually caused by such a reduction of pore space, this points out the importance of correct or at least consequent pore space calculation.

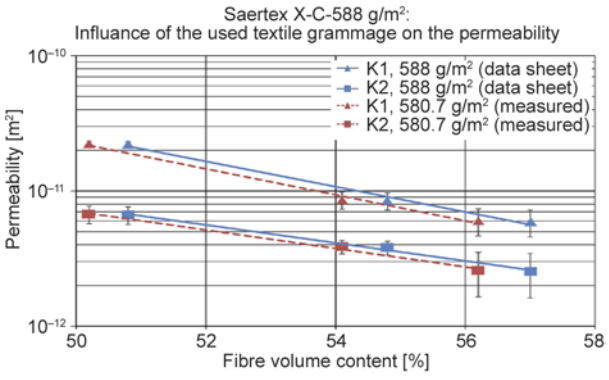

Figure 6. Influence of the used CF NCF textile grammage on the in-plane permeability values

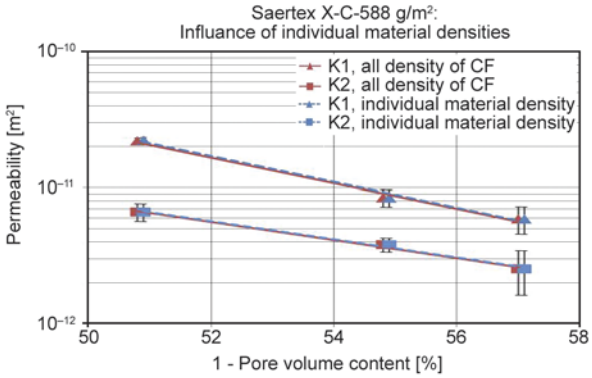

Figure 7. Influence of different approaches for grammage calculation for carbon fibre NCF

Other influencing factors on the permeability of textiles could be the filament type, the filament shape and the filament diameter. Rieber [50] showed that the influence of the filament diameter can influence the in-plane permeability values by 10% using 6 and 9 µm thick filaments. Summerscales [52] refers in his work to the studies of Gurton. Gurton reports that the impregnability of a yarn with 50% fibre volume content is three times higher by using a 15 µm filament diameter compared to a yarn with 5 µm filament diameter.

The determined values for the permeability of the major and minor axis as well as the orientation angle are listed in Table 2 (glass fibre woven textile) and Table 3 (carbon fibre NCF). The orientation angle refers to the direction of the highest in-plane permeability K1 related to the production direction of the material (0°). Since both materials are not purposely sheared the permeability main axes should coincide with the material axes. Thus, the orientation angle should be 0°. As can be seen slight deviations from are given, which can be caused by material inhomogeneities, unintended shearing during handling, and deviations of the real flow front from the assumed ideally point-symmetrical ellipse. Considering the orientation angle detected at the IVW for the CF NCF at a FVC of 54.80% it can be seen that

Table 2. Major and minor axis permeability values for the glass fibre woven textile

Laboratory	FVC [%]	K1		K2		Orientation angle	
		Average [m²]	Deviation [%]	Average [m²]	Deviation [%]	Average [°]	Deviation [°]
LVV	46.10	$5.53 \cdot 10^{-11}$	17.28	$1.20 \cdot 10^{-11}$	11.70	1.40	±2.54
	50.40	$3.51 \cdot 10^{-11}$	5.95	$6.73 \cdot 10^{-12}$	8.85	0.80	±2.16
	53.80	$2.97 \cdot 10^{-11}$	8.63	$5.48 \cdot 10^{-12}$	12.13	1.40	±1.45
IVW	47.10	$4.98 \cdot 10^{-11}$	10,60	$1,08 \cdot 10^{-11}$	8.68	0.96	±1.13
	51.50	$3.19 \cdot 10^{-11}$	11.20	$5.85 \cdot 10^{-12}$	10.62	0.04	±0.63
	54.90	$1.95 \cdot 10^{-11}$	7.20	$3.33 \cdot 10^{-12}$	4.52	1.08	±0.92

Table 3. Major and minor axis permeability values for the carbon fibre NCF

Laboratory	FVC [%]	K1		K2		Orientation angle	
		Average [m²]	Deviation [%]	Average [m²]	Deviation [%]	Average [°]	Deviation [°]
LVV	49.30	$2.37 \cdot 10^{-11}$	3.66	$1.11 \cdot 10^{-11}$	27.61	3.06	±1.59
	55.40	$7.62 \cdot 10^{-12}$	11.64	$3.49 \cdot 10^{-12}$	4.61	3.83	±3.83
	58.60	$3.50 \cdot 10^{-12}$	22.77	$1.89 \cdot 10^{-12}$	9.83	7.09	±7.53
IVW	50.80	$2.20 \cdot 10^{-11}$	4.97	$6.64 \cdot 10^{-12}$	14.87	0.02	±7.40
	54.80	$8.43 \cdot 10^{-12}$	14.51	$3.81 \cdot 10^{-12}$	11.69	–3.19	±6.32
	57.00	$5.90 \cdot 10^{-12}$	22.73	$2.28 \cdot 10^{-12}$	40.97	3.53	±10.80

this value is negative. Due to the large preform size which gets saturated during the measurement, material inhomogeneity and handling as well as shearing effects it is possible to generate a negative value for the orientation angle.

5. Conclusions

In this study two similar dielectric capacitive based 2D permeability measurement systems were compared by measuring two different materials. A glass fibre woven textile and a carbon fibre based biaxial NCF were investigated at two diverse research sites. In order to eliminate the influence of sample preparation the samples were prepared in Leoben, Austria and were shipped to Kaiserslautern, Germany. The permeability measurements were executed independently of each site. The permeability results and the reproducibility of these chosen textiles gained at the two research labs are valid for the investigated material. The reproducibility and the accuracy of the permeability measurements cannot be transferred to other textiles produced with other materials, e.g. aramid or natural fibres.

The results can be summarized and are stating to the following:

– The results for the in-plane permeability values have shown a very good agreement. The deviance between the LVV and the IVW results is smaller than the standard deviation between the repetition measurements.
– A high reproducibility of permeability measurements was also reached by comparing two batch qualities to each other. The similarity of the results shows the homogeneity of the chosen material. Also the older batch was measured with a third capacity technology-based system.
– The comparison of the permeability results of the carbon fibre NCF showed higher deviations but there is also a good agreement between the two research sites.
– The in-plane permeability values are affected by the used textile grammage. The grammage is directly related to the fibre volume content which influences on the permeability calculation.
– In the case of the carbon fibre textile an additional polyester stitching yarn is present. If the carbon fibre and the polyester yarn were allocated with their true density the difference of the calculated permeabilities were two to three percentages compared to the procedure of using only the density of a carbon fibre.

It could be shown that the dielectric capacitive permeameter technology is a promising approach towards reliable and reproducible permeability measurements. The executed radial in-plane measurements show a low standard deviation and a very good reproducibility in the case of the glass fibre woven textile. It can also be noted that by using the presented technology it is possible to measure the same permeability characteristics with a very low

deviation in two different located and supervised labs.

Acknowledgements

The authors kindly acknowledge the financial support provided by both the Bundesministerium für Wirtschaft, Familie und Jugend in Austria, the Christian Doppler Laboratory and the FACC Operations GmbH.

The authors also kindly acknowledge the funding of the project 'Westaperm – Advancement and Extension of the 2D-Measurement cell for the standardized determination of the permeability of textile fibre structures' by AIF within the ZIM-program.

References

[1] Lässig R., Eisenhut M., Mathias A., Schulte R. T., Peters F., Kühmann T., Waldmann T., Begemann W.: Serienproduktion von hochfesten Faserverbundbauteilen. Perspektiven für den deutschen Maschinen-und Anlagenbau. Studie von Roland Berger Consultants (2012).

[2] Bickerton S., Advani S. G.: Characterization and modeling of race-tracking in liquidcomposite molding processes. Composites Science and Technology, **59**, 2215–2229 (1999).
DOI: 10.1016/S0266-3538(99)00077-9

[3] Weimer C., Preller T., Mitschang P., Drechsler K.: Approach to net-shape preforming using textile technologies. Part I: Edges. Composites Part A: Applied Science and Manufacturing, **31**, 1261–1268 (2000).
DOI: 10.1016/S1359-835X(00)00073-7

[4] Weimer C., Preller T., Mitschang P., Drechsler K.: Approach to net-shape preforming using textile technologies. Part II: Holes. Composites Part A: Applied Science and Manufacturing, **31**, 1269–1277 (2000).
DOI: 10.1016/S1359-835X(00)00074-9

[5] Kendall K. N., Rudd C. D., Owen M. J., Middleton V.: Characterization of the resin transfer moulding process. Composites Manufacturing, **3**, 235–249 (1992).
DOI: 10.1016/0956-7143(92)90111-7

[6] Rieber G., Jiang J., Deter C., Chen N., Mitschang P.: Influence of textile parameters on the in-plane permeability. Composites Part A: Applied Science and Manufacturing, **52**, 89–98 (2013).
DOI: 10.1016/j.compositesa.2013.05.009

[7] Verleye B., Croce R., Griebel M., Klitz M., Lomov S. V., Morren G., Sol H., Verpoest I., Roose D.: Permeability of textile reinforcements: Simulation, influence of shear and validation. Composites Science and Technology, **68**, 2804–2810 (2008).
DOI: 10.1016/j.compscitech.2008.06.010

[8] Liu X-L.: Isothermal flow simulation of liquid composite molding. Composites Part A: Applied Science and Manufacturing, **31**, 1295–1302 (2000).
DOI: 10.1016/S1359-835X(00)00007-5

[9] Steenkamer D. A., Wilkins D. J., Karbhari V. M.: The influence of preform joints on the processing of RTM composites. Composites Manufacturing, **6**, 23–34 (1995).
DOI: 10.1016/0956-7143(95)93710-2

[10] Louis M., Huber U.: Investigation of shearing effects on the permeability of woven fabrics and implementation into LCM simulation. Composites Science and Technology, **63**, 2081–2088 (2003).
DOI: 10.1016/S0266-3538(03)00111-8

[11] Grujicic M., Chittajallu K. M., Walsh S.: Non-isothermal preform infiltration during the vacuum-assisted resin transfer molding (VARTM) process. Applied Surface Science, **245**, 51–64 (2005).
DOI: 10.1016/j.apsusc.2004.09.123

[12] Darcy H.: Les fontaines publiques de la ville de Dijon. Victor Dalmont, Paris (1856).

[13] Lundström T. S., Stenberg R., Bergström R., Partanen H., Birkeland P. A.: In-plane permeability measurements: A nordic round-robin study. Composites Part A: Applied Science and Manufacturing, **31**, 29–43 (2000).
DOI: 10.1016/S1359-835X(99)00058-5

[14] Amico S., Lekakou C.: An experimental study of the permeability and capillary pressure in resin-transfer moulding. Composites Science and Technology, **61**, 1945–1959 (2001).
DOI: 10.1016/S0266-3538(01)00104-X

[15] Gebart B. R., Lidström P.: Measurement of in-plane permeability of anisotropic fiber reinforcements. Polymer Composites, **17**, 43–51 (1996).
DOI: 10.1002/pc.10589

[16] Vernet N., Ruiz E., Advani S., Alms J. B., Aubert M., Barburski M., Barari B., Beraud J. M., Berg D. C., Correia N., Danzi M., Delavière T., Dickert M., Di Fratta C., Endruweit A., Ermanni P., Francucci G., Garcia J. A., George A., Hahn C., Klunker F., Lomov S. V., Long A., Louis B., Maldonado J., Meier R., Michaud V., Perrin H., Pillai K., Rodriguez E., Trochu F., Verheyden S., Wietgrefe M., Xiong W., Zaremba S., Ziegmann G.: Experimental determination of the permeability of engineering textiles: Benchmark II. Composites Part A: Applied Science and Manufacturing, **61**, 172–184 (2014).
DOI: 10.1016/j.compositesa.2014.02.010

[17] Hoes K., Dinescu D., Sol H., Vanheule M., Parnas R. S., Luo Y., Verpoest I.: New set-up for measurement of permeability properties of fibrous reinforcements for RTM. Composites Part A: Applied Science and Manufacturing, **33**, 959–969 (2002).
DOI: 10.1016/S1359-835X(02)00035-0

[18] Rieber G., Mitschang P.: 2D permeability changes due to stitching seams. Composites Part A: Applied Science and Manufacturing, **41**, 2–7 (2010).
DOI: 10.1016/j.compositesa.2009.09.006

[19] Weitzenböck J. R., Shenoi R. A., Wilson P. A.: Measurement of three-dimensional permeability. Composites Part A: Applied Science and Manufacturing, **29**, 159–169 (1998).
DOI: 10.1016/S1359-835X(97)00049-3

[20] Nedanov P. B., Advani S. G.: A method to determine 3D permeability of fibrous reinforcements. Journal of Composite Materials, **36**, 241–254 (2002).
DOI: 10.1177/0021998302036002462

[21] Okonkwo K., Simacek P., Advani S. G., Parnas R. S.: Characterization of 3D fiber preform permeability tensor in radial flow using an inverse algorithm based on sensors and simulation. Composites Part A: Applied Science and Manufacturing, **42**, 1283–1292 (2011).
DOI: 10.1016/j.compositesa.2011.05.010

[22] Stöven T., Weyrauch F., Mitschang P., Neitzel M.: Continuous monitoring of three-dimensional resin flow through a fibre preform. Composites Part A: Applied Science and Manufacturing, **34**, 475–480 (2003).
DOI: 10.1016/S1359-835X(03)00059-9

[23] Valdes-Parada F. J., Ochoa-Tapia J. A., Alvarez-Ramirez J.: Validity of the permeability Carman–Kozeny equation: A volume averaging approach. Physica A: Statistical Mechanics and its Applications, **388**, 789–798 (2009).
DOI: 10.1016/j.physa.2008.11.024

[24] Morren G., Bossuyt S., Sol H.: 2D permeability tensor identification of fibrous reinforcements for RTM using an inverse method. Composites Part A: Applied Science and Manufacturing, **39**, 1530–1536 (2008).
DOI: 10.1016/j.compositesa.2008.05.019

[25] Morren G., Bottiglieri M., Bossuyt S., Sol H., Lecompte D., Verleye B., Lomov S. V.: A reference specimen for permeability measurements of fibrous reinforcements for RTM. Composites Part A: Applied Science and Manufacturing, **40**, 244–250 (2009).
DOI: 10.1016/j.compositesa.2008.11.011

[26] Hammond V. H., Loos A. C.: The effects of fluid type and viscosity on the steady-state and advancing front permeability behavior of textile preforms. Journal of Reinforced Plastics and Composites, **16**, 50–72 (1997).
DOI: 10.1177/073168449701600105

[27] Parnas R. S., Salem A. J.: A comparison of the unidirectional and radial in-plane flow of fluids through woven composite reinforcements. Polymer Composites, **14**, 383–394 (1993).
DOI: 10.1002/pc.750140504

[28] Francucci G., Rodríguez E. S., Vázquez A.: Study of saturated and unsaturated permeability in natural fiber fabrics. Composites Part A: Applied Science and Manufacturing, **41**, 16–21 (2010).
DOI: 10.1016/j.compositesa.2009.07.012

[29] Liu Q., Parnas R. S., Giffard H. S.: New set-up for in-plane permeability measurement. Composites Part A: Applied Science and Manufacturing, **38**, 954–962 (2007).
DOI: 10.1016/j.compositesa.2006.06.024

[30] Bickerton S., Sozer E. M., Graham P. J., Advani S. G.: Fabric structure and mold curvature effects on preform permeability and mold filling in the RTM process. Part I. Experiments. Composites Part A: Applied Science and Manufacturing, **31**, 423–438 (2000).
DOI: 10.1016/S1359-835X(99)00087-1

[31] Bickerton S., Sozer E. M., Šimácek P., Advani S. G.: Fabric structure and mold curvature effects on preform permeability and mold filling in the RTM process. Part II. Predictions and comparisons with experiments. Composites Part A: Applied Science and Manufacturing, **31**, 439–458 (2000).
DOI: 10.1016/S1359-835X(99)00088-3

[32] Adams K. L., Rebenfeld L.: In-plane flow of fluids in fabrics: Structure/flow characterization. Textile Research Journal, **57**, 647–654 (1987).
DOI: 10.1177/004051758705701104

[33] Adams K. L., Rebenfeld L.: Permeability characteristics of multilayer fiber reinforcements. Part II: Theoretical model. Polymer Composites, **12**, 186–190 (1991).
DOI: 10.1002/pc.750120308

[34] Adams K. L., Russel W. B., Rebenfeld L.: Radial penetration of a viscous liquid into a planar anisotropic porous medium. International Journal of Multiphase Flow, **14**, 203–215 (1988).
DOI: 10.1016/0301-9322(88)90006-7

[35] Adams K. L., Rebenfeld L.: Permeability characteristics of multilayer fiber reinforcements. Part I: Experimental observations. Polymer Composites, **12**, 179–185 (1991).
DOI: 10.1002/pc.750120307

[36] Chan A. W., Hwang S-T.: Anisotropic in-plane permeability of fabric media. Polymer Engineering and Sciene, **31**, 1233–1239 (1991).
DOI: 10.1002/pen.760311613

[37] Weitzenböck J. R., Shenoi R. A., Wilson P. A.: Radial flow permeability measurement. Part A: Theory. Composites Part A: Applied Science and Manufacturing, **30**, 781–796 (1999).
DOI: 10.1016/S1359-835X(98)00183-3

[38] Schledjewski R., Grössing H., Fauster E.: Accurate 2D permeability measurement: Optical permeability characterisation. in: 'SAMPE SETEC 2013: Novel aspects in composite technologies: From fibre to light weight structures. Wuppertal, Germany' 34–40 (2013).

[39] Stadtfeld H. C.: Entwicklung einer Messzelle zur Bestimmung von Kompaktierungs- und Permeabilitätskennwerten bei flächigen Faserhalbzeugen. PhD thesis, Technische Universität Kaiserslautern, Kaiserslautern (2006).

[40] Dungan F. D., Sastry A. M.: Saturated and unsaturated polymer flows: Microphenomena and modeling. Journal of Composite Materials, **36**, 1581–1603 (2002).
DOI: 10.1177/0021998302036013179

[41] Arbter R., Beraud J. M., Binetruy C., Bizet L., Bréard J., Comas-Cardona S., Demaria C., Endruwei A., Ermanni P., Gommer F., Hasanovic S., Henrat P., Klunker F., Laine B., Lavanchy S., Lomov S. V., Long A., Michaud V., Morren G., Ruiz E., Sol H., Trochu F., Verleye B., Wietgrefe M., Wu W., Ziegmann G.: Experimental determination of the permeability of textiles: A benchmark exercise. Composites Part A: Applied Science and Manufacturing, **42**, 1157–1168 (2011). DOI: 10.1016/j.compositesa.2011.04.021

[42] Pan R., Liang Z., Zhang C., Wang B.: Statistical characterization of fiber permeability for composite manufacturing. Polymer Composites, **21**, 996–1006 (2000). DOI: 10.1002/pc.10253

[43] Endruweit A., Long A. C.: Influence of stochastic variations in the fibre spacing on the permeability of bi-directional textile fabrics. Composites Part A: Applied Science and Manufacturing, **37**, 679–694 (2006). DOI: 10.1016/j.compositesa.2005.08.003

[44] Endruweit A., Long A. C., Robitaille F., Rudd C. D.: Influence of stochastic fibre angle variations on the permeability of bi-directional textile fabrics. Composites Part A: Applied Science and Manufacturing, **37**, 122–132 (2006). DOI: 10.1016/j.compositesa.2005.04.014

[45] Endruweit A., McGregor P., Long A. C., Johnson M. S.: Influence of the fabric architecture on the variations in experimentally determined in-plane permeability values. Composites Science and Technology, **66**, 1778–1792 (2006). DOI: 10.1016/j.compscitech.2005.10.031

[46] Endruweit A., Gommer F., Long A. C.: Stochastic analysis of fibre volume fraction and permeability in fibre bundles with random filament arrangement. Composites Part A: Applied Science and Manufacturing, **49**, 109–118 (2013). DOI: 10.1016/j.compositesa.2013.02.012

[47] Fauster E., Grössing H., Schledjewski R.: Uncertainty analysis for optical permeability measurement of reinforceding textiles. in: 'Proceedings of ICCM 19, Montreal, Canada' 5802–5809 (2013).

[48] Daniel P., Kissinger C., Roeder G.: Anordnung zur Vermessung der Ausbreitung eines Matrixmaterials in elektrisch leitfähigen Verstärkungsstrukturen. DE 10004146 C2, Germany (2000).

[49] Kissinger C., Mitschang P., Neitzel M., Roeder G., Haberland R.: Continuous on-line permeability measurement of textile structures. in: 'Proceedings of the 45th International SAMPE Symposium and Exhibition, Long Beach, California, USA', 2089–2096 (2000).

[50] Rieber G.: Einfluss von textilen Parametern auf die Permeabilität von Multifilamentgeweben für Faserverbundkunststoffe. PhD thesis, Technische Universität Kaiserslautern, Kaiserslautern (2011).

[51] Lekakou C., Johari M. A. K. B., Bader M. G.: Compressibility and flow permeability of two-dimensional woven reinforcements in the processing of composites. Polymer Composites, **17**, 666–672 (1996). DOI: 10.1002/pc.10658

[52] Summerscales J.: A model for the effect of fibre clustering on the flow rate in resin transfer moulding. Composites Manufacturing, **4**, 27–31 (1993). DOI: 10.1016/0956-7143(93)90013-X

eXPRESS Polymer Letters Vol.9, No.2 (2015) 143–153
Available online at www.expresspolymlett.com
DOI: 10.3144/expresspolymlett.2015.15

UV-curable nanocasting technique to prepare bioinspired superhydrophobic organic-inorganic composite anticorrosion coatings

K. C. Chang[1], T. L. Chuang[2], W. F. Ji[1], C. H. Chang[1], Y. Y. Peng[2], H. Shih[2], C. L. Hsu[3], J. M. Yeh[1], W. C. Tang[4], Y. C. Su[4]*

[1]Department of Chemistry, Center for Nanotechnology and Biomedical Technology at Chung-Yuan Christian University (CYCU), 32023 Chung Li, Taiwan, Republic of China
[2]Master Program in Nanotechnology and Center for Nanotechnology at CYCU, 32023 Chung Li, Taiwan, Republic of China
[3]Department of Physics, Center for Nanotechnology at Chung-Yuan Christian University (CYCU), 32023 Chung Li, Taiwan, Republic of China
[4]Division of Applied Chemistry, Material and Chemical Research Laboratories, Industrial Technology Research Institute, 30011 Hsinchu, Taiwan, Republic of China

Received 4 August 2014; accepted in revised form 4 October 2014

Abstract. A UV-curing technique was used to develop advanced anticorrosive coatings made of a poly(methyl methacrylate) (PMMA)/silica composite (PSC) with bioinspired *Xanthosoma sagittifolium* leaf-like superhydrophobic surfaces. First of all, a transparent soft template with negative patterns of xanthosoma sagittifolium leaf can be fabricated by thermally curing the polydimethylsiloxane (PDMS) pre-polymer in molds at 60°C for 4 h, followed by detaching PDMS template from the surface of natural leaf. PSC coatings with biomimetic structures can be prepared by performing the UV-radiation process upon casting UV-curable precursor with photo-initiator onto cold-rolled steel (CRS) electrode under PDMS template. Subsequently, UV-radiation process was carried out by using light source with light intensity of 100 mW/cm^2 with exposing wavelength of 365 nm. Surface morphologies of the as-synthesized hydrophobic PMMA (HP) and superhydrophobic PSC (SPSC) coatings showed a large number of micro-scaled mastoids, each decorated with many nano-scaled wrinkles that were systematically investigated by using scanning electron microscopy (SEM). The contact angles of water droplets on the sample surfaces can be increased from ~81 and 103° on PMMA and PSC surfaces to ~148 and 163° on HP and SPSC surfaces, respectively. The SPSC coating was found to provide an advanced corrosion protection effect on CRS electrodes compared to that of neat PMMA, PSC, and HP coatings based on a series of electrochemical corrosion measurements in 3.5 wt% NaCl electrolyte. Enhanced corrosion protection of SPSC coatings on CRS electrodes can be illustrated by that the silica nanoparticles on the small papillary hills of the bioinspired structure of the surface further increased the surface roughness, making the surface exhibit superior superhydrophobic, and thus leading to much better anticorrosion performance.

Keywords: *coatings, polymer composite, bioinspired, superhydrophobic, anticorrosion*

1. Introduction

Corrosion is the deterioration of materials by chemical interaction with their environment. The consequences of corrosion are many and varied; corrosion's effects on the safe, reliable, and efficient operation of equipment or structures are often more serious than the simple loss of a metal mass. Several corrosion-control methods are available, such as inhibitors, cathodic protection [1], anodic protection [2], coating [3], and alloying. Among the above methods, polymeric (or organic) coatings have been employed to protect metals against corrosion for a

*Corresponding author, e-mail: juiming@cycu.edu.tw

long time. The primary effect of a polymeric coating is to function as a physical barrier against corrosive species such as O^2 and H^+.

Superhydrophobic (or ultrahydrophobic) surfaces are those on which the water contact angle (WCA) is 150° and higher. A lotus leaf is a classic example of a natural superhydrophobic surface with a WCA of larger than 150° [4]. The superhydrophobic effect is due to both of low surface energy materials and hierarchical (nano-/macro-) structures. The surface is also characterized by a very low water roll-off angle (*i.e.*, very low WCA hysteresis [5]). Previous research has shown that water droplets on these textured surfaces readily sit on the apexes of the nanostructures because air bubbles fill the valleys of the structures under the droplets. Water drops on such surfaces cannot penetrate the micro- or nanostructures and wet the surface, resulting in extremely high contact angles; thus, these naturally occurring leaves exhibit considerable superhydrophobicity. Numerous methods, including photolithography [6], plasma treatment [7], templates [8], chemical deposition [9], sol-gel processes [10], chemical vapor deposition (CVD) [11], casting, and chemical etching [12], have been utilized to fabricate superhydrophobic surfaces.

Several studies have been reported on using polymers and polymer nanocomposites for various applications such as fabricating hydrophobic/superhydrophobic surfaces [13–21]. Therefore, development of hydrophobic/superhydrophobic polymers and polymer nanocomposites has become an interesting subject in materials science. Very few studies have reported on the use of polymer and polymer nanocomposite coatings to study the anticorrosive properties that hydrophobic/superhydrophobic surfaces provide [22–26]. However, organic polymer-inorganic silica composite anticorrosion coatings with bioinspired superhydrophobic surfaces have never been studied. Therefore, we demonstrated a feasible strategy to develop advanced PMMA/silica composite (PSC) anticorrosion coatings by a nanocasting method along with a UV-curing technique designed to directly duplicate fresh plant leaf surfaces (such as *Xanthosoma sagittifolium* leaves). The imprint of the approximate superhydrophobic *Xanthosoma sagittifolium* leaf was transferred onto the composite surface so that the resulting composite exhibited the approximate superhydrophobicity required to prevent corrosion.

Traditionally, some resins utilized for their anticorrosion properties require the use of organic solvents, which significantly increase human health risks. As new regulations regarding the emission of volatile organic compounds (VOCs) are put into effect, increased demands for environmentally friendly (green) coating systems will require the progressive substitution of greener compounds in place of hazardous coatings. Among the alternatives are waterborne and solvent-free coatings. Thus, we developed an eco-friendly process to prepare composite anticorrosion coatings without using solvents. The composite anticorrosion coatings developed in this study provided multiple effects to protect metals from corrosion. One is the bioinspired structure with superhydrophobicity approximately equivalent to that of *Xanthosoma sagittifolium* leaf that can repel moisture and further reduce the water/corrosive media adsorption on the PMMA surfaces, preventing the underlying metals from corrosion. The other is the silica nanoparticle on the small papillary hills of the bioinspired structure, which enhances the surface hydrophobicity to a superhydrophobic degree, leading to a better anticorrosion effect. The detailed anticorrosion performance of the developed SPSC coatings was evaluated by a series of electrochemical corrosion measurements. Corrosion protection studies were performed on a sample-coated cold-rolled steel (CRS) immersed in a corrosive medium (3.5 wt% sodium chloride aqueous solution).

2. Experimental section

2.1. Chemicals and instruments

Methyl methacrylate (MMA; Aldrich, 99.0%, USA) was doubly distilled prior to use. Photo-initiator alpha-Benzyl-alpha-(dimethylamino)-4-morpholinobutyro-phenon (Aldrich, 97.0%, USA), tetraethyl orthosilicate (TEOS; Fluka, 98.0%, Germany), 3-(trimethoxysilyl)propyl methacrylate (MSMA; Acros, 98.0%, Belgium), ethanol (EtOH; Riedel-de Haën, 99.8%, Germany), and ammonium hydroxide solution (NH_3; Aldrich, 25.0%, USA) were used as received without further purification. The liquid components (Sylgard 184, Dow corning, USA) of polydimethylsiloxane (PDMS) were supplied by the Dow Corning Corporation. All the reagents were of reagent grade unless otherwise stated.

Fourier transform infrared (FTIR) spectra were recorded using an FTIR spectrometer (JASCO FT/

IR-4100, Japan) at room temperature. Surface morphologies of the superhydrophobic samples were observed by using SEM (JOEL JSM-7600F, Japan) and AFM (PSIA XE-100 STM SESTAM, Korea). Contact angles were measured using a First Ten Angstroms FTA 125 (USA) goniometer at ambient temperatures. Water droplets (about 4 μL) were carefully dropped onto the surfaces of the samples, and the contact angles were determined from the average of five measurements at various positions on the samples' surfaces. The corrosion potential and corrosion current of sample-coated CRS electrodes were electrochemically measured using a VoltaLab 50 potentiostat/galvanostat. Electrochemical impedance spectroscopy (EIS) measurements were recorded on an AutoLab (PGSTAT302N, Netherlands) potentiostat/galvanostat electrochemical analyzer.

2.2. Synthesis of vinyl-modified silica (VMS) particles

VMS particles were prepared by conventional base-catalyzed sol-gel reactions of TEOS in the presence of MSMA molecules (Figure 1a). The procedure was similar to previously described methods [27]. A typical procedure to prepare the VMS particles was given as follows: 0.52 g (0.0025 mole) of TEOS and 2.48 g (0.01 mole) of MSMA were mixed in a 250 mL beaker under ultrasonic. A separate solution of 50 mL H_2O that add a little 15 N NH_3 to control the pH = 9 under magnetically stirring at room temperature. Then, the MSMA and TEOS solution was slowly added into the H_2O solution with stirring for 12 h at 60°C. After the sol-gel reactions, the as-prepared VMS particles were thus obtained. The raw silica (RS) was also prepared through the conventional sol-gel reactions of TEOS molecules simultaneously as control experiments without the addition of MSMA monomers.

2.3. Preparation of PDMS template

The PDMS prepolymer was obtained by mixing the elastomer base and a curing agent in a proper ratio (10:1, w/w). The PDMS pre-polymer was poured into 3×6 cm^2 molds fixed to a piece of fresh, natural *Xanthosoma sagittifolium* leaf (the veins of the leaf were removed in an area of about 3×6 cm^2) and then cured in a 60°C oven for 4 h. After curing, the PDMS blocks were separated from the molds and used as templates for imprinting. The thick of PDMS template was 3.0 mm.

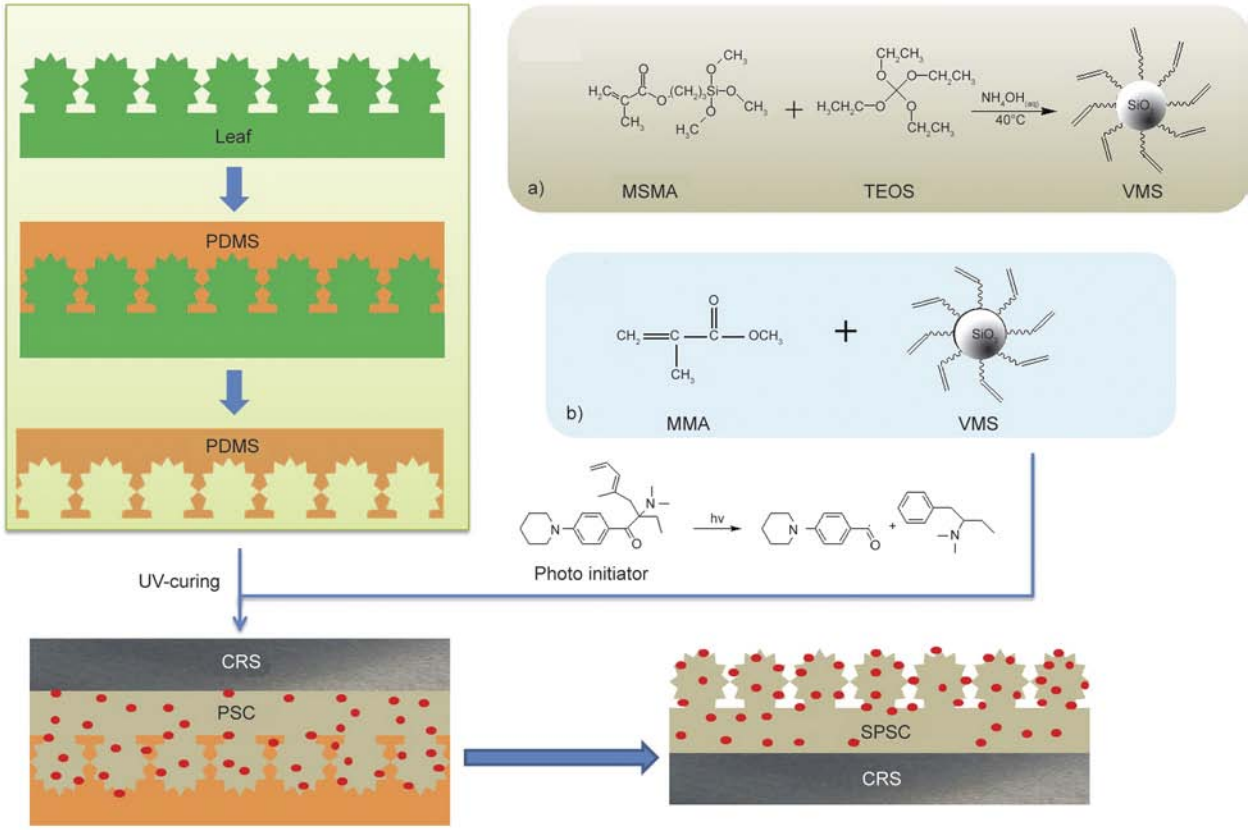

Figure 1. Preparation process of (a) VMS particles and (b) superhydrophobic surfaces of an organic-inorganic composite by using a nanocasting method combined with a UV-curing technique

2.4. UV-curable SPSC coatings

Figure 1b shows a schematic diagram for the fabrication of SPSC coating materials. First, a PDMS prepolymer was cast against a fresh *Xanthosoma sagittifolium* leaf surface and then cured under appropriate conditions. The prepared PDMS template has negative *Xanthosoma sagittifolium* leaf surface structures, and was obtained after peeling the leaf off. Second, the substrate was covered with the UV-curable precursor solution, and the template was pressed against the CRS. It was then exposed to UV-light (fusion UV-curing, light intensity = 2000 mJ/cm^2) for 300 s. After the UV-curing process and peeling off the PDMS template, a *Xanthosoma sagittifolium* leaf-like surface was formed on the CRS.

2.5. Electrochemical measurements of coatings

Electrochemical corrosion measurements were performed using a VoltaLab 50 device. All the electrochemical corrosion measurements were performed in a double-wall jacketed cell, covered with a glass plate, in which water was maintained at a constant operational temperature of 25±0.5°C. The open-circuit potential (OCP) in the equilibrium state of the system was recorded as the corrosion potential (E_{corr} in mV versus a saturated calomel electrode (SCE)). Tafel plots were obtained by scanning the potential from –500 to 500 mV above E_{corr} at a scan rate of 10 mV/min. The corrosion current (I_{corr}) was determined by superimposing a straight line along the linear portion of the cathodic or anodic curve and extrapolating it through E_{corr}. The corrosion rate (R_{corr}, in milli-inches per year, MPY) was calculated using Equation (1) [28]:

$$R_{corr}[\mathrm{MPY}] = \frac{0.13\, I_{corr}(E.W.)}{A \cdot d} \quad (1)$$

where $E.W.$ is the equivalent weight [g/eq.], A is the area [cm^2], and d is the density [g/cm^3].

An AutoLab (PGSTAT302N) potentiostat/galvanostat was employed to perform the a.c. impedance spectroscopy measurements. The impedance measurements were carried out in the frequency range 100 kHz–100 MHz with pure iron (area, 1×1 cm^2) as the working electrode embedded in epoxy, Pt as the counter electrode, and SCE as the reference electrode. The working electrode was first maintained in the test environment for 30 min before the impedance run. All experiments were conducted at room temperature. All raw data were collected at least three times to ensure reproducibility and statistical significance.

3. Results and discussion

3.1. Spectroscopic studies of VMS particles

In this study, the as-prepared VMS particles were synthesized from the process of acid-catalyzed sol-gel reaction of TEOS in the presence of MSMA molecules and subsequently characterized by FTIR, ^{13}C-NMR and ^{29}Si-NMR spectroscopy. Figure 2a shows the representative FTIR spectroscopy of as-prepared RS and VMS particles. For example, the characteristic peaks located at 1711, 1654 and 1433 cm^{-1} were assigned to the stretching of C=O, C=C and –CH_3, respectively [29]. The presence of organic groups in the materials after hydrolysis and condensation was confirmed using solid-state NMR spec-

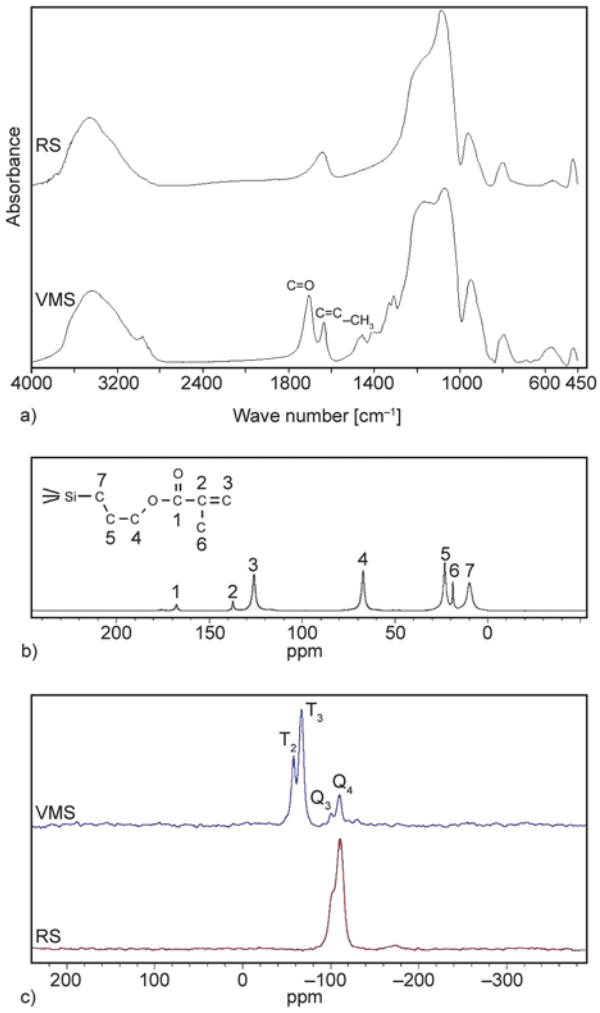

Figure 2. (a) FTIR absorption spectra of RS and VMS particles, (b) ^{13}C CP-MAS NMR spectra of VMS particles, (c) ^{29}Si MAS NMR spectra of RS and VMS particles

troscopy. The solid-state ^{13}C CP MAS NMR spectra displayed seven resonances for VMS sample, corresponding to vinyl carbons at 127.1 and 137.1 ppm *vs.* VMS [29], as shown in Figure 2b. Moreover, solid-state ^{29}Si MAS NMR provides information about the silicon environment. The ^{29}Si MAS NMR spectra of RS and VMS samples were presented in Figure 2c. RS particles exhibited two resonances at –100.8 and –110.4 ppm, corresponding to $HOSi(OSi)_3$ (Q^3) and $Si(OSi)_4$ (Q^4) silicate species, respectively. Upon modifying the surface with vinyl group using MSMA, the ^{29}Si MAS NMR spectrum show two additional resonances at –56.76 and –65.96 ppm that were assigned to $R–Si(OH)_2(OSi)$ (T^1) and $R–Si(OH)(OSi)_2$ (T^2) centers [29], respectively.

3.2. Microscopic observations

A photograph of natural fresh *Xanthosoma sagittifolium* leaves is shown in Figure 3a. Figure 3b is a high-magnification SEM image of the fresh *Xanthosoma sagittifolium* leaf. The average WCA on the fresh *Xanthosoma sagittifolium* leaves is *ca.* 146±2° (Figure 3b). In Figure 3b, many small papillary hills are clearly visible on the natural *Xanthosoma sagittifolium* leaf. The diameters of the small papillary hills are between 7 and 9 μm. Figure 3c is an SEM image of the PDMS template prepared by casting the liquid PDMS directly onto a natural fresh *Xanthosoma sagittifolium* leaf. Many holes with diameters of 7–9 μm are shown on the surface of the PDMS template. Figure 3c shows the topographic structure of the holes on the surface that complements the papillary hills on the natural fresh *Xanthosoma sagittifolium* leaf. This result demonstrates that the template effectively replicated the topologically inverted structures of the *Xanthosoma sagittifolium* leaf surfaces.

Figure 4 shows the structures on the surfaces of the nanocast layers on the CRS slides as observed using SEM. Numerous papillary microstructures (average diameter, *ca.* 7–9 μm) were formed on the surfaces. The papillary microstructures are the replicas of the surface patterns on the *Xanthosoma sagittifolium* leaves. Compared with the surface structure of HP (Figure 4a–4c), many silica nanoparticles emerged

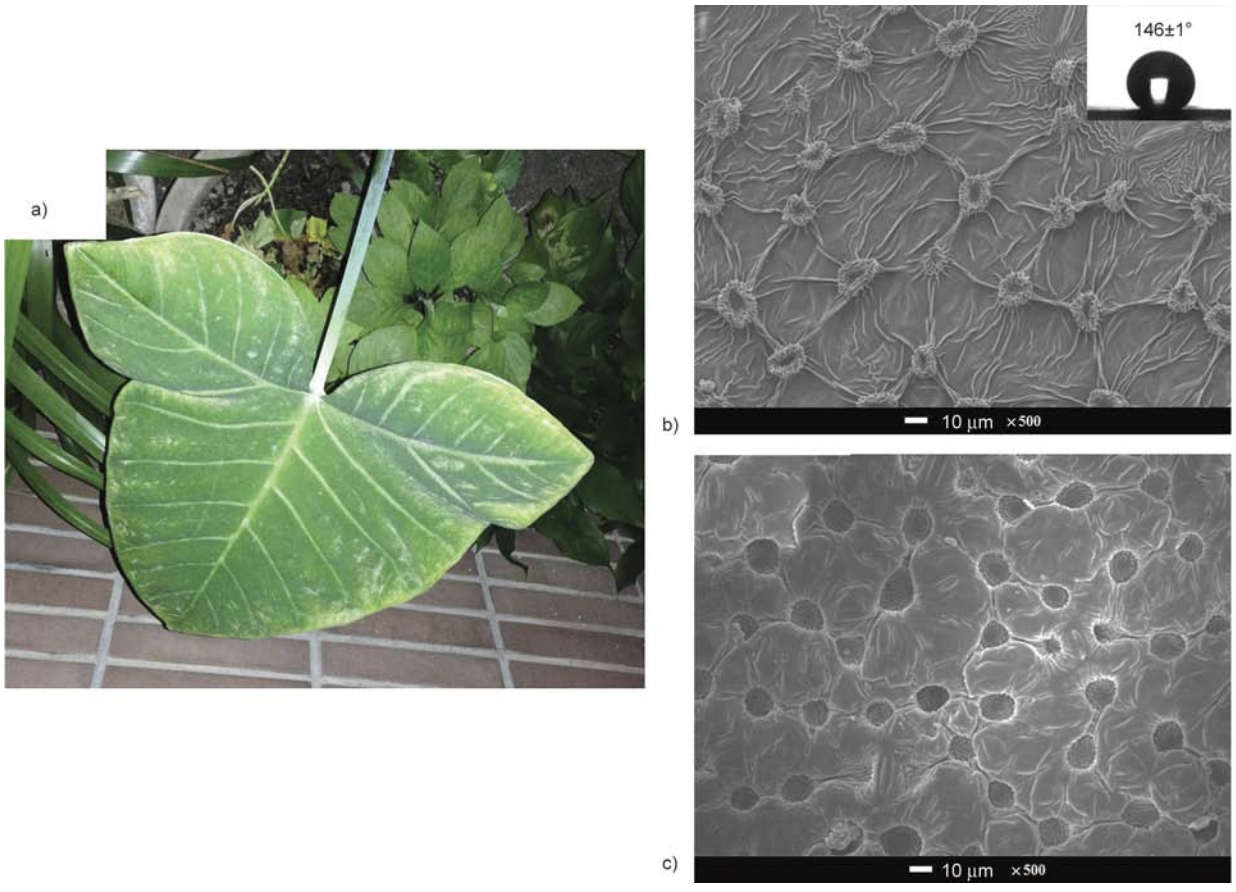

Figure 3. (a) Photograph of *Xanthosoma sagittifolium* leaves. (b) SEM image of a fresh natural leaf. Illustration shows the water contact angle of a *Xanthosoma sagittifolium* leaf. (c) PDMS negative template.

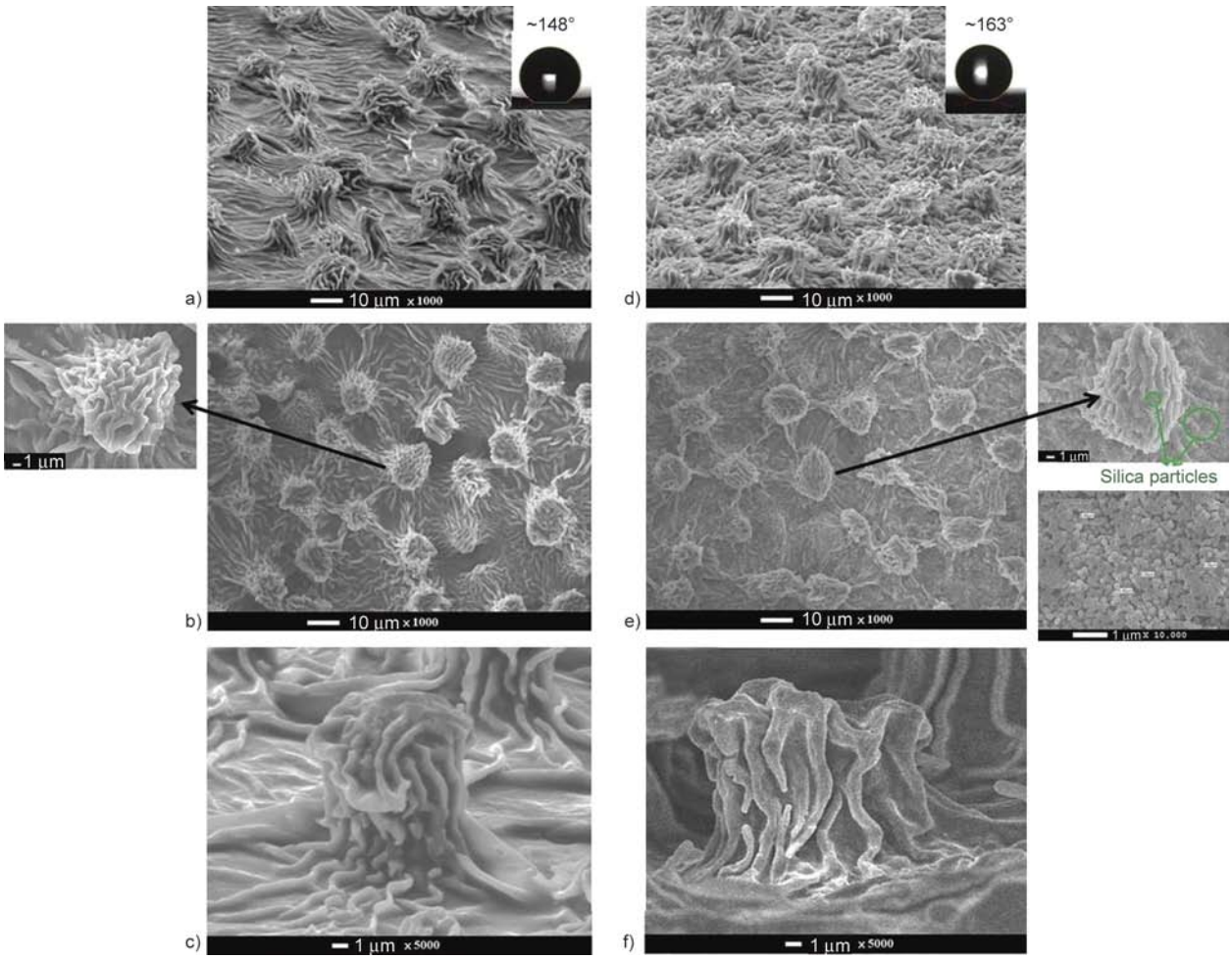

Figure 4. SEM images for (a, d) the *Xanthosoma sagittifolium* leaf-like hydrophobic surface of PMMA and the superhydrophobic surface of the composite. The inset shows the contact angle of the surface. (b, e) Top views of the surface of PMMA and the composite. The inset of (e) shows the silica particles. (c, f) Section views of the surfaces of PMMA and the composite.

on the papillary and surface microstructures of SPSC (Figure 4d–4f). The average size of these nanoparticles is about 340±40 nm.

The chemical compositions of the surfaces of the HP and SPSC coatings were analyzed by using EDX spectroscopy (Figure 5). The spectrum of HP showed peaks for carbon and oxygen, but no silicon was detected. However, the EDX spectrum of SPSC yielded carbon, oxygen, and silicon peaks. For SPSC, the weight percentages of silicon were 34.20 and 41.15% for the papillary and surface microstructures, respectively. The presence of the silicon peak indicates that the silica nanoparticles are actually on the papillary and surface microstructures.

In order to better understand the surface topography and the extent of surface roughness on the surfaces of the HP and SPSC coatings, AFM studies were performed in which height images were obtained and average roughness levels of the surfaces were determined. Figure 6 show three-dimensional AFM images of HP and SPSC coatings on CRS substrates. It can be seen that papillary nanostructures, which are replicas of the *Xanthosoma sagittifolium* leaf, were formed on the surfaces. The surface morphology shown by the AFM images is consistent with the SEM observations. Using these AFM images, the root-mean-square (RMS) roughness levels of the HP and SPSC coatings were measured. The HP coating had an RMS roughness of 1.482 μm; the SPSC coating displayed a rougher surface consisting of large silica domains with an RMS roughness of 1.645 μm.

Because providing a surface with nanostructures is essential for fabricating a superhydrophobic surface, we created a superhydrophobic surface by using a nanocasting technique along with silica nanoparticles on the small papillary hills of the bioinspired structure.

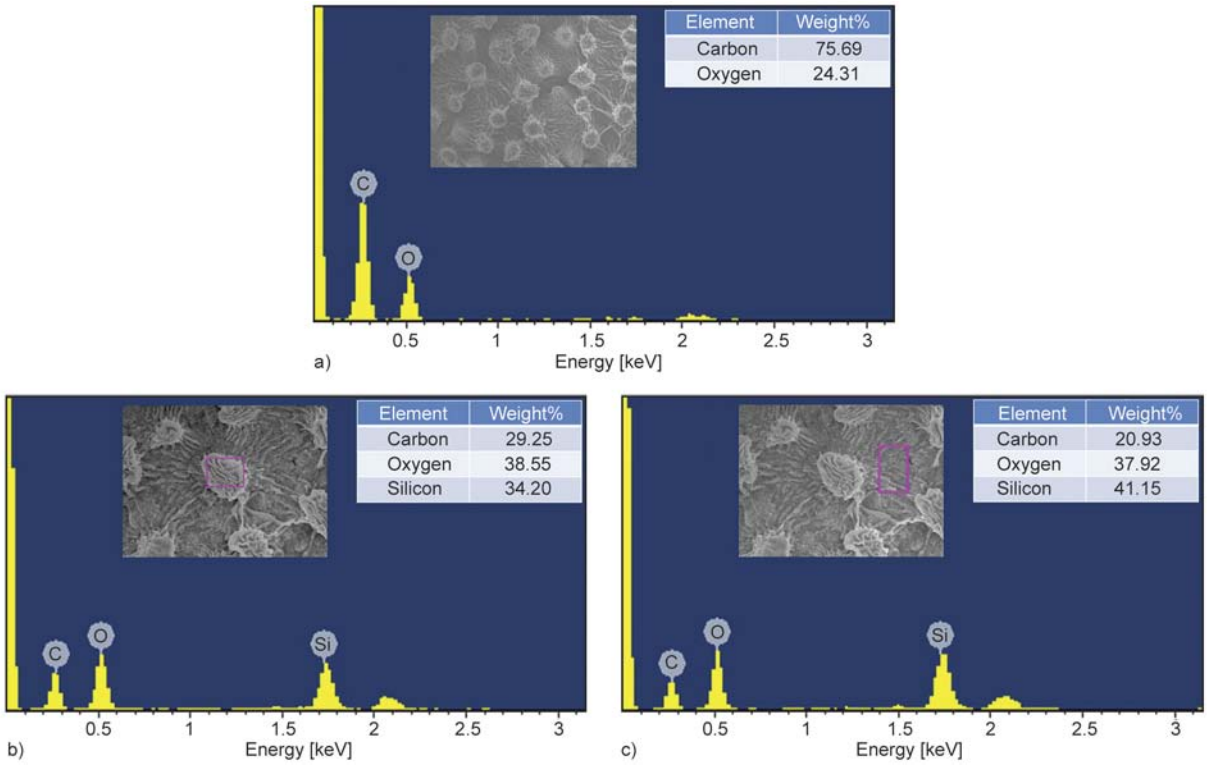

Figure 5. EDX spectra of (a) HP, (b) papillary microstructures of SPSC and (c) the surface microstructure of SPSC

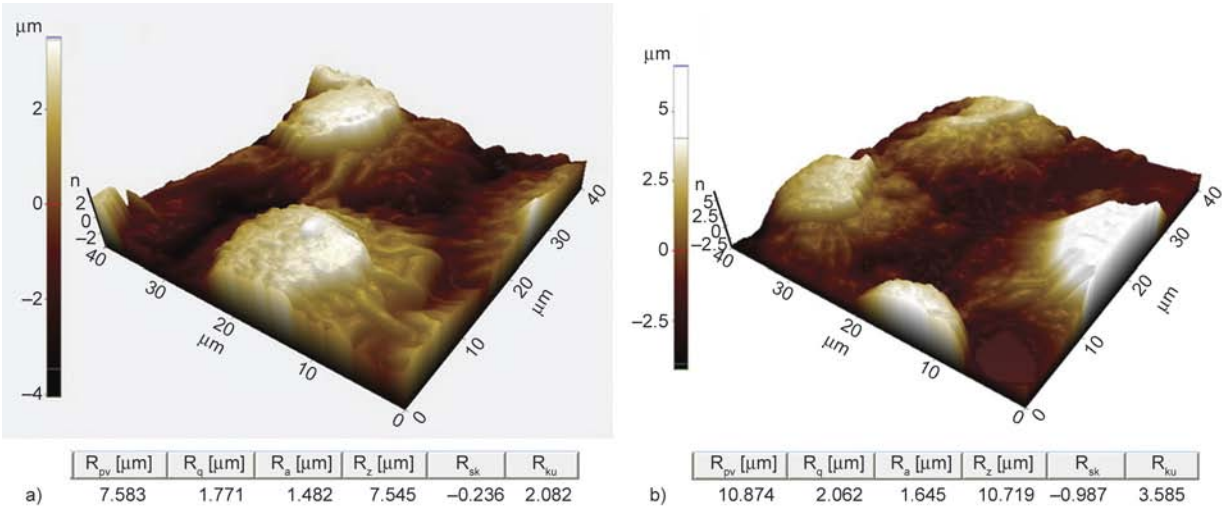

Figure 6. 3D topographical images (a) HP and (b) SPSC surfaces

3.3. Contact angle (wettability) measurements

The coating material replicated from the fresh *Xanthosoma sagittifolium* leaves showed superhydrophobic characteristics and a large WCA. The WCAs of PMMA, HP, PSC, and SPSC are shown in Table 1. The results show that the WCA became as high as 163±1° with a hysteresis of 4° for SPSC. As a significant amount of air was trapped between the papillary hills of the SPSC surface, a water drop on such a coating could only make contact with the tops of the papillary hills. Thus, the water placed on the surface of the SPSC coating was likely resting on a thin air cushion. In addition, the silica nanoparticles increased the roughness of the SPSC coating, which could lead to the formation of more air pockets, trapping more air, and minimizing the contact area; thus, the surface hydrophobicity was further enhanced.

Figure 7 shows the change in the water contact angle with various times for SPSC. The durability of the water repellent on the SPSC coating is a very important parameter. The SPSC was stored at room temperature in the ambient atmosphere for one month, and water contact angles were measured hereafter. Almost no decrease in the water contact

Table 1. Contact angle and electrochemical corrosion measurements of bare CRS, PMMA, PSC, HP and SPSC coated electrodes

Sample code	Electrochemical corrosion measurements[a]				P_{EF}%	Thickness [µm]	Contact angle [°/H_2O][b]	Hysteresis angle [°/H_2O]8
	E_{corr} [mV vs SCE]	R_p [kΩ·cm^2]	I_{corr} [µA/cm^2]	R_{corr} [MPY]				
CRS	–825	1.15	17.45	16.24	–	–	–	–
PMMA	–685	14.67	2.21	2.06	92.16	16±2	81±1	1
PSC	–587	23.45	1.79	1.67	95.10	18±2	103±1	1
HP	–501	58.27	0.75	0.70	98.03	19±2	148±1	2
SPSC	–320	296.91	0.03	0.03	99.61	19±2	163±1	4

[a]Saturated calomel electrode (SCE) was employed as a reference electrode.
[b]The contact angle was determined from the average of five measurements at various positions on the samples' surface.

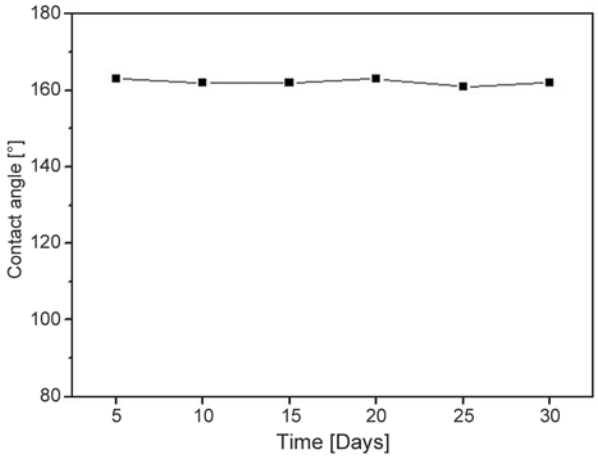

Figure 7. Change in water contact angle with various times for SPSCm

angle was observed, indicating that the superhydrophobic property of the as-prepared SPSC coating is stable enough.

The ability of a coating to protect metal substrates against corrosion depends on three aspects: (1) sorption of water onto the coating, (2) transport of water throughout the coating, and (3) accessibility of water to the coating/substrate interface. Therefore, it is reasonable to accept that the low-wettability SPSC effectively prevented the water from adsorbing onto the substrate surface and therefore exhibited excellent corrosion resistance in wet environments.

3.4. Potentiodynamic and electrochemical impedance measurements

On the basis of a series of electrochemical measurements (*i.e.*, corrosion potential, polarization resistance, and corrosion current measured in a corrosive medium (3.5 wt% aqueous NaCl electrolyte)), we concluded that the SPSC coating was more effective at protecting the CRS electrode against corrosion than the common HP, PSC, and PMMA coatings. Information about corrosion current can be obtained by extrapolating Tafel plots from both the cathodic and anodic polarization curves for the respective corrosion processes [30]. Extrapolating the cathodic and anodic polarization curves to their point of intersection provides both the corrosion potential and the corrosion current. Corrosion protection studies were performed on samples with 17±3 µm-thick coatings and which were immersed in a corrosive medium for 30 min. Tafel plots for the four samples immersed in the corrosive medium are shown in Figure 8; the corresponding data are listed in Table 1. Generally, higher E_{corr} and polarization resistance, R_p, values and lower I_{corr} and R_{corr} values indicate better corrosion protection.

The R_p values were evaluated from the Tafel plots according to the Stearn–Geary equation (Equation (2)) [31]:

$$R_p = \frac{b_a b_c}{2.303(b_a + b_c)} I_{corr} \quad (2)$$

where, I_{corr} is determined by an intersection of the linear portions of the anodic and cathodic curves

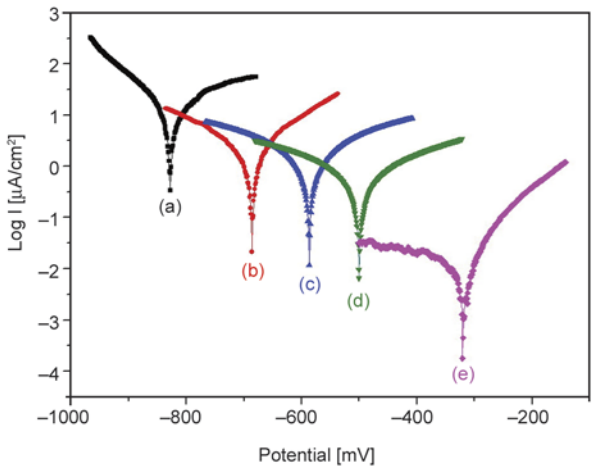

Figure 8. Tafel plots for (a) bare, (b) PMMA-coated, (c) PSC-coated, (d) HP-coated and (e) SPSC-coated CRS electrodes measured at 25±0.5°C

and b_a and b_c are the anodic and cathodic Tafel slopes (*i.e.*, $\Delta E/\Delta \log I$), respectively.

The Tafel plots for the sample-coated CRS electrodes indicate corrosion potentials of E_{corr} = –685, –587, and –501 mV for the PMMA, PSC and HP coatings, respectively, which were more positive than that for the bare CRS electrode, for which E_{corr} = –825 mV. Moreover, the corrosion currents (I_{corr}) of the PMMA, PSC, and HP-coated CRS electrodes were *ca*. 2.21, 1.79, and 0.75 μA/cm^2, which were significantly lower than that of the bare CRS electrode (*i.e.*, 17.45 μA/cm^2).

The corresponding I_{corr} and R_{corr} decreased considerably when we used the PSC-coated bare CRS electrode with *Xanthosoma sagittifolium*-leaf–like structures (SPSC) to obtain superhydrophobic properties. Moreover, the E_{corr} and R_p of the SPSC-coated CRS electrode was more positive and larger than that of the HP-coated CRS electrode, as E_{corr} and R_p increased from –501 to –320 mV (*vs*. SCE) and 58.27 to 296.91 kΩ·cm^2, respectively, for the SPSC-coated CRS electrode.

The protection efficiency (P_{EF}%) values were estimated using the Equation (3) [32]:

$$P_{EF}\% = 100\frac{R_p^{-1}(\text{uncoated}) - R_p^{-1}(\text{coated})}{R_p^{-1}(\text{uncoated})} \quad (3)$$

The SPSC coatings exhibited a P_{EF} of 99.61%, suggesting that SPSC is more effective in preventing electrochemical corrosion than PMMA, PSC, and HP, which had P_{EF} values of 92.16, 95.10, and 98.03%, respectively.

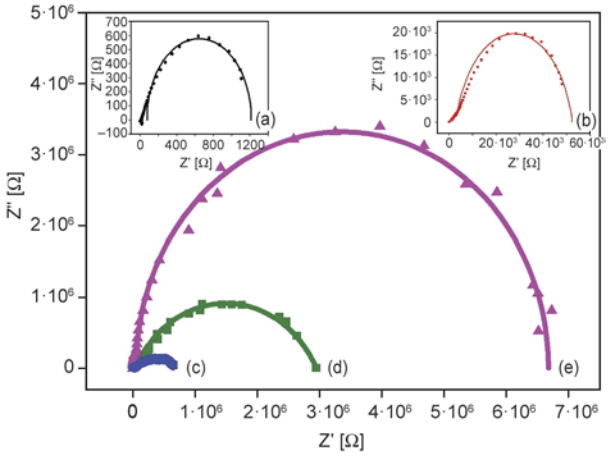

Figure 9. Nyquist plots for (a) bare, (b) PMMA-coated, (c) PSC-coated, (d) HP-coated, and (e) SPSC-coated CRS electrodes

Figure 9 shows the Nyquist plots of the four measured samples. The first sample (a) is uncoated CRS. A series of samples denoted as (b), (c), (d), and (e) represent the CRS-coated by PMMA, PSC, HP, and SPSC, respectively. The charge transfer resistances of all samples, as determined by subtracting the intersection of the high-frequency end from the low-frequency end of the semicircle arc with the real axis, were 0.001, 0.048, 0.645, 2.95, and 6.52 MΩ·cm^2. EIS Bode plots (impedance *vs*. frequency) of all samples are shown in Figure 10. Z_{real} is a measure of corrosion resistance [33]. Low Z_{real} value could be brought about by very high capacitance and/or very low resistance of the coating [34]. Large value of the capacitance has been related to the high extent at which water has penetrated the coating [35]. In the case of Bode plots, the value of Z_{real} at the lowest frequency also represents the corrosion resistance. The Bode magnitude plots for uncoated CRS and CRS-coated by PMMA, PSC,

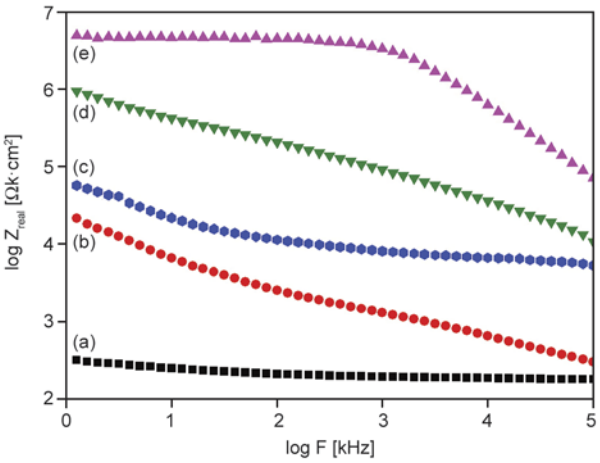

Figure 10. Bode plots for (a) bare, (b) PMMA-coated, (c) PSC-coated, (d) HP-coated and (e) SPSC-coated CRS electrodes

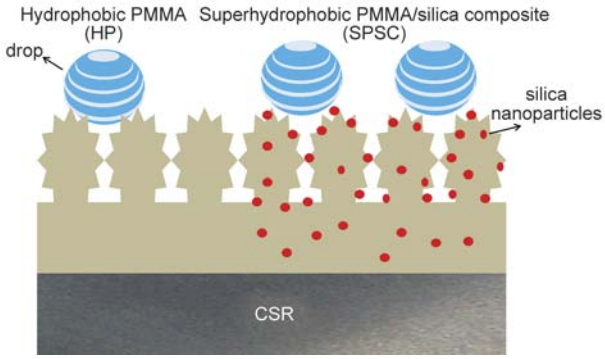

Figure 11. Schematic representation of hydrophobic and superhydrophobic surfaces of HP and SPSC coatings

HP, and SPSC shows Z_{real} values of 2.5, 4.3, 4.8, 6.0 and 6.7 kΩ·cm^2, respectively, at low frequency end. The electrochemical results show that the SPSC coating provided better protection against corrosion of the CRS electrode than the other coatings did; this is mainly attributed to the superhydrophobicity of the SPSC coating compared to HP, PSC, and PMMA coatings, which may have resulted from the super water-repellent property, as shown in Figure 11. This is evidenced by the contact angle (wettability) measurements of the as-prepared coatings.

4. Conclusions

Advanced anticorrosion coatings of PSC with bioinspired *Xanthosoma sagittifolium* leaf-like superhydrophobic surfaces were successfully prepared by using a nanocasting method along with a UV-curing technique. Surface morphologies of as-prepared SPSC coatings were found to contain a large number of micro-scaled mastoids, each decorated with many nano-scaled wrinkles. The WCA of the SPSC coating whose surface was imprinted with the bioinspired pattern of the surface of a natural leaf was about 163°, which was significantly larger than that of the HP coating (*i.e.*, WCA = 148°). This is because the silica nanoparticles on the small papillary hills of the bioinspired structure enhanced the surface hydrophobicity to a superhydrophobic degree. The superhydrophobicity of SPSC materials affords them excellent anticorrosive properties.

Acknowledgements

The authors acknowledge financial support from the Ministry of Science and Technology, Taiwan, R.O.C. (NSC 101-2113-M-033-005-MY3), and the Center for Nanotechnology and Biomedical Technology at CYCU.

References

[1] Edinger C., Grimaudo V., Broekmann P., Waldvogel S. R.: Stabilizing lead cathodes with diammonium salt additives in the deoxygenation of aromatic amides. ChemElectroChem, **1**, 1018–1022 (2014). DOI: 10.1002/celc.201402050

[2] Chirkunov A. A., Gorbachev A. S., Kuznetsov Y. I., Shikhaliev K. S.: Inhibition of anodic dissolution of low-carbon steel with alkyl phosphonates in borate buffer solution. Protection of Metals and Physical Chemistry of Surfaces, **48**, 769–772 (2012). DOI: 10.1134/S2070205112070040

[3] Correa E., Zuleta A. A., Guerra L., Gómez M. A., Castaño J. G., Echeverría F., Liu H., Skeldon P., Thompson G. E.: Tribological behavior of electroless Ni–B coatings on magnesium and AZ91D alloy. Wear, **305**, 115–123 (2013). DOI: 10.1016/j.wear.2013.06.004

[4] Lai S. C. S.: Mimicking nature: Physical basis and artificial synthesis of the Lotus–effect. University of Leiden, Leiden (2003).

[5] Extrand C. W.: Model for contact angles and hysteresis on rough and ultraphobic surfaces. Langmuir, **18**, 7991–7999 (2002). DOI: 10.1021/la025769z

[6] Chen L., Yang G., Wang S.: Air-grid surface patterning provided by superhydrophobic surfaces. Small, **8**, 962–965 (2012). DOI: 10.1002/smll.201102345

[7] Oliveira N. M., Reis R. L., Mano J. F.: Superhydrophobic surfaces engineered using diatomaceous earth. ACS Applied Materials and Interfaces, **5**, 4202–4208 (2013). DOI: 10.1021/am4003759

[8] Sun M., Luo C., Xu L., Ji H., Oujang Q., Yu D., Chen Y.: Artificial lotus leaf by nanocasting. Langmuir, **21**, 8978–8981 (2005). DOI: 10.1021/la050316q

[9] Zang D., Li F., Geng X., Lin K., Clegg P. S.: Tuning the wettability of an aluminum surface via a chemically deposited fractal dendrite structure. The European Physical Journal E, **36**, 59/1–59/8 (2013). DOI: 10.1140/epje/i2013-13059-2

[10] Mahadik S. A., Fernando P. D., Hegade N. D., Wagh P. B., Gupta S. C.: Durability and restoring of superhydrophobic properties in silica-based coatings. Journal of Colloid and Interface Science, **405**, 262–268 (2013). DOI: 10.1016/j.jcis.2013.04.042

[11] Wang J., Song X., Rui L., Shen J., Yang G., Huang H.: Fluorocarbon thin film with superhydrophobic property prepared by pyrolysis of hexafluoropropylene oxide. Applied Surface Science, **258**, 9782–9785 (2012). DOI: 10.1016/j.apsusc.2012.06.029

[12] Ou J., Hu W., Xue M., Wang F., Li W.: Superhydrophobic surfaces on light alloy substrates fabricated by a versatile process and their corrosion protection. ACS Applied Materials and Interfaces, **5**, 3101–3107 (2013). DOI: 10.1021/am4000134

[13] Gu H. Y., Qi Z. Y., Wu W., Zeng Y., Song L. X.: Superhydrophobic polyimide films with high thermal endurance via UV photo-oxidation. Express Polymer Letters, **8**, 588–595 (2014). DOI: 10.3144/expresspolymlett.2014.62

[14] Wu Z., Wang H., Xue M., Tian X., Ye X., Zhou H., Cui Z.: Facile preparation of superhydrophobic surfaces with enhanced releasing negative air ions by a simple spraying method. Composites Science and Technology, **94**, 111–116 (2014). DOI: 10.1016/j.compscitech.2014.01.019

[15] Bayer I. S., Steele A., Loth E.: Superhydrophobic and electroconductive carbon nanotube-fluorinated acrylic copolymer nanocomposites from emulsions. Chemical Engineering Journal, **221**, 522–530 (2013).
DOI: 10.1016/j.cej.2013.01.023

[16] Wolfs M., Darmanin T., Guittard F.: Superhydrophobic nanofiber arrays and flower-like structures of electrodeposited conducting polymers. Soft Matter, **8**, 9110–9114 (2012).
DOI: 10.1039/C2SM26274F

[17] Chen Z. M., Pan S. J., Yin H. J., Zhang L. L., Ou E. C., Xiong Y. Q., Xu W. J.: Facile synthesis of superhydrophobic TiO_2/polystyrene core-shell microspheres. Express Polymer Letters, **5**, 38–46 (2011).
DOI: 10.3144/expresspolymlett.2011.5

[18] Ding X., Zhou S., Gu G., Wu L.: A facile and large-area fabrication method of superhydrophobic self-cleaning fluorinated polysiloxane/TiO_2 nanocomposite coatings with long-term durability. Journal of Materials Chemistry, **21**, 6161–6164 (2011).
DOI: 10.1039/C0JM04546B

[19] Schutzius T. M., Tiwari M. K., Bayer I. S., Megaridis C. M.: High strain sustaining, nitrile rubber based, large-area, superhydrophobic, nanostructured composite coatings. Composites Part A: Applied Science and Manufacturing, **42**, 979–985 (2011).
DOI: 10.1016/j.compositesa.2011.03.026

[20] Manoudis P. N., Karapanagiotis I., Tsakalof A., Zuburtikudis I., Panayiotou C.: Superhydrophobic composite films produced on various substrates. Langmuir, **24**, 11225–11232 (2008)
DOI: 10.1021/la801817e

[21] Yilgor I., Bilgin S., Isik M., Yilgor E.: Facile preparation of superhydrophobic polymer surfaces. Polymer, **53**, 1180–1188 (2012).
DOI: 10.1016/j.polymer.2012.01.053

[22] Grignard B., Vaillant A., de Coninck J., Piens M., Jonas A. M., Detrembleur C., Jerome C.: Electrospinning of a functional perfluorinated block copolymer as a powerful route for imparting superhydrophobicity and corrosion resistance to aluminum substrates. Langmuir, **27**, 335–342 (2011).
DOI: 10.1021/la102808w

[23] de Leon A. C. C., Pernites R. B., Advincula R. C.: Superhydrophobic colloidally textured polythiophene film as superior anticorrosion coating. ACS Applied Materials and Interfaces, **4**, 3169–3176 (2012).
DOI: 10.1021/am300513e

[24] Singh B. P., Jena B. K., Bhattacharjee S., Besra L.: Development of oxidation and corrosion resistance hydrophobic graphene oxide-polymer composite coating on copper. Surface and Coatings Technology, **232**, 475–481 (2013).
DOI: 10.1016/j.surfcoat.2013.06.004

[25] Peng C-W., Chang K-C., Weng C-J., Lai M-C., Hsu C-H., Hsu S-C., Li S-Y., Wei Y., Yeh J-M.: UV-curable nanocasting technique to prepare bio-mimetic superhydrophobic non-fluorinated polymeric surfaces for advanced anticorrosive coatings. Polymer Chemistry, **4**, 926–932 (2013).
DOI: 10.1039/C2PY20613G

[26] Chang K-C., Ji W-F., Lai M-C., Hsiao Y-R., Hsu C-H., Chuang T-L., Wei Y., Yeh J-M, Liu W-R.: Synergistic effects of hydrophobicity and gas barrier properties on the anticorrosion property of PMMA nanocomposite coatings embedded with graphene nanosheets. Polymer Chemistry, **5**, 1049–1056 (2014).
DOI: 10.1039/C3PY01178J

[27] Yeh J-M., Chang K-C., Peng C-W., Chiou S-C., Hwang S-S., Yang J-C., Lin H-R.: Effect of vinyl-modified silica and raw silica particles on the properties of as-prepared polymer-silica nanocomposite foams. Journal of Nanoscience and Nanotechnology, **8**, 6297–6305 (2008).
DOI: 10.1166/jnn.2008.354

[28] Wei Y., Wang J., Jia X., Yeh J-M., Spellane P.: Polyaniline as corrosion protection coatings on cold rolled steel. Polymer, **36**, 4535–4537 (1995).
DOI: 10.1016/0032-3861(95)96866-7

[29] Yu Y-Y., Chen C-Y., Chen W-C.: Synthesis and characterization of organic–inorganic hybrid thin films from poly(acrylic) and monodispersed colloidal silica. Polymer, **44**, 593–601 (2003).
DOI: 10.1016/S0032-3861(02)00824-8

[30] Beving D. E., McDonnell A. M. P., Yang W. S., Yan Y. S.: Corrosion resistant high-silica-zeolite MFI coating. One general solution formulation for aluminum alloy AA-2024-T3, AA-5052-H32, AA-6061-T4, and AA-7075-T6. Journal of the Electrochemical Society, **153**, B325–B329 (2006).
DOI: 10.1149/1.2207845

[31] Stern M., Geary A. L.: Electrochemical polarization. I. A theoretical analysis of the shape of polarization curves. Journal of the Electrochemical Society, **104**, 56–63 (1957).
DOI: 10.1149/1.2428496

[32] Bockris J., Reddy K. N.: Modern electrochemistry. Plenum Press, New York (1976).

[33] Zucchi F., Grassi V., Frignani A., Monticelli C., Trabanelli G.: Electrochemical behaviour of a magnesium alloy containing rare earth elements. Journal of Applied Electrochemistry, **36**, 195–204 (2006).
DOI: 10.1007/s10800-005-9053-3

[34] Kannan M. B., Gomes D., Dietzel W., Abetz V.: Polyoxadiazole-based coating for corrosion protection of magnesium alloy. Surface and Coatings Technology, **202**, 4598–4601 (2008).
DOI: 10.1016/j.surfcoat.2008.03.027

[35] Rammelt U., Reinhard G.: Application of electrochemical impedance spectroscopy (EIS) for characterizing the corrosion-protective performance of organic coatings on metals. Progress in Organic Coatings, **21**, 205–226 (1992).
DOI: 10.1016/0033-0655(92)87005-U

eXPRESS Polymer Letters Vol.9, No.2 (2015) 154–164
Available online at www.expresspolymlett.com
DOI: 10.3144/expresspolymlett.2015.16

A colourimetric method for the determination of the degree of chemical cross-linking in aspartic acid-based polymer gels

B. Gyarmati[1], *N. Hegyesi*[1,2], *B. Pukánszky*[1,2], *A. Szilágyi*[1*]

[1]Department of Physical Chemistry and Materials Science, Budapest University of Technology and Economics, Budafoki út 8., H-1111 Budapest, Hungary
[2]Institute of Materials Science and Environmental Chemistry, Research Centre for Natural Sciences, Hungarian Academy of Sciences, P.O. Box 286, H-1519 Budapest, Hungary

Received 9 May 2014; accepted in revised form 5 October 2014

Abstract. A 2,4,6-trinitrobenzenesulphonic acid (TNBS)-based assay is developed to determine the degree of chemical cross-linking in aspartic acid-based polymer gels. The conventional colourimetric method for the quantitative determination of amine groups is difficult to use in polymer networks; thus, an improved method is developed to analyse polymer gels swollen in dimethyl sulfoxide (DMSO). Reaction products of the derivatizing reaction are examined by NMR. The chemical stability of the reagent is increased in DMSO, and the method shows satisfactory linearity and accuracy. The degree of chemical cross-linking in the investigated gels is close to its theoretical maximum, but the conversion of the pendant amine groups to cross-linking points is strongly dependent on the feed composition of the gels.

Keywords: *polymer gels, 2,4,6-trinitrobenzene-sulphonic acid, poly(aspartic acid), degree of cross-linking, cross-linking ratio*

1. Introduction

Polymer hydrogels are good candidates for several bio-related applications because of their large water-absorbing capacity, soft tissue-like properties, viscoelastic character and permeability to the influx and efflux of small molecular compounds [1–5]. The swelling properties and mechanical strength of the hydrogels are determined mainly by the cross-link density, which is the number of physical and chemical net points that connect polymer chains in a unit volume of gel [1, 6–8]. Although several theoretical models are available for the estimation of cross-linking density (*e.g.*, Flory-Rehner swelling theory [9]), these models have several limitations and cannot distinguish chemical from physical net points. However, chemical net points are of particular importance because they are stable under physiological conditions and determine the maximum degree of swelling of hydrogels.

The goal of this work was to develop a simple analytical method for quantifying the number of chemical cross-links in aspartic acid-based polymer gels [10–13]. Polysuccinimide (PSI) gels are obtained by cross-linking PSI with diamines, and cross-linked PSI gels can be hydrolysed into poly(aspartic acid) (PASP) gels. During the cross-linking of PSI, some of the diamine molecules remain unreacted, whereas others react with the polymer through only one of their amine groups so pendant amine groups remain in the network. Cross-linker molecules reacting with both amine groups form chemical cross-links between polymer chains. The cross-linking ratio (X_{FEED}) is defined as the number of moles of cross-linker molecules per the number of moles of repeating units of the polymer [14]. The structure of the formed network can be characterized by the degree of chemical cross-linking which is the molar ratio of diamine molecules that form chemical cross-link-

*Corresponding author, e-mail: aszilagyi@mail.bme.hu

ing points to the repeating units of the polymer in PSI and PASP gels. Essentially, the degree of chemical cross-linking is only equal to the cross-linking ratio if the conversion rate of the reaction is 100%. The degree of chemical cross-linking of PASP gels was previously determined by Torma *et al*. [14]. The concentration of unreacted cross-linker molecules was quantified using ninhydrin, whereas the concentration of pendant amine groups was determined by aqueous acid-base potentiometric titration. However, the equilibration time can be long for every titration step in the case of cross-linked polymers. Thus, this method is very time-consuming because a large number of data points must be determined to obtain a reliable titration curve. A method that requires considerably fewer data points would be highly beneficial.

In the colourimetric method developed in this study, the degree of chemical cross-linking was determined using 2,4,6-trinitrobenzene-sulphonic acid (TNBS), which is a well-known reagent for the quantitative determination of primary amine groups in chromatography. In alkaline aqueous solution, TNBS reacts with amine groups via bimolecular aromatic nucleophilic substitution, resulting in a yellow adduct with absorption maxima at 340 nm (trinitrophenyl amine) and 420 nm (Meisenheimer complex) [15–20]. Simultaneously, TNBS hydrolyses to picric acid, which exhibits overlapping peaks with the main product, trinitrophenyl amine (Figure 1) [21]. The reaction constant of the hydrolysis is a few orders of magnitude smaller than that of the main reaction (*e.g.,* the pseudo first-order rate constant for the amine group of lysine is $9 \cdot 10^{-4}$ 1/s whereas for hydroxyl groups is $1.4 \cdot 10^{-7}$ 1/s) [22]; thus, the side reaction does not interfere with the quantitative determination of small molecules [15, 22]. However, the side reaction is not negligible in slow reactions; hence, the conventional TNBS assay cannot be applied directly to determine the concentration of amine groups in polymer gels. Moreover, the rate of the hydrolysis to picric acid strongly depends on the ionic strength [22], which is difficult to maintain at a well-defined value in the presence of a polyelectrolyte gel [2, 8, 23]. The dissimilar reaction rates of by-product formation in the analyte and in the blank solution might cause inaccuracies during absorbance measurements and in the quantitative determination of amine groups. Some researchers tried to solve this difficulty by hydrolysing the gels to small molecules in strongly acidic solution after the reaction with TNBS [24–28]. However, controlling the degradation of the polymer might be difficult under the extreme reaction conditions, which resulting in the formation of poorly defined oligomers and other by-products. Consequently, we employed a new strategy to exclude the formation of picric acid by changing the solvent of the assay to DMSO and to be able to perform the assay under mild reaction conditions. The reaction mechanism is proposed based on ^{1}H NMR measurements of the model reaction of TNBS and the cross-linker molecules. The degree of chemical cross-linking was determined as a function of the feed composition of the gels.

2. Experimental

2.1. Materials and instruments

Imidazole (puriss p.a.), 1,4-diaminobutane (DAB, 99%) and 2,4,6-trinitrobenzenesulphonic acid (TNBS, 1 M in H_2O, analytical reagent) solutions were acquired from Sigma-Aldrich Ltd., Hungary. Dibutylamine (DBA, 99%), sodium tetraborate decahy-

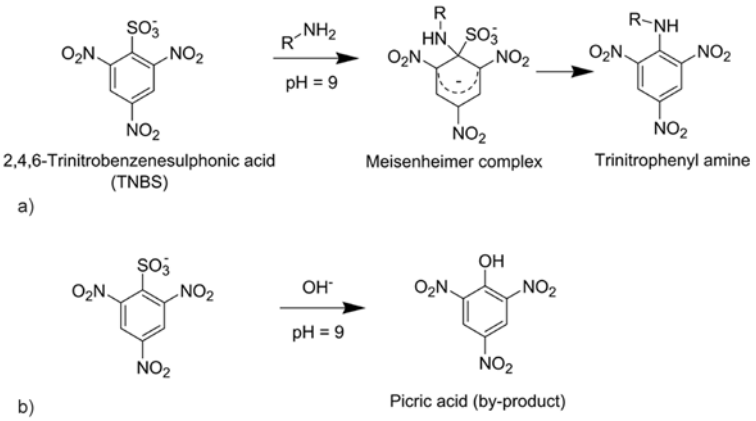

Figure 1. Reaction of 2,4,6-trinitrobenzenesulphonic acid (TNBS) with a) primary amines and b) hydroxyl ions

drate (a.r.), cysteamine hydrochloride (97%), cystamine dihydrochloride (98%), potassium chloride (99.5%), sodium bromate (99%), poly(vinyl alcohol) (PVA, M_W = 60 kDa, 98% hydrolysed), glutardialdehyde (GDA, 25wt% solution in water for synthesis), S-aspartic acid (99%) and dithiothreitol (DTT, for biochem.) were purchased from Merck Ltd., Hungary. *N*,*N*-Dimethylformamide (DMF, pure) was bought from Lach Ner, Czech Republic. Dimethyl sulphoxide (DMSO, analytical grade) was obtained from Fisher Chemical, Hungary. De-ionized water (Milli-Q reagent grade, κ > 18.2 Ω·m, Millipore, USA) was used for each analysis and for the preparation of buffer solutions. All reagents and solvents were used without further purification.

The pH of the buffer solutions was verified using a pH/ion analyser (Radelkis OP-271/1, Hungary). Absorbance measurements were performed using a Specord 200 UV-Vis spectrophotometer (Analytik Jena, Germany) with a quartz cuvette (path length = 1 cm, V = 3 mL). The spectral resolution was 1 nm, and the scanning speed was 10 nm/s. Nuclear magnetic resonance (NMR) experiments were performed on a Bruker Avance 300 spectrometer (USA) operating at 300 MHz. ^{1}H NMR spectra were recorded using 128 scans.

A buffer solution of pH = 8 was prepared from imidazole (c = 0.1 M); the pH was adjusted to 8 by the addition of 1 M HCl. A buffer solution of pH = 9.3 was prepared from sodium tetraborate decahydrate (c = 0.1 M) and used in aqueous reactions of TNBS. The ionic strength of the buffers was maintained at 0.15 M by the addition of KCl.

2.2. Synthesis

Polysuccinimide (PSI) was synthesized by the thermal polycondensation of aspartic acid as reported in a previous study [29]. The average molecular weight of PSI was M_W = 56 kDa. PSI-DAB gels were prepared by cross-linking PSI with DAB (Figure 2). In

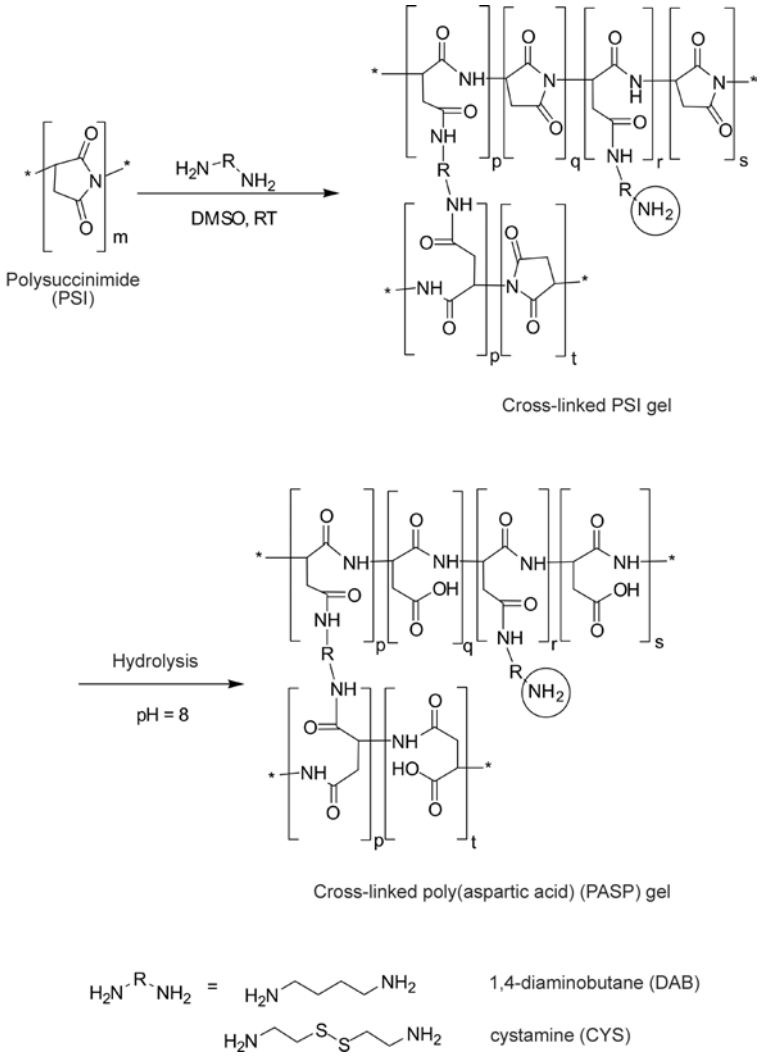

Figure 2. The synthesis of polysuccinimide (PSI) and poly(aspartic acid) (PASP) gels

brief, PSI was dissolved in DMSO (9.70 wt%), and the solution of DAB (8.80 wt% in DMSO) was added dropwise to the polymer solution. The precursor solution of gels was transferred into Eppendorf tubes ($V \cong 1$ mL). Although the gelation of the solution could be visually observed after a few minutes (Table 1), the gels were kept in the tubes for 24 hours to complete the cross-linking process. The PSI-DAB gels were immersed in aqueous buffer solution (pH = 8) and the gels became opaque at first because water is a poor solvent of PSI. The PSI-DAB gels hydrolysed to PASP-DAB gels within 3 days and homogeneous, transparent gels were yielded. The degree of swelling (Q_m) of the PSI-DAB gel is defined as the mass ratio of the prepared gel to the dried gel; $Q_{m,\,pH=8}$ of the PASP-DAB gel is defined as the mass ratio of PASP-DAB gel swollen at pH = 8 to the dried gel. The mass of the dried gel was determined by immersing the gel piece into water, followed by a drying step in vacuum at 25°C.

Table 1. Cross-linking ratio, gelation time and degree of swelling of the gels

Sample	X_{FEED}[a] [–]	t_{gel}[b] [min]	Q_m[c] [–]	$Q_{m,\,pH=8}$[d] [–]
A	1/5	3–5	5.0	7.5
B	1/10	5–8	7.2	15.2
C	1/15	8–10	9.0	18.3
D	1/20	18–20	9.3	20.5

[a]X_{FEED}: cross-linking ratio which is the number of moles of cross-linker molecules per the number of moles of repeating units of the polymer,
[b]t_{gel}: gelation time of PSI-DAB gel determined by visual observation,
[c]Q_m: the mass ratio of the prepared PSI-DAB gel to the dried gel,
[d]$Q_{m,\,pH=8}$: the mass ratio of the PASP-DAB gel at pH = 8 to the dried gel

2.3. Determination of degree of chemical cross-linking of PASP-DAB hydrogels in water

The degree of chemical cross-linking of PASP-DAB gels was determined in two main steps as shown in Figure 3. In the first step, unreacted diamine molecules were extracted from the PASP-DAB gels ($m \cong 1$ g) by washing the gels with buffer solution (5·1000 µL, pH = 9.3). The amine content of the

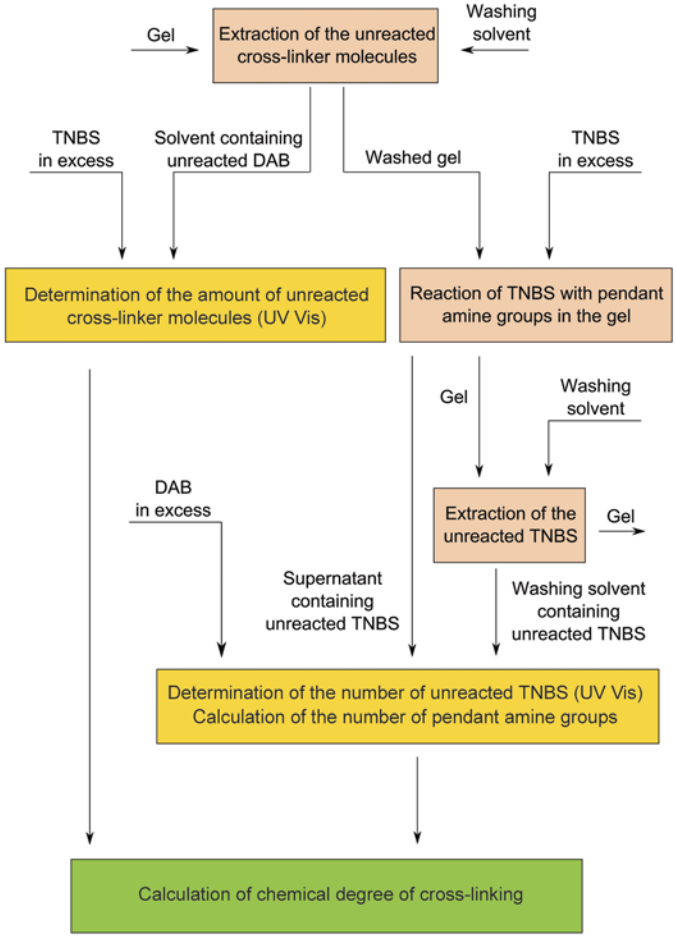

Figure 3. Flow-chart of the quantification of unreacted cross-linker molecules and pendant amine groups inside the gels

washing solution was determined after adding TNBS (50 μL, 30 mM TNBS in water) in excess to 2000 μL of the analyte. The absorbance of the analyte solution was measured after 30 min against a blank buffer solution (pH = 9.3) containing TNBS at the same concentration as in the analyte. Calibration of the method was done using DAB in alkaline aqueous solution (c_{TNBS} = 7.3·10^{-4} M, pH = 9.3, λ = 420 nm, ε = 15364 M^{-1}·cm^{-1}, r^2 = 0.9956).

In the second step, a washed gel sample ($m \cong 0.01$ g) was immersed in aqueous solution of TNBS (500 μL, 3 mM, pH = 9.3) and reacted for 3 h at 25°C. The gel was removed and the unreacted TNBS was extracted from the gel by washing with buffer solution (3·500 μL, pH = 9.3). The TNBS content of the solution was determined by the addition of DAB (50 μL, 8.80 wt%) in excess to 5000 μL of the analyte. The concentration of unreacted reagent was determined from its absorbance spectrum.

2.4. Determination of degree of chemical cross-linking of PSI-DAB gels in DMSO

The degree of chemical cross-linking of PSI-DAB gels was determined similarly as in the case of PASP-DAB gels, but the solvent was replaced from water to DMSO (Table 1). Thus, in the first step (Figure 3), unreacted diamine molecules were removed from the PASP-DAB gels ($m \cong 1$ g) by washing the gels with DMSO (5·1000 μL DMSO). The amine content of the washing solution was determined after adding TNBS (50 μL, 300 mM in DMSO) to 2000 μL of the analyte. The absorbance of the analyte solution was measured after 30 min against the blank solution of TNBS in DMSO. Calibration was done in DMSO using TNBS in excess (c_{TNBS} = 7.3·10^{-3} M, λ = 437 nm, ε = 625 M^{-1}·cm^{-1}, r^2 = 0.9992).

In the second step, a washed gel sample ($m \cong 0.01$ g) was immersed in TNBS (375 μL, 30 mM in DMSO) and reacted for 1 day. The gel was removed and the unreacted TNBS was extracted from the gel by washing (3·500 μL DMSO). The TNBS content of the solution was determined by the addition of DAB (125 μL, 8.80 wt% in DMSO) in excess to 5000 μL of the analyte. The concentration of the reaction product was determined from its absorbance spectrum. Calibration was done in DAB excess (c_{DAB} = 25·10^{-3} M, λ = 437 nm, ε = 18 393 M^{-1}·cm^{-1}, r^2 = 0.9995).

2.5. Accuracy and stability

A widely accepted reference method does not exist for the determination of the number of pendant amine groups. Thus, we applied a method based on the determination of small molecules to determine accuracy because the TNBS assay for small molecular amines is well-established. Disulphide cross-linked PSI gels (PSI-CYS) were synthesized by the reaction of PSI and cystamine (CYS) (Figure 2). 950 mg of polymer solution (PSI in DMF, 5.00 wt%) was diluted with 451 mg DMF, and then 23 mg cystamine hydrochloride was dissolved in the same solution. 34 μL dibutylamine as a deprotonating agent was added dropwise to the solution under continuous stirring. The solution was poured into Eppendorf tubes ($V \cong 1$ mL) and kept there for 24 h to yield gels. The concentration of pendant amine groups in PSI-CYS gel was determined in DMSO as described previously in the case of PSI-DAB gels after careful

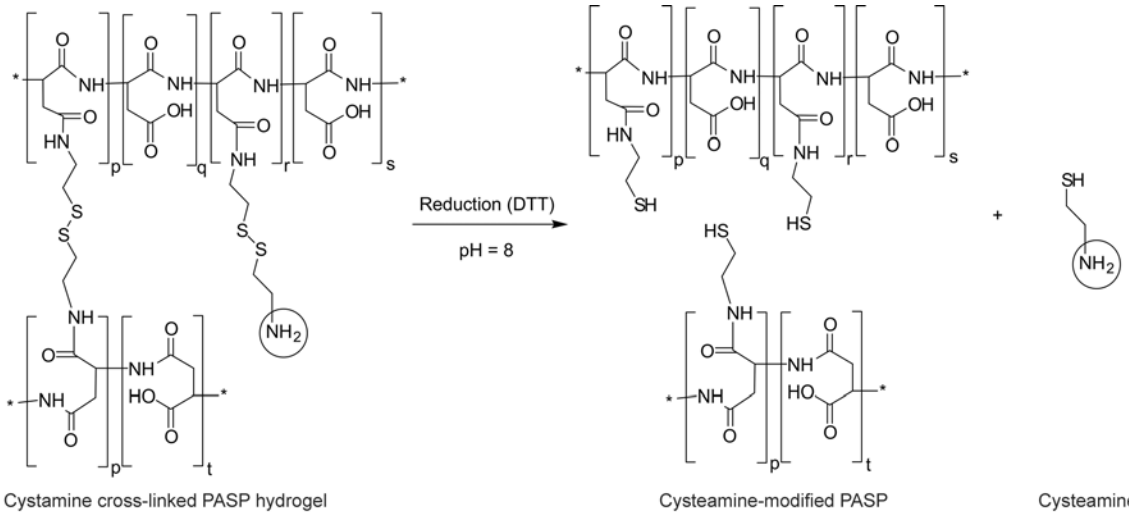

Figure 4. Reduction of cystamine cross-linked poly(aspartic acid) (PASP) gels to cysteamine-modified PASP and cysteamine

removal of cystamine by washing with 0.1 M HCl. For the reference measurements, the PSI-CYS gels were hydrolysed to disulphide cross-linked PASP (PASP-CYS) gels. A given amount ($m \cong 0.1$ g) of PASP-CYS gel was placed into a dialysis tube (cut-off molecular weight was 12 kDa) filled with 10 ml of a buffer solution (pH = 8) containing 10 mM DTT to reduce the disulphide bonds inside the hydrogel (Figure 4). Solutions of the reduced polymer and cysteamine were dialysed against water. The cysteamine concentration in the outer solution was determined with TNBS in the presence of sodium bromate ($c = 10^{-4}$ M). Calibration was done using cysteamine in aqueous buffer solution over the concentration range of $1.0 \cdot 10^{-5}$ to $8.0 \cdot 10^{-5}$ M ($c_{TNBS} = 7.3 \cdot 10^{-4}$ M, $\lambda = 420$ nm, $\varepsilon = 11\,727$ $M^{-1} \cdot cm^{-1}$, $r^2 = 0.9998$).

The stability of TNBS was determined in DMSO. Chemically cross-linked poly(vinyl alcohol) (PVA) gels were synthesized as it follows. 3.0 g of PVA solution (12 wt%) was diluted with 1.7 g of deionised water. Subsequently, 150 mg of 1 M GDA as a cross-linker and 100 µL of 20% HCl as a catalyst were added to the solution of PVA under continuous stirring at 25°C. The pre-cursor solution was transferred into Eppendorf tubes and kept there for 24 h. Unreacted cross-linker molecules were removed from the PVA gels by careful washing with de-ionized water. Lastly, the PVA hydrogels were immersed in DMSO, and the solvent was changed several times to produce PVA gels swollen in DMSO. A sample of PVA gel ($m \cong 0.1$ g) was immersed in TNBS (300 µL, 5 mM in DMSO) and incubated for 3 days. The gel was washed with DMSO (3·500 µL) to extract TNBS. The collected solution of TNBS was diluted with DMSO to 5000 µL. 50 µL DAB (8.80 wt% in DMSO) was added to 2000 µL of the diluted solution of TNBS. The absorbance spectrum of the solution was measured after 30 min against DMSO containing DAB at the same concentration as in the analyte.

3. Results and discussion

3.1. Determination of degree of chemical cross-linking in water

The unreacted DAB molecules were extracted from the PSI-DAB gel and reacted with TNBS at pH = 9.3. Figure 5a shows the absorption spectrum of the solution after 30 min (sample D in Table 1). The characteristic peak at 420 nm could not be detected. Thus, the concentration of cross-linker molecules is below the detection limit of the method ($1.2 \cdot 10^{-5}$ M) which means that less than 0.1% of the DAB molecules remain unreacted after the cross-linking process independently of the cross-linking ratio. Thus, each cross-linker molecule is attached to the polymer chain through at least one of its functional groups, in agreement with previously reported results [14].

After the immersion of the PASP-DAB gel into TNBS, the solution became yellow within 3 hours. A broad peak could be identified at 357 nm in the absorbance spectrum of the solution (Figure 5b). Because the supernatant must not contain amine groups, we can assume that the yellow compound is the hydrolysed by-product of TNBS, picric acid. The side reaction might have a larger reaction rate

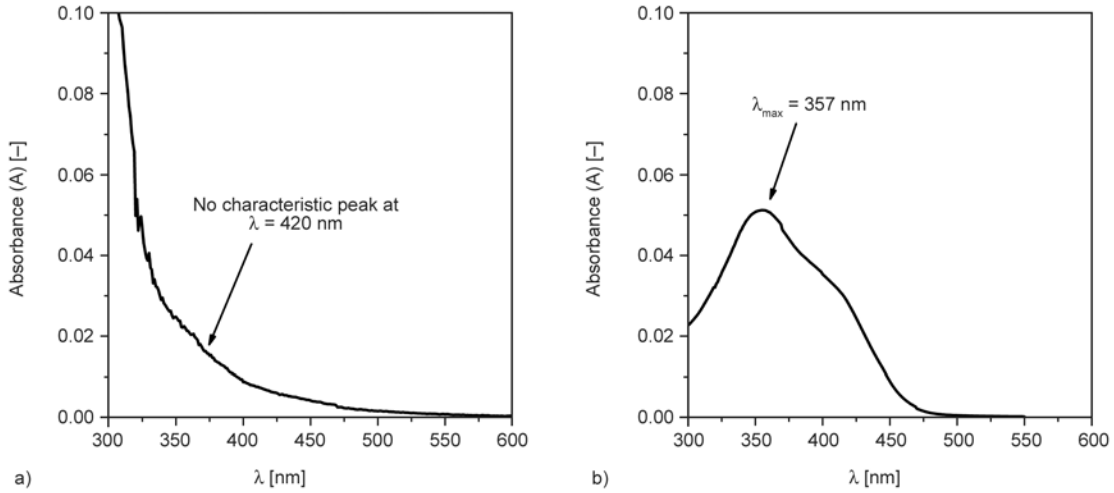

Figure 5. a) Absorption spectrum of the extracted swelling solution of PASP-DAB gel after the addition of TNBS in excess in aqueous buffer (pH = 9.3); b) absorption spectrum of the supernatant of PASP-DAB gels after 3 h incubation with TNBS in aqueous solution (pH = 9.3)

in the presence of the PASP gel, as indicated by the absence of a yellow product in the blank solution after the same reaction time. The dissimilar reaction rate of hydrolysis of TNBS can be explained by the difference in ionic strengths, i.e., PASP polyelectrolyte gels carry mobile counter-ions, which have a poorly defined effect on reaction kinetics. As a consequence, the number of pendant amines cannot be determined in aqueous solution and the reaction medium must be replaced to exclude side-reactions.

3.2. Reaction mechanism in DMSO

TNBS reacts with amine groups in DMSO as well, but several other factors must be considered. Contrary to the protic character of water, DMSO is a polar aprotic solvent. TNBS is a strong acid and exists in its dissociated form in alkaline aqueous solutions. Its dissociation is hindered in DMSO. Thus, TNBS remains protonated before the reaction with amine groups, which affects the mechanism of adduct formation. The stability of the Meisenheimer complex might also be different in DMSO [30]. We carried out a model reaction between TNBS and 1,4-diaminobutane in d_6-DMSO to propose the possible reaction mechanism. We confine our discussion to two cases that are relevant to the present analysis: first, a large excess of TNBS was maintained, and second, a large excess of DAB was maintained (the molar ratios of TNBS to DAB were 3 and 1/3, respectively). ^{1}H NMR spectra were recorded after 8 hours of reaction time. A detailed analysis of the reaction mechanism lies beyond the scope of the present study, and only the main conclusions are drawn here. The results of a detailed NMR analysis are to be published in another paper.

In all probability, sulphonic acid and primary amine groups form a salt in the dipolar solvent in a large excess of TNBS (Figure 6, I), followed by the nucleophilic addition of the primary amine group onto TNBS (Figure 6, II). The primary amine groups in the analyte can act as a base catalyst in the elimination of sulphonic acid groups (Figure 6, III). Accordingly, the conversion of TNBS to its amine-substituted derivative requires an excess of primary amine groups. Lastly, nucleophilic attack at the unsubstituted ring positions of TNBS may also occur in the large excess of primary amine groups (Figure 6, IV) [20, 30].

In a large excess of TNBS, the peak of the unreacted reagent appears at 8.8 ppm (H-a nuclei) in Figure 7. A relatively small peak at 8.9 ppm indicates the presence of the aniline derivative (Figure 6, III, H-b nuclei), assuming that a reaction time of 8 hours is sufficient for the total conversion of the Meisenheimer adduct (Figure 6, II) to the corresponding aniline (Figure 6, III). The broad peak at 7.6 ppm can be assigned to the salt of TNBS and DAB (Figure 6, I). The assumption is supported by the intensity integrals (I) of the peaks: I(H-c):I(H-d):I(H-e) = 3:2:2. The integrals indicate that both amine groups of DAB are protonated as shown in Figure 6.

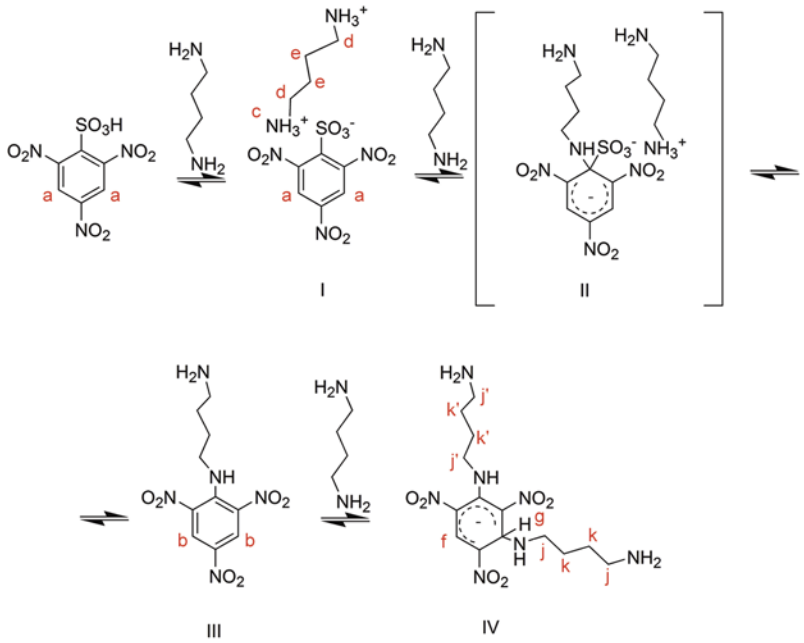

Figure 6. Proposed mechanism of the reaction between TNBS and 1,4-diaminobutane (DAB) in DMSO

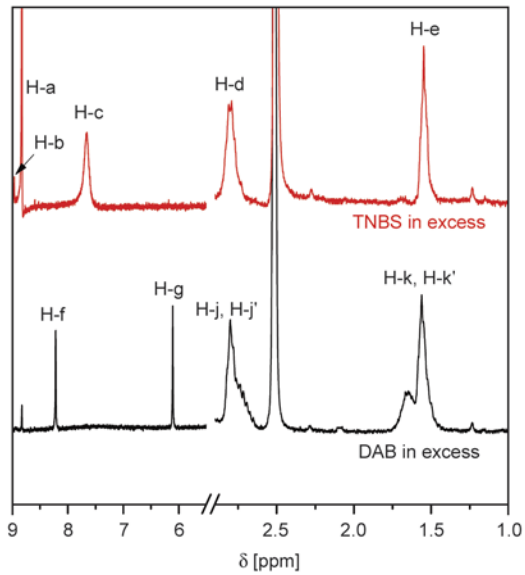

Figure 7. [1]H NMR spectra of the reaction product of TNBS and 1,4-diaminobutane in DMSO

In a large excess of DAB, the NMR spectrum is essentially different. The peak of TNBS (H-a) was reduced, indicating that only a small amount of the reagent remained in the mixture. The peak of ammonium group (H-c) disappeared; thus, we can assume that the equilibrium shifted towards the nucleophilic substitution of sulphonic acid groups and the formation of the aniline derivative. However, the peak of the H-b nucleus was not observed, whereas new peaks appeared at 8.1 and 6.0 ppm, indicating the formation of a new reaction product. The strong decrease in the chemical shift suggests the presence of an electron-rich chemical environment. The nucleophilic addition of primary amine groups to the unsubstituted ring positions resulted in the formation of a σ-complex (Figure 6, IV), which fits the chemical shifts (8.1 and 6.0 ppm) in the NMR spectrum [20]. The presence of this σ-complex is confirmed by the 1:1 intensity integrals of H-f and H-g nuclei.

The results prove that different species were present simultaneously in the reaction mixture. However, a reliable analysis requires a large excess of one of the reagents to shift the equilibrium to a well-defined product. Consequently, the molar ratio of TNBS to DAB was kept above 5 during the analysis of unreacted DAB to yield only the product I (Figure 6). Similarly, DAB was used in a 4-fold excess to TNBS during the quantitative determination of unreacted TNBS to yield only product IV (Figure 6).

3.3. Determination of degree of chemical cross-linking of PSI-DAB gels in DMSO

At first, unreacted cross-linker molecules were extracted from the PSI-DAB gel by washing with DMSO and the DAB molecules in the washing solution were reacted with TNBS. Similarly to the results obtained in aqueous medium, a characteristic peak ($\lambda = 437$ nm) was not obtained in the absorption spectrum of the solution (Figure 8a), indicating that less than 0.1% of the cross-linker molecules remain unreacted after the cross-linking process, independently of the cross-linking ratio.

Secondly, the PSI-DAB gel was immersed in the solution of TNBS. The supernatant remained colourless indicating that the formation of picric acid was excluded in DMSO. Unreacted TNBS was extracted from the gel by washing with DMSO, and its concentration was determined from the absorbance

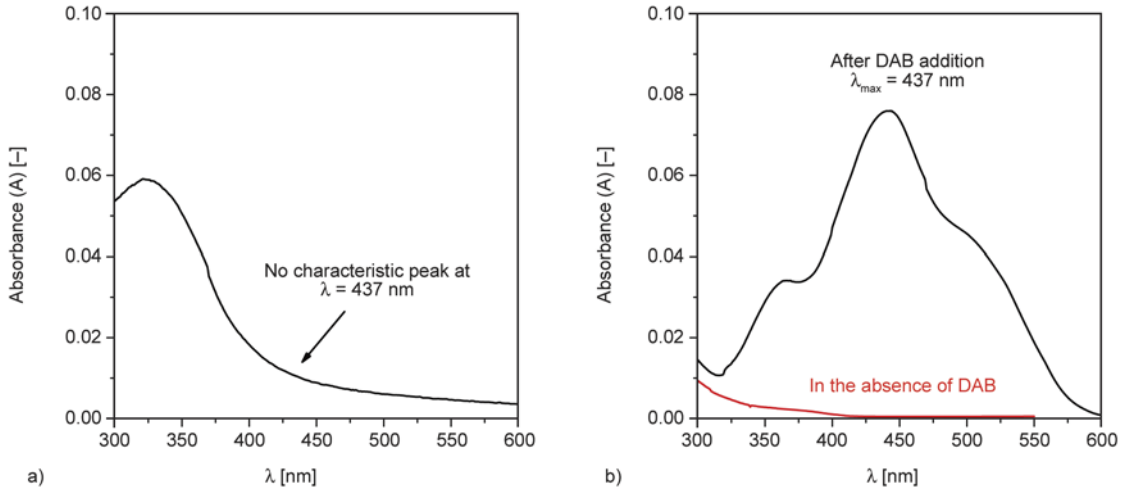

Figure 8. a) Absorption spectrum of the extracted washing solution of PSI-DAB gel after the addition of TNBS in DMSO; b) absorption spectrum of TNBS extracted from the gels in DMSO with and without DAB

spectrum after the addition of DAB (Figure 8b). The reaction time was varied between 1 to 5 days, but it did not affect the measured amount of unreacted TNBS; thus, a reaction time of 1 day was applied in further experiments. The conversion rate of diamine molecules to cross-linking points was smaller than 100% in each case (Figure 9a). Consequently, the degree of chemical cross-linking was smaller than its theoretical maximum value calculated from the total conversion of cross-linker molecules (Figure 9b). The difference between the degree of chemical cross-linking and its theoretical maximum is rather small, but we observed a clear tendency between the conversion rate and the cross-linking ratio (Figure 9a). A larger cross-linking ratio results in a larger conversion rate, which contradicts the original expectation. However, the observed correlation can be explained by the development of a network structure during the cross-linking process. The amine groups of the cross-linker molecules and succinimide repeating units exhibit high reactivity; thus, a slightly cross-linked structure with pendant amine groups must form during the first stage of the cross-linking process. The presence of chemical cross-linking points reduces the segmental mobility of the polymer, which hinders the further formation of amide linkages; therefore, the structure formed in the initial stage of the process essentially affects any further reaction. In the case of a large cross-linking ratio, the polymer chains are densely cross-linked, which has a dual effect. First, the degree of swelling is significantly smaller than that of a less densely cross-linked gel (see the degree of swelling values in DMSO in Table 1) because of the elastic effect of net points, and the increased polymer concentration inside the forming gel accelerates the reaction. Second, the densely cross-linked structure orients the pendant amine groups for amide formation with the succinimide groups of adjacent polymer chains. Amide formation is supported by favourable distance of polymer chains and the orientation effect might be further strengthened by hydrogen bonds between nearby pendant amine groups. Further effects must be also important in this case *e.g.,* electrostatic interactions in the polyelectrolyte network. All of these effects are less significant in a loosely cross-linked network, resulting in a lower conversion rate of cross-linker molecules. Nevertheless, the conversion rate was remarkably high (>70%), and the degree of chemical cross-linking was also relatively high over the investigated range.

3.4. Stability and accuracy

TNBS was incubated in PVA gels for 3 days in the absence of free amines and approximately 99.9% of the feed amount of the reagent was recovered after careful washing of the gel. Therefore, the reagent is chemically stable in DMSO, and long-term measurements can be carried out without the formation of interfering by-products.

The accuracy of the TNBS assay was verified on PASP-CYS gels by quantifying of cysteamine after cleavage of disulphide linkages inside the gels. The presence of thiol groups during the analysis interferes with the reaction of TNBS and free amines, thus sodium bromate was used to oxidize excess

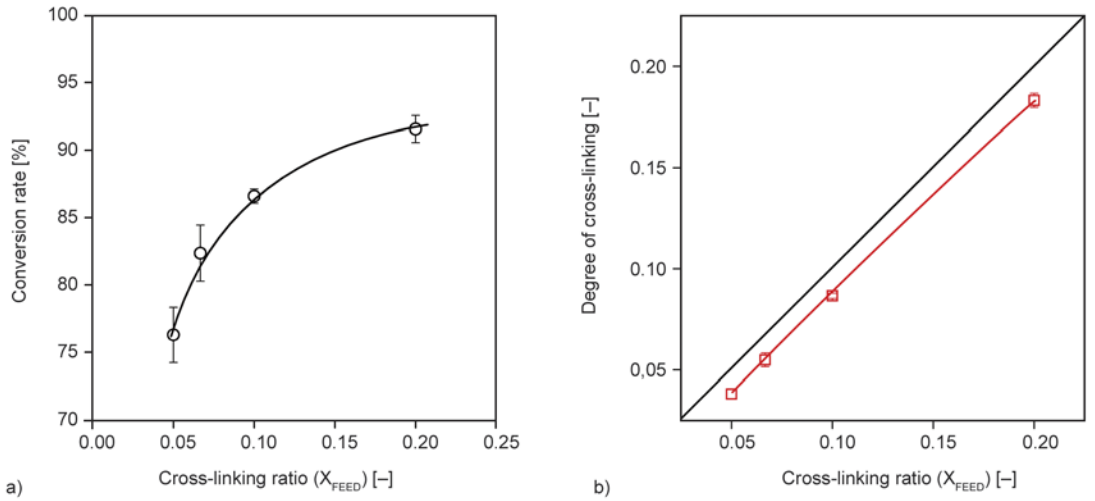

Figure 9. a) Conversion rate of diamine molecules to cross-linking points as a function of cross-linking ratio (X_{FEED}); b) Correlation between the degree of chemical cross-linking and the cross-linking ratio. The diagonal line represents 100% conversion. The curves on both diagrams are used to guide the eye.

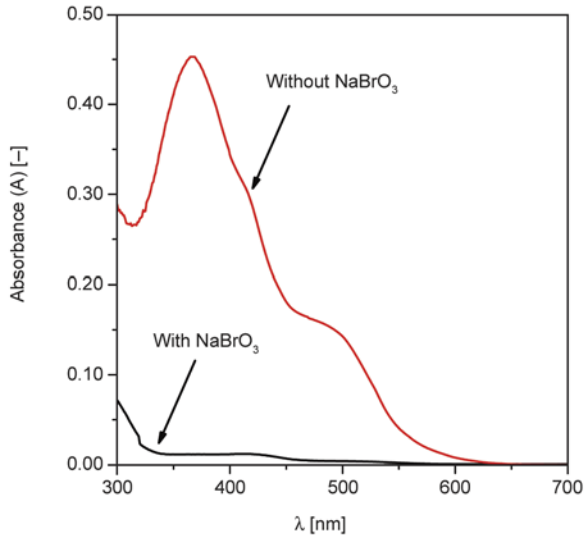

Figure 10. Absorption spectrum of TNBS in the presence of dithiothreitol (DTT) with and without the addition of sodium bromate ($NaBrO_3$) as oxidizing agent

DTT after dialysis (Figure 10). The number of pendant amine groups in the PSI-CYS gel was also determined in DMSO with the developed TNBS assay. Results show that 8.0±1.4% of cystamine do not form chemical cross-links, whereas the reduction-based method yielded a value of 11.3±1.8%. According to an F-test, reproducibilities of the two methods are equal at a significance level of 95%, and a paired t-test proved that the numbers of pendant amine groups obtained by the two methods are the same at a significance level of 95%. Consequently, the method developed for the quantitative determination of pendant amine groups in DMSO exhibits satisfactory accuracy for chemically cross-linked aspartic acid-based polymer gels.

4. Conclusions

A novel method using 2,4,6-trinitrobenzensulphonic acid (TNBS) was developed to determine the degree of chemical cross-linking in aspartic acid-based polymer gels. The conventional TNBS method is reliable for the quantitative determination of small molecular amines in alkaline aqueous medium because the hydrolysis of the reagent does not interfere with the analysis if the reaction time is short. However, analysis of polymer networks bearing pendant amine groups is difficult in aqueous medium because of the formation of picric acid in a considerable amount. The TNBS assay was implemented in DMSO, and the reaction products were examined by ^{1}H NMR. The formation of picric acid was excluded, and the degree of chemical cross-linking of polysuccinimide gels was determined. Less than 0.1% of the cross-linker molecules remained unreacted because of the high reactivity of diamine molecules and the repeating units of the polymer. The conversion rate of diamine molecules to chemical cross-linking points was high but strongly depended on the feed composition of the gels. The stability of the reagent and accuracy of the developed method are satisfactory; thus, the method can be used to determine the degree of chemical cross-linking of PSI gels. Furthermore, this method can be extended to analyse other DMSO-swollen polymer gels bearing pendant amine groups.

5. Acknowledgements

This research was supported by the OTKA Foundation (PD76401) and by the New Széchenyi Development Plan (TÁMOP-4.2.1/B-09/1/KMR-2010-0002). András Szilágyi thanks the János Bolyai Research Scholarship of Hungarian Academy of Sciences for its support. The authors would like to thank Viktor Csókai for his help in the evaluation of the NMR spectra.

References

[1] Tanaka Y., Gong J. P., Osada Y.: Novel hydrogels with excellent mechanical performance. Progress in Polymer Science, **30**, 1–9 (2005).
DOI: 10.1016/j.progpolymsci.2004.11.003

[2] Gyenes T., Torma V., Gyarmati B., Zrínyi M.: Synthesis and swelling properties of novel pH-sensitive poly (aspartic acid) gels. Acta Biomaterialia, **4**, 733–744 (2008).
DOI: 10.1016/j.actbio.2007.12.004

[3] Kopeček J.: Hydrogel biomaterials: A smart future? Biomaterials, **28**, 5185–5192 (2007).
DOI: 10.1016/j.biomaterials.2007.07.044

[4] Wang H., Shi Y., Wang L., Yang Z.: Recombinant proteins as cross-linkers for hydrogelations. Chemical Society Reviews, **42**, 891–901 (2013).
DOI: 10.1039/c2cs35358j

[5] Çaykara T., Akçakaya I.: Swelling behaviors of ionic poly(*N*,*N*-dimethylacrylamide-*co*-acrylamide) hydrogels in various media. Journal of Applied Polymer Science, **104**, 2140–2145 (2007).
DOI: 10.1002/app.24313

[6] Xu K., Tan Y., Chen Q., An H., Li W., Dong L., Wang P.: A novel multi-responsive polyampholyte composite hydrogel with excellent mechanical strength and rapid shrinking rate. Journal of Colloid and Interface Science, **345**, 360–368 (2010).
DOI: 10.1016/j.jcis.2010.01.058

[7] Kersey F. R., Loveless D. M., Craig S. L.: A hybrid polymer gel with controlled rates of cross-link rupture and self-repair. Journal of the Royal Society Interface, **4**, 373–380 (2007). DOI: 10.1098/rsif.2006.0187
[8] De S. K., Aluru N. R., Johnson B., Crone W. C., Beebe D. J., Moore J.: Equilibrium swelling and kinetics of pH-responsive hydrogels: Models, experiments, and simulations. Journal of Microelectromechanical Systems, **11**, 544–555 (2002). DOI: 10.1109/jmems.2002.803281
[9] Flory P. J.: Principles of polymer chemistry. Cornell University Press, Ithaka (1953).
[10] Wagermaier W., Kratz K., Heuchel M., Lendlein A.: Characterization methods for shape-memory polymers. Advances in Polymer Science, **226**, 97–145 (2010). DOI: 10.1007/12_2009_25
[11] Treloar L. R. G.: The physics of rubber elasticity. Oxford University Press, Oxford (1958).
[12] Mark J. E., Erman B.: Rubberlike elasticity. Cambridge University Press, Cambridge (2007).
[13] Yang J., Wang F., Tan T.: Degradation behavior of hydrogel based on crosslinked poly(aspartic acid). Journal of Applied Polymer Science, **117**, 178–185 (2010). DOI: 10.1002/app.31943
[14] Torma V., Gyenes T., Szakács Z., Zrínyi M.: A novel potentiometric method for the determination of real crosslinking ratio of poly(aspartic acid) gels. Acta Biomaterialia, **6**, 1186–1190 (2010). DOI: 10.1016/j.actbio.2009.08.045
[15] Kiranas E. R., Tzouwara Karayanni S. M., Karayannis M. I.: The reaction of glutamic acid and trinitrobenzenesulfonic acid–kinetic study and analytical application. Talanta, **44**, 1113–1121 (1997). DOI: 10.1016/s0039-9140(96)02205-9
[16] Cayot P., Tainturier G.: The quantification of protein amino groups by the trinitrobenzenesulfonic acid method: A reexamination. Analytical Biochemistry, **249**, 184–200 (1997). DOI: 10.1006/abio.1997.2161
[17] Brown H. H.: A study of 2,4,6-trinitrobenzenesulfonic acid for automated amino acid chromatography. Clinical Chemistry, **14**, 967–978 (1968).
[18] Snyder S. L., Sobocisnki P. Z.: An improved 2,4,6-trinitrobenzenesulfonic acid method for the determination of amines. Analytical Biochemistry, **64**, 284–288 (1975). DOI: 10.1016/0003-2697(75)90431-5
[19] Grotzky A., Manaka Y., Fornera S., Willeke M., Walde P.: Quantification of α-polylysine: A comparison of four UV/Vis spectrophotometric methods. Analytical Methods, **2**, 1448–1455 (2010). DOI: 10.1039/c0ay00116c
[20] Crampton M. R.: The stabilities of Meisenheimer complexes. Part 15. The interactions of 2,4,6-trinitrobenzenesulphonate ions with sodium sulphite and with sodium hydroxide in water. Journal of the Chemical Society, Perkin Transactions 2, **1978**, 343–346 (1978). DOI: 10.1039/p29780000343
[21] Ives D. J. G., Moseley P. G. N.: Picric acid in aqueous solution. Journal of the Chemical Society B: Physical Organic, 757–761 (1966). DOI: 10.1039/J29660000757
[22] Means G. E., Congdon W. I., Bender M. L.: Reactions of 2,4,6-trinitrobenzenesulfonate ion with amines and hydroxide ion. Biochemistry, **11**, 3564–3571 (1972). DOI: 10.1021/bi00769a011
[23] Brannon-Peppas L., Peppas N. A.: Equilibrium swelling behavior of dilute ionic hydrogels in electrolytic solutions. Journal of Controlled Release, **16**, 319–329 (1991). DOI: 10.1016/0168-3659(91)90009-3
[24] Kirchmajer D. M., Watson C. A., Ranson M., in het Panhuis M.: Gelapin, a degradable genipin cross-linked gelatin hydrogel. RSC Advances, **3**, 1073–1081 (2013). DOI: 10.1039/c2ra22859a
[25] Bubnis W. A., Ofner III C. M.: The determination of ε-amino groups in soluble and poorly soluble proteinaceous materials by a spectrophotometrie method using trinitrobenzenesulfonic acid. Analytical Biochemistry, **207**, 129–133 (1992). DOI: 10.1016/0003-2697(92)90513-7
[26] Ofner III C. M., Bubnis W. A.: Chemical and swelling evaluations of amino group crosslinking in gelatin and modified gelatin matrices. Pharmaceutical Research, **13**, 1821–1827 (1996). DOI: 10.1023/A:1016029023910
[27] Kuijpers A. J., Engbers G. H. M., Feijen J., De Smedt S. C., Meyvis T. K. L., Demeester J., Krijgsveld J., Zaat S. A. J., Dankert J.: Characterization of the network structure of carbodiimide cross-linked gelatin gels. Macromolecules, **32**, 3325–3333 (1999). DOI: 10.1021/ma981929v
[28] Vichasilp C., Nakagawa K., Sookwong P., Higuchi O., Kimura F., Miyazawa T.: A novel gelatin crosslinking method retards release of mulberry 1-deoxynojirimycin providing a prolonged hypoglycaemic effect. Food Chemistry, **134**, 1823–1830 (2012). DOI: 10.1016/j.foodchem.2012.03.086
[29] Gyarmati B., Vajna B., Némethy Á., László K., Szilágyi A.: Redox- and pH-responsive cysteamine-modified poly(aspartic acid) showing a reversible sol–gel transition. Macromolecular Bioscience, **13**, 633–640 (2013). DOI: 10.1002/mabi.201200420
[30] Crampton M. R., Routledge P. J.: The stabilities of Meisenheimer complexes. Part 34. Kinetic studies of σ-adduct formation and nucleophilic substitution in the reactions of 2,4,6-trinitrophenetole with aliphatic amines in dimethyl sulphoxide. Journal of the Chemical Society, Perkin Transactions 2, **1984**, 573–581 (1984). DOI: 10.1039/p29840000573